MINISTRY OF EDUCATION
AND TRAINING

VIETNAM ACADEMY
OF SCIENCE AND TECHNOLOGY

GRADUATE UNIVERSITY SCIENCE AND TECHNOLOGY

Nguyen Thi Bich Ngoc

THE ROLE OF MAGNETIC FIELDS IN STAR FORMATION

DISSERTATION ON SCIENCES OF MATTER

Major: Atomic and Nuclear Physics
Code: 9 44 01 06

Hanoi - 2026

Chapter 1

Introduction

To start this thesis, I will introduce the essential scientific background in this Chapter. Section 1 will present an overview of the star formation. Magnetic fields play an important role in star formation across various spatial scales. In addition, although dust only constitutes about 1% of the ISM, it plays a fundamental role in various physicochemical processes. Therefore, I will present the magnetic fields in star formation in Section 2. Since dust polarization is widely used to infer magnetic fields, an understanding of dust physics, particularly the grain alignment paradigm, is necessary to ensure reliable interpretations. We cannot reliably trace magnetic fields with dust polarization if dust alignment is not correctly understood. Dust physics is presented in Section 3. In Section 4, I will present the current open questions and the motivation for this Ph.D. work.

1.1. Introduction to Star Formation

1.1.1. Interstellar Medium

Star formation begins when gas in the interstellar medium (ISM) of galaxies starts to gather and condense. As gravity pulls the diffuse gas together, its density gradually increases. Under suitable conditions, this process gives rise to molecular clouds, dense cores, and eventually to the formation of stars and planets. The ISM is a scientific laboratory that helps us understand the material from which stars form. ISM is a non-homogeneous, dynamic, and evolving medium containing multiple phases with different temperature and density conditions. The interstellar gas is primarily H and He, and an addition of a small amount of heavy elements results from stars and stellar explosions. The most occupied volume of the ISM is the warm and hot components, which have high temperatures and low densities. However, these components contribute very little to the total mass of the ISM. The cold ISM, i.e., neutral and molecular gas, is the one that contributes the most to the total mass of the ISM. McKee & Ostriker [1] proposed a theory of the ISM in which they divided the ISM into different phases, mainly regulated by the feedback from supernova explosions. The ISM is dynamic, and the matter can change phases, e.g., ionizing and cooling. The different phases of the ISM were reviewed as follows [2]:

- **Hot ionized medium (HIM) or coronal gas**: It consists of gas that is shock-heated by blast waves from supernova explosions. It has high temperatures $T > 10^{5.5}$ K, low number density $\sim 0.004\,\mathrm{cm}^{-3}$.

- **H II gas**: Its hydrogen has been photoionized by UV photons from nearby stars, referred to as H II region or diffuse H II. $T \sim 10^4$ K, $n_{\mathrm{H}} \sim 0.3 - 10^4\,\mathrm{cm}^{-3}$.

- **Warm Ionized Medium (WIM)**: It consists of a hot plasma embedded mostly in the

HIM and heated by the Lyman continuum radiation coming from nearby hot young stars.

- **Warm Neutral Medium (WNM)**: Its gas has a low ionization fraction, and 60% of it is in the form of neutral atomic hydrogen with a temperature of about 5000 K and a density lower than 1 cm^{-3}

- **Cold Neutral Medium (CNM)**: It consists of colder atomic gas (< 100 K), ~1% of the volume of the local ISM, mainly associated with molecular gas and is highly filamentary (e.g., [3]).

- **Diffuse** H_2: Known to be extended in the CNM region and dense enough to prevent the photo-dissociation of H_2 molecules by the thermal radiation from nearby stars.

- **Dense** H_2: Temperature varies between 10 K – 50 K, and the density ranges between 10^3 – $10^6 cm^{-3}$ which is high enough to form clumps and cores that can be observed using CO line or dust continuum observations.

1.1.2. Molecular Clouds

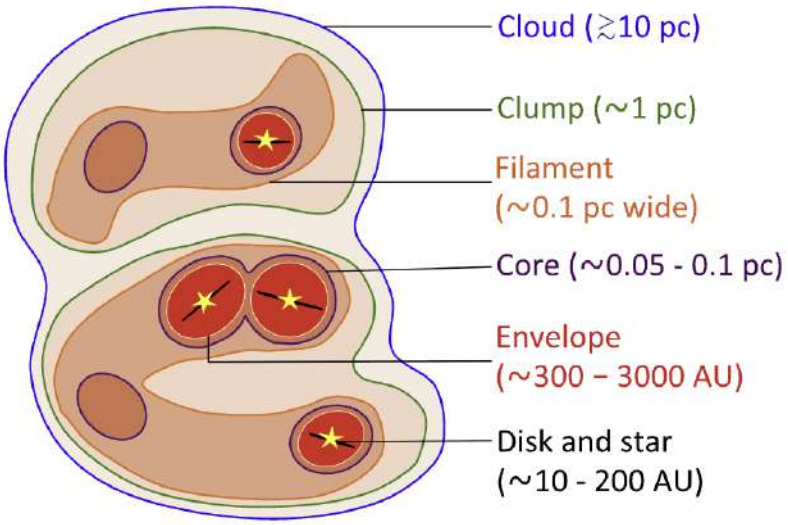

Figure 1.1: Cartoon of a molecular cloud with the information about their gas density, masses, sizes, and main tracers used for observations. The structures are not drawn to scale. Figure adopted from [4].

The coldest and densest regions of ISM, where the temperature is about 10 – 25 K, and the density is larger than 10^2 cm^{-3}, are known as molecular clouds [5]. Molecular cloud sizes vary from 1 – 100 pc [6]. The largest clouds are called Giant Molecular Clouds, whose masses can be from 10^5 to $10^7 M_\odot$. Molecular clouds exhibit various shapes, such as spherical, elongated, or filamentary structures, and they serve as the primary sites for stellar birth, initiating the process of star formation. Molecular clouds are composed mainly of molecular H_2, He, and the CO molecule. About 1% of molecular cloud mass is attributed to dust grains. Distributed throughout the Milky Way, molecular clouds offer an opportunity to study star formation under various conditions, such as low- and high-mass regions, as well as isolated and cluster environments.

Infrared dark clouds (IRDCs) are dense and cold regions of molecular clouds. IRDCs are quiescent, containing many compact cores and clumps, which are believed to be the cradles of massive stars and star clusters (e.g., [7]). Extinction results from the absorption and scattering of light on cold dust grains. They can be observed as regions of strong emission in near- and mid-infrared because the dust grains re-emit the absorbed energy at longer wavelengths.

These are cold, dense, and relatively inactive molecular clouds in their early stages. Over time, IRDCs undergo fragmentation, leading to the formation of dense cores and clumps. As massive stars begin to form, their feedback generates H II regions or expanding bubbles. Eventually, these structures evolve to resemble the bright, filamentary molecular clouds commonly found in regions of high-mass star formation.

Molecular clouds can gravitationally collapse to form cores and stars. Cores are the smallest, densest regions within a molecular cloud, which have sizes around 0.03 to 0.2 pc. Individual stars are formed from cores. *Herschel* space telescope [8] revealed hierarchical sub-structures within molecular clouds: clumps and dense cores. Clumps are dense (n $\sim 10^3 - 10^4\,\mathrm{cm}^{-3}$) with typical sizes of $0.1 - 3\,\mathrm{pc}$ and masses of $50 - 500 M_\odot$. Dense cores have densities of $\sim 10^5 - 10^6\,\mathrm{cm}^{-3}$ and sizes of $0.01 - 0.1\,\mathrm{pc}$. The dense cores are the sites of forming single or multiple stars [9]. Cores without evidence of star formation are referred to as starless cores. Cores that already possess the embedded young stellar objects (YSOs) are called protostellar cores. Figure 1.1 illustrates a cartoon of a molecular cloud and its sub-structures.

1.1.3. Filaments

Filaments are ubiquitous in the ISM. It is well-recognized that molecular clouds contain filamentary structures (e.g., [10]). High-resolution observations made by *Herschel* suggested that most molecular clouds show filamentary structures [11]. Moreover, most protostars and prestellar cores are formed along filaments [12]. It suggests that filaments can be an important step in the star formation process. Figure 1.2 shows the column density map of Aquila observed in *Herschel* overlaid with filament networks (left) and prestellar and protostar cores (right) [13]. The spatial distribution of filaments varies from one cloud to another, and some contain very complex filamentary networks with low-density sub-filaments.

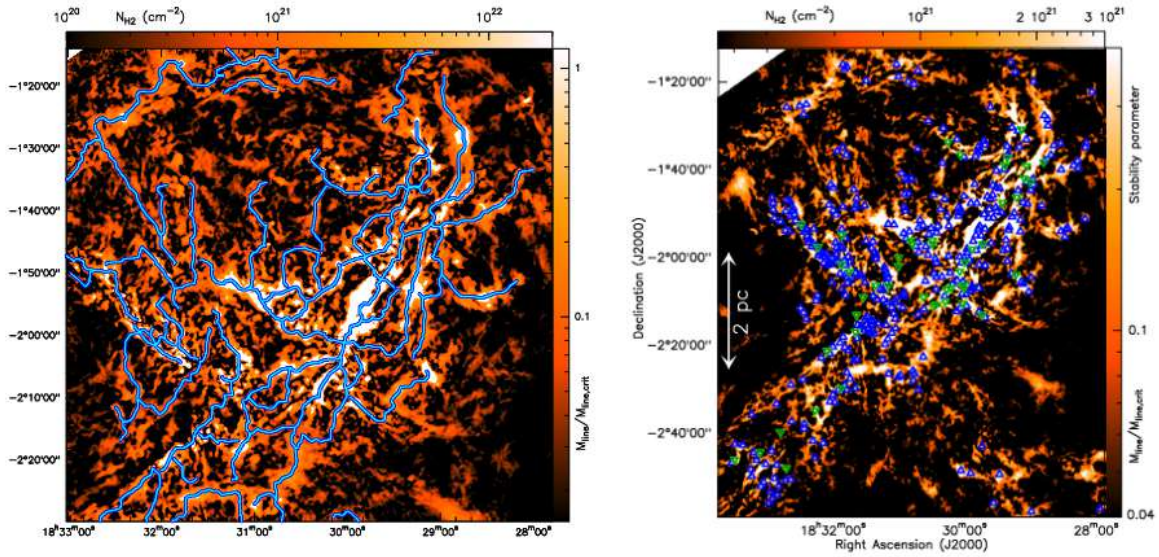

Figure 1.2: Aquila molecular cloud. Left: Column density map derived from *Herschel* data and filament network (blue lines) identified with the DisPerSE algorithm [14]. Right: Candidates for prestellar (blue) and protostellar (green) cores overlaid on the density map. The Figure is adapted from [13]

A filament becomes gravitationally unstable when its line mass exceeds a critical threshold [15]: $M_{\mathrm{line,crit}} = 2c_s^2/G$, where $c_s = \sqrt{k_\mathrm{B}T/m}$ is the isothermal sound speed and G is the

gravitational constant. For a typical temperature of $\sim$ 10 K, this critical line mass corresponds to about 15 $M_\odot$/pc [12].

The filament's radial profile is described by a Plummer-like function (e.g., [11, 16]) of the form:

$$N_p(r) = N^0_{H_2} / [1 + (r/R_{\rm flat})^2)]^{\frac{p-1}{2}} \tag{1.1}$$

where r is the radial distance, $R_{\rm flat}$ is the radius of the inner, flat region of the density profile, and p is the power-law density exponent at large radii. The model volume density profile is calculated as

$$\rho_p(r) = \rho_c / [1 + (r/R_{\rm flat})^2)]^{p/2} \tag{1.2}$$

The filament width can be calculated as $\sim 2R_{\rm flat}$. A width of the nearby filaments of $\sim$ 0.1 pc in several local molecular clouds was found [16]. Long filaments in our Galaxy having widths of 1–40 pc were found [17].

The typical width of 0.1 pc in nearby star-forming regions has prompted questions regarding the filament's origin and the physical significance of its characteristic width. One plausible explanation is that filaments may form at the intersection of two shock waves, observed in some regions (for example, OMC-1) due to the supersonic turbulence [18, 19]. Others claim that the filament width originates from magnetohydrodynamic turbulence (e.g., see [11]). Based on the *Herschel* observations, the "filament paradigm" for star formation represents two key steps in the star formation process (1) turbulence shifts up the gas, giving rise to a web-like structure in the ISM, and (2) gravity takes over and controls the further fragmentation of filaments into prestellar cores and eventually protostars [11, 20]. According to the filament paradigm, magnetic fields are proposed to play a role in driving the evolution of filaments and overseeing the star formation process (see more in Section 1.2).

1.1.4. Star Formation

1.1.4.1. Gravitational Collapse of Dense Cores

Stars form through the gravitational collapse of molecular clouds. When a cloud is massive enough, its self-gravity exceeds internal pressure support, the cloud collapses. The initial model of cloud collapse was introduced by [21]. This model assumes that molecular clouds are governed by self-gravity and the internal pressure due to their gravitational instability.

For a sphere cloud of perfect gas at temperature T, its internal kinetic energy is:

$$E_{\rm kin} = \frac{3}{2}\frac{M k_{\rm B} T}{\mu m_{\rm H}}, \tag{1.3}$$

where M is the internal mass of the system, $k_{\rm B}$ is the Boltzman constant, $m_{\rm H}$ the mass of a hydrogen atom, μ is the weight of hydrogen molecule.

The gravitational energy is:

$$E_{\rm grav} = -\frac{3}{5}\frac{GM^2}{R}, \tag{1.4}$$

where R is the radius of the cloud. The cloud mass $M = \rho\frac{4}{3}\pi R^3$ with ρ the cloud density.

When $E_{\rm grav} > E_{\rm kin}$, the core has to collapse. The minimum mass, known as the Jeans mass $M_{\rm Jeans}$, was first derived in [21] and is expressed as:

$$M_{\rm Jeans} = \frac{4\pi}{3}\frac{c_s^3}{\sqrt{G^3\rho}} \tag{1.5}$$

where c_s is the isothermal sound speed of the gas.

The Jeans length is the length at which gravity starts to dominate and the cloud is fragmenting. It is given by the following equation:

$$L_{\text{Jeans}} = \sqrt{\frac{\pi c_s^2}{G\rho}} \tag{1.6}$$

The Jeans mass typically underestimates the minimum mass needed for collapse when neglecting the impact of turbulence and magnetic fields. Magnetic fields provide magnetic pressure, and turbulence can inject nonthermal kinetic energy to destroy the overdense regions. Radiative and mechanical feedback from external sources can also influence gravitational collapse. Moreover, the star formation efficiencies are very low (about 1-4%) in nearby star-forming regions (e.g., [22]). This suggests that star formation is inefficient and must be slowed down by other forces. Therefore, the simplistic Jeans model does not reproduce the physics of cloud collapse, and it has to consider the other energy.

Considering that the core is in a state of virial equilibrium of the gravitational potential, internal kinetic, magnetic [23], and external pressure, P_{ext}, on the core [24] energies, for the same hypothetical homogeneous spherical core with a uniform magnetic field, B, the virial theorem is expressed as:

$$\frac{3Mk_{\text{B}}T}{\mu m_{\text{H}}} - 4\pi R^3 P_{\text{ext}} - \frac{1}{R}\left(\frac{3}{5}GM^2 - \frac{1}{3}R^4B^2\right) = 0. \tag{1.7}$$

1.1.4.2. Low-mass Star Formation

There are four stages of the evolution for low-mass ($< 8M_{\odot}$) protostars to the main sequence: Class 0, Class I, Class II, and Class III, from the least to the most evolved. Classes I to III were proposed by [26], and Class 0 was added later by [27]. [28] reported one more phase, flat spectral, which lies between Class I and II.

The classification of these stages is based on their spectral energy distribution (SED) features. The slope of the SED is defined as $\alpha_{IR} = \frac{dlog(\lambda F_\lambda)}{dlog\lambda}$, with F_λ is the flux at the wavelength λ [29]. Figure 1.3 and Table 1.1 summarize the main properties of these stages and their evolution as theoretical and observational properties.

In the collapse phase, the formation of a slowly rotating core is embedded in a molecular cloud clump. At Class 0, a protostar is already formed, although its envelope remains more massive than the protostar. The lifetime of the Class 0 objects is estimated to be about 10^4 years. At Class I, the protostar might be surrounded by an early protoplanetary disk with a massive envelope. Class II is surrounded by a protoplanetary disk, whereas Class III is surrounded by a debris disk.

1.1.4.3. High-mass Star Formation

Among the topics of star formation, the formation of massive stars is still much less understood than that of low-mass stars [30]. Although massive stars make up less than 1% of the stellar population, they are responsible for about 99% of the UV photons. Throughout their evolution, they have a major impact on the ISM. During the protostellar stage, accretion is accompanied by powerful outflows that inject large amounts of energy and momentum into the surrounding medium. Later, during their short lifetimes, strong stellar winds and intense UV radiation ionize the nearby ISM. At the end of their evolution, they explode as supernovae, returning chemically enriched material to the ISM. These feedback processes can interact

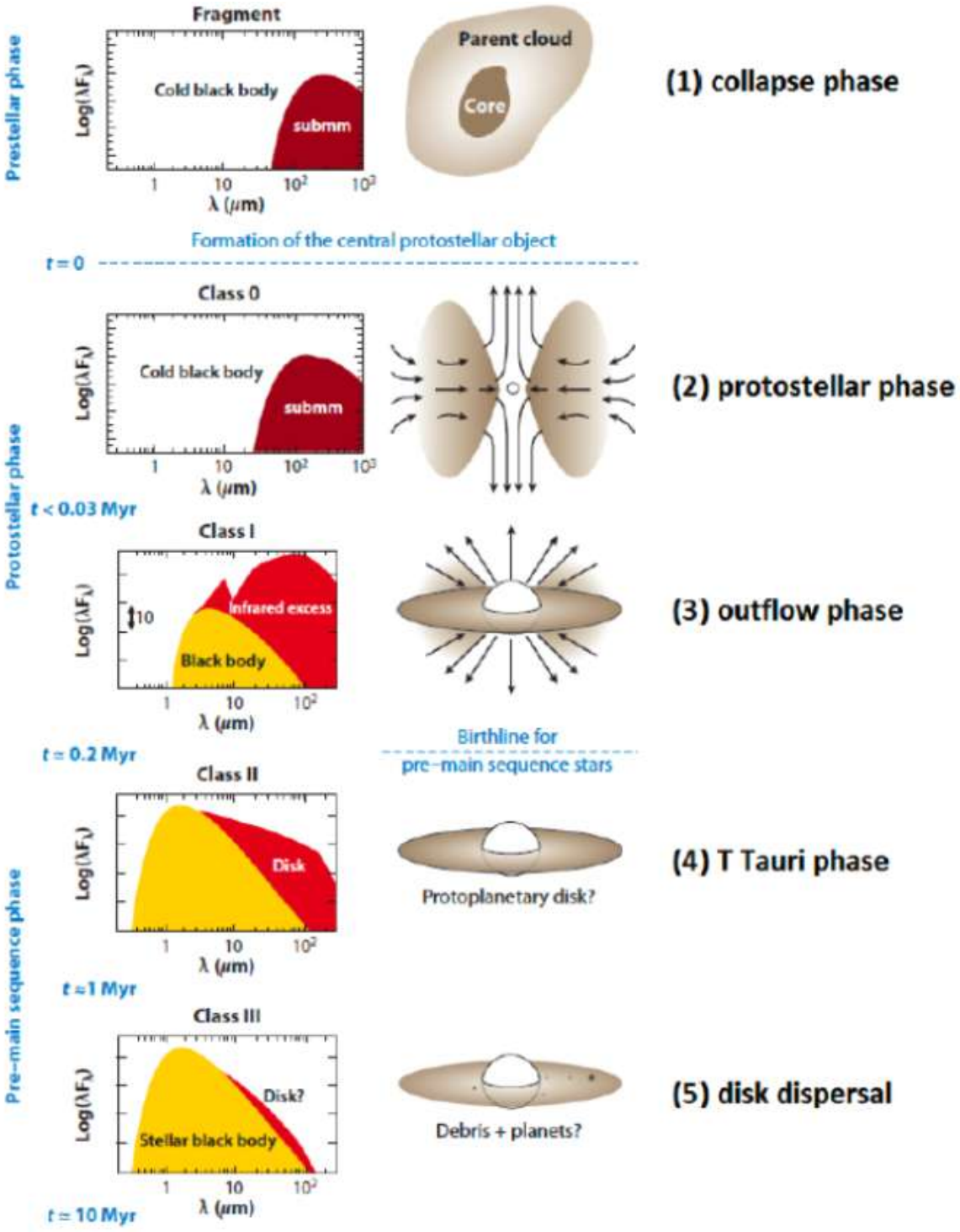

Figure 1.3: Evolutionary phases for low-mass star formation, from dark clouds to planetary systems. The classification is inferred based on SED features (Class 0, I, II, III). Source: [25].

with nearby molecular clouds and may trigger a new generation of star formation. In contrast to low-mass stars, massive stars are rare and evolve rapidly, with their whole formation and evolution occurring within only a few million years. Although high-mass stars are very important, the picture of massive star formation has not yet been established. Two leading theories of high-mass star formation include: (1) massive stars form as low-mass stars [31] and (2) competitive accretion, in which stars form in a cluster, acquiring mass through either

Table 1.1: Classification of young stellar objects

Class	SED slope	Timelife (Myr)	Physical properties	Observation characteristics
0	–	0.03-0.2	$M_{env} > M_{star} > M_{disk}$	No optical or near-IR emission
I	> 0.3	0.3-0.5	$M_{star} > M_{env} \sim M_{disk}$	Generally optically obscured
II	−1.6-0.3	∼2	$M_{disk}/M_{star} \sim 0.01$ $M_{env} \sim 0$	Accreting disks
III	<−1.6	∼10	$M_{disk}/M_{star} << 0.01$ $M_{env} \sim 0$	Passive disk; no or very weak accretion

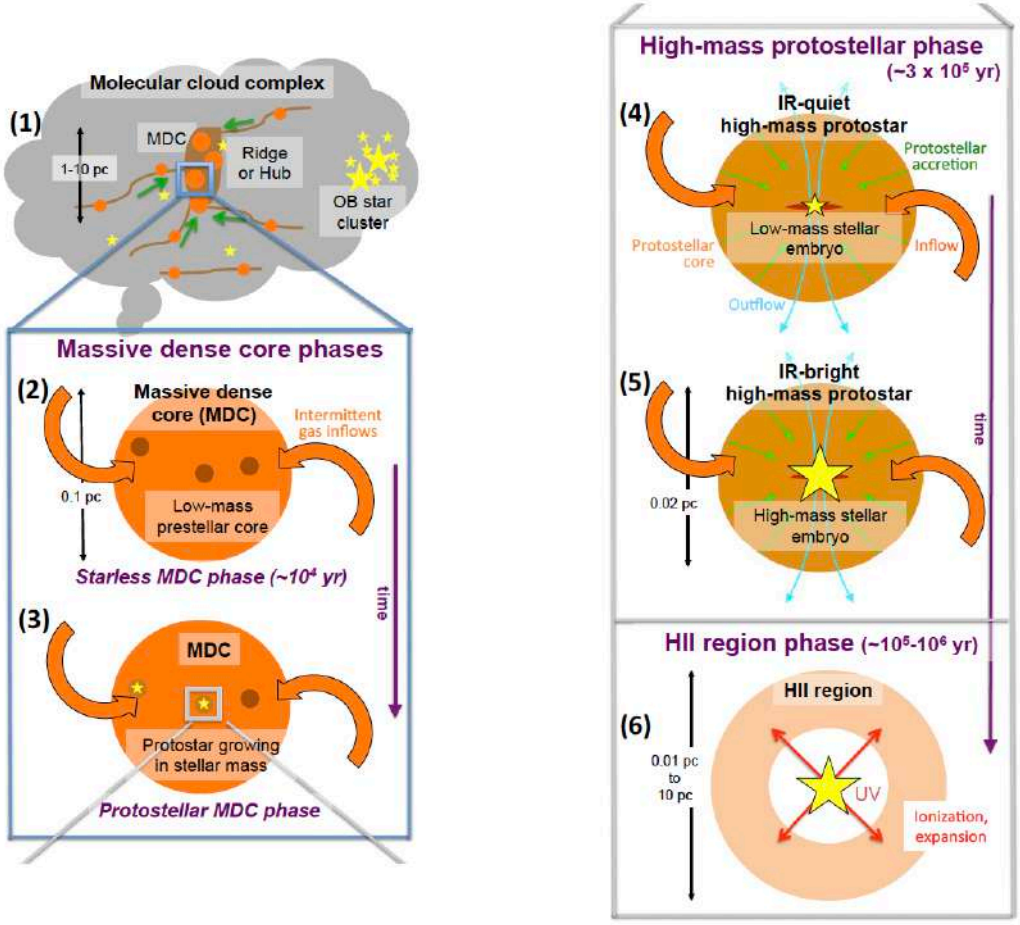

Figure 1.4: Evolutionary phases for high-mass star formation [30].

accretion of a common reservoir [32] or accretion streams from cloud collapse [33].

In the core accretion models, high-mass star formation is a scaled-up version of low-mass star formation. Massive stars form from large, turbulent, and magnetically supported prestellar cores that resist fragmentation. These cores, typically compact, ∼0.01 – 0.1 pc, dense, n_{H_2} $\sim 10^6$ cm^{-3}, and cold, ∼10 K, are strong candidates for high-mass star formation [12]. Com-

petitive accretion, on the other hand, posits that stars form in clusters, with more massive stars forming near the cluster center. Here, the gravitational potential of the cluster allows stars closer to the core to accrete more material, growing into massive stars. Observations of massive stars in star clusters support this model. Figure 1.4 shows the evolutionary diagram proposed for the formation of high-mass stars.

1.2. Magnetic Fields in Star Formation

Historically, the theory of star formation began with a simplified gravitational collapse scenario, in which stars form through the gravitational instability and subsequent collapse of dense cores within molecular clouds (e.g., [21]). However, gravity alone typically underestimates the actual mass threshold necessary for collapse (e.g., [34]). Observationally, star formation efficiencies in molecular clouds are typically very low, on the order of 1–4% (e.g., [35]). This low efficiency suggests that star formation is not only inefficient but also actively slowed by forces other than gravity.

Stars typically form in dense and cold molecular clouds, involving various physical processes such as turbulence, magnetization, gravity, and feedback. However, we do not understand the details of this picture, such as their role and relative contribution to the process. Molecular clouds are also expected to be magnetized, as the magnetic field is thought to be frozen into the ionized material, and undergo interaction between neutral and charged particles. Magnetic fields can regulate the motion of matter (e.g. [36]). Over recent decades, magnetic fields have received increasing attention due to their critical role across multiple scales—from cloud-scale structures down to individual protostellar disks. Thus, understanding the relative importance of magnetic fields compared to gravity and turbulence is essential for a comprehensive theory of star formation.

The following subsection reviews several metrics of the magnetic field's relative importance in the ISM, including their comparisons with gravity and turbulence. Note that the values may change with size and density scale.

1.2.1. Relative Importance of Magnetic Fields versus Gravity

Mass-to-flux ratio

The mass-to-magnetic flux ratio, M/Φ (commonly called the mass-to-flux ratio), is an important quantity for evaluating the role of magnetic fields compared with gravity in the star formation process [37]. It is usually expressed relative to its critical value,

$$\lambda = \frac{(M/\Phi)_{\rm observed}}{(M/\Phi)_{\rm critical}} = 7.6\times10^{-21}\frac{N(\mathrm{H_2})}{B_{\rm POS}} \tag{1.8}$$

where the critical mass-to-flux ratio $(M/\Phi)_{\rm critical} = \frac{1}{2\pi\sqrt{G}}$ [38], $N(\mathrm{H_2})$ is the column density of the region under consideration in units per square centimeter, and $B_{\rm POS}$ is magnetic field strength in the plane of the sky given in units of microgauss.

The mass-to-flux ratio, λ, measures the relative importance of gravity compared to magnetic support in a molecular cloud. It is a critical parameter for estimating the stability of magnetized regions against gravitational collapse. A subcritical value, $\lambda < 1$, indicates that the magnetic field is strong enough to support the cloud against gravity, effectively preventing collapse. In contrast, a supercritical region ($\lambda > 1$) suggests that gravitational forces overcome magnetic support, allowing the cloud to collapse and potentially form stars.

Molecular clouds are observed to be predominantly magnetically critical (Figure 1.5) through Zeeman detections, while diffuse ISM is subcritical [37]. Magnetic fields are not

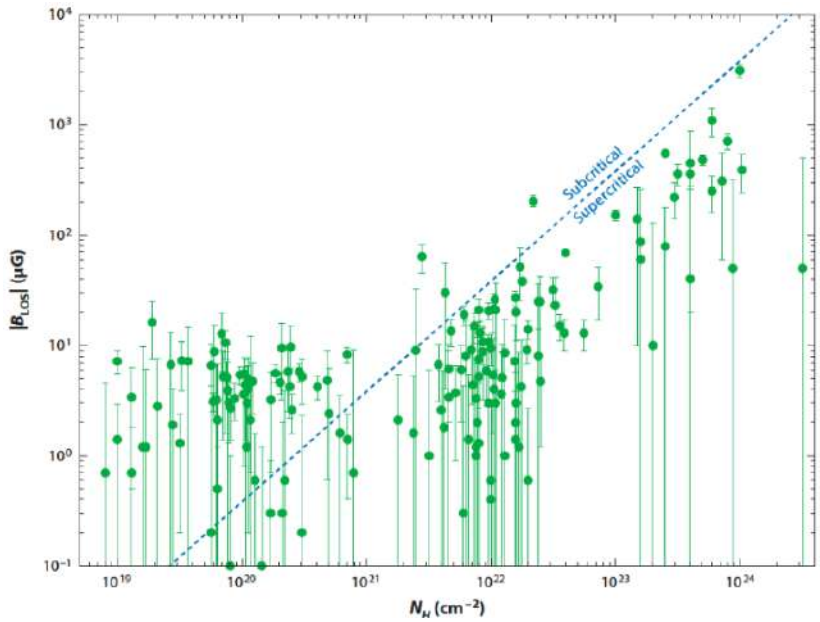

Figure 1.5: Dependence of the line-of-sight magnetic field strength on column density in the ISM by Zeeman measurements. The dashed lines separate the super- and subcritical conditions. Figure taken from [37].

strong enough to support dense clouds against gravitational collapse. The relation of the mean magnetic field strength with density shows that when the column density is below 10^{21} cm^{-2}, the magnetic field strength remains constant. This relation explains how gravitational contraction occurs relative to magnetic field lines. Diffuse clouds accumulate matter along magnetic field lines, increasing density without affecting the field strength [37]. At higher densities, gravity contracts the clouds by self-gravity, boosting the magnetic field under flux-freezing conditions; hence, the magnetic field strength increases with density.

1.2.2. Relative Importance of Magnetic Field versus Turbulence: Strong and Weak Field Models

Turbulence plays a crucial role in the structure and evolution of the ISM and molecular clouds. Turbulence in molecular clouds introduces kinetic energy and creates density fluctuations that can both resist and trigger gravitational collapse, depending on the scale and intensity of turbulent motions. The relative importance of turbulent motion and magnetic fields to the formation and evolution of molecular clouds is a much-debated question. Different models describe different roles of the magnetic fields, such as weak-field and strong-field models [37]. In the former, turbulence plays a decisive role in the formation of new stars, while in the latter, magnetic fields control the formation and evolution of molecular clouds. The relative importance and the roles played by turbulence and magnetic fields may vary during the star formation process. Stars must form from magnetically supercritical (gravitationally unstable) cores; these cores are thought to be embedded in magnetically subcritical molecular clouds (e.g. [39]). The cloud is supercritical when the mass-to-flux ratio is greater than unity and subcritical otherwise. Therefore, investigating this parameter is an efficient way to test star formation models.

Turbulence in astrophysical environments can be broadly categorized into two regimes: hydrodynamic turbulence and magnetohydrodynamic turbulence, depending on whether magnetic fields are dynamically important.

Hydrodynamic turbulence refers to the chaotic, non-linear motions of fluid without the influence of magnetic fields. It is characterized by compressible and incompressible motions across a wide range of spatial scales. The sonic Mach number, $\mathcal{M}_s = \sigma_v / c_s$, quantifies the strength of hydrodynamic turbulence and is defined as the ratio of the turbulent velocity dispersion, σ_v, to the sound speed, c_s. A value of $\mathcal{M}_s > 1$ indicates supersonic turbulence, which is common in molecular clouds and can lead to the formation of shocks and density enhancements.

However, in this thesis, the primary focus is on the role of magnetic fields in star formation. Therefore, I focus on the analysis and interpretation of magnetized turbulence.

Alfvénic Mach number

Magnetohydrodynamic turbulence occurs when magnetic fields are present and interact with the turbulent motions of the ionized or partially ionized gas. The influence of turbulence relative to magnetic fields is measured by the Alfvénic Mach number, $\mathcal{M}_A$, which measures the ratio of turbulent speed to the Alfvén speed, v_A, (the speed at which disturbances propagate along magnetic field lines). $\mathcal{M}_A$ is an important parameter for describing the evolution of molecular clouds [22]. The Alfvénic Mach number, $\mathcal{M}_A$, quantifies the relative importance of turbulence compared to magnetic fields. A sub-Alfvénic condition ($\mathcal{M}_A < 1$) indicates that magnetic fields dominate over turbulence, suggesting a strongly magnetized environment. Conversely, a super-Alfvénic condition ($\mathcal{M}_A > 1$) implies that turbulence is the dominant force, with magnetic fields playing a relatively minor role. In the latter scenario, the magnetic field morphology is expected to be strongly influenced by turbulent motions, resulting in a more disordered or random field structure. In the super-Alfvénic regime, turbulence strongly influences the magnetic field morphology. Therefore, the morphology of the magnetic field is expected to be random. The Alfvénic Mach number, $\mathcal{M}_A$, can be estimated from the velocity dispersion, σ_v, as [40, 41]:

In the super-Alfvénic regime, the magnetic field becomes less dominant than turbulence, so its morphology is strongly influenced by turbulent motions. As a result, the magnetic field structure is expected to appear more random. Following [40] and [41], the Alfvénic Mach number, $\mathcal{M}A$, can be estimated from the velocity dispersion, σv, as:

$$\mathcal{M}_A = \frac{\sigma_v}{v_A} = \frac{\sigma_v \sqrt{4\pi\rho}}{B} \tag{1.9}$$

where $v_A = \frac{B}{\sqrt{4\pi\rho}}$ is the Alfvénic speed and ρ is the gas density.

1.2.3. Multiscale Magnetic Fields: Theory Confronting Observations

Magnetic fields in star-forming regions vary from μG to mG [37]. For a dense core, magnetic field models show an hourglass morphology centered on its center of mass because the field is 'frozen' to the small fraction of charged particles. An example of the model can be seen in Figure 1.6 [42]. The hourglass has been seen in a number of observations of low-mass protostellar cores. This means that the protostellar cores form in strongly magnetized regions. Figure 1.6 (center) shows an example of the hourglass-shaped magnetic field morphology toward the class 0 protostar L1157 [43]. However, observations of starless cores do not show clear hourglass morphologies (see Figure 1.6 right).

The magnetic field orientation across multiple spatial scales is an interesting topic. In a strong-field region, the magnetic-field orientation is consistent across multiple scales [45]. In low-mass regions, a consistent magnetic field orientation has been observed in the Orion molecular cloud across scales ranging from $\sim$ 100 pc down to $\sim$ 1,000 au [47, 43]. However,

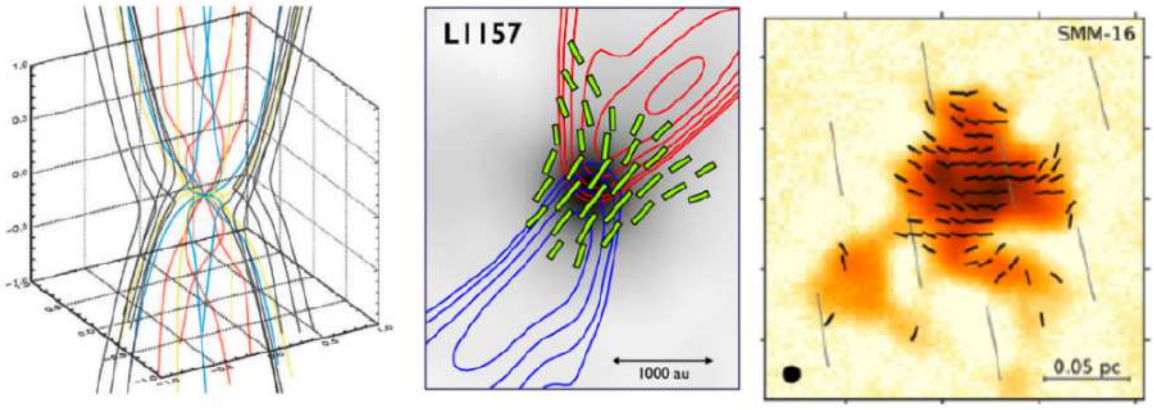

Figure 1.6: Left: A model of a collapsing, magnetized star-forming core showing hourglass-shaped magnetic field morphology [42]. Center: Observations of hourglass-shaped magnetic fields of the Class 0 protostar L1157 (line segments) [43]. Right: Map of magnetic fields towards the starless core L1689 SMM-16 (line segments) [44].

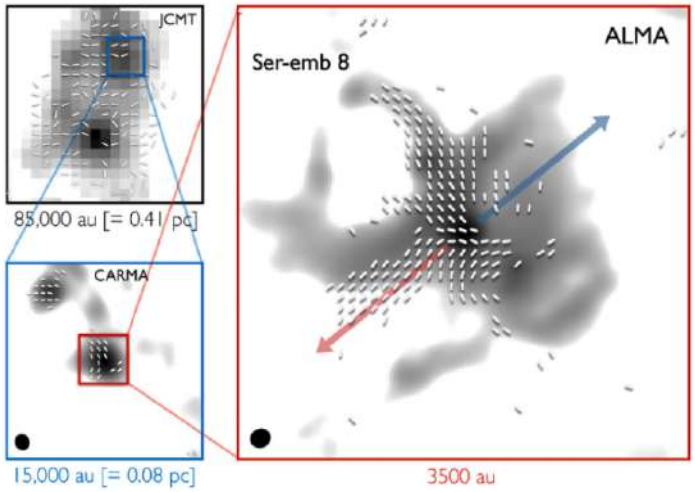

Figure 1.7: Multiscale observations of the magnetic fields toward the low-mass Class 0 protostar Ser-emb 8. The line segments show the orientation of the magnetic fields overplotted on the intensity map. Observations are from the JCMT at 850 μm, CARMA[1] at 1.3 mm, and ALMA at 870 μm. The red and blue arrows represent the bipolar outflow. This figure is adapted from [45].

the field morphology is not the case for Ser-emb 8 as shown in Figure 1.7. MHD simulations suggest that Ser-emb 8 may have formed in an environment where turbulence and infall dominate the magnetic fields [48].

Magnetic fields play a potentially dynamic role in the formation and evolution of filaments across different scales [39]. Moreover, the role of magnetic fields in the formation of filaments is likely vital because it makes the flow more coherent, therefore, allowing filaments to survive longer (see [49] for a review).

Observations of the magnetic fields surrounding filaments show a statistical correlation between the orientation of cloud structure and the magnetic field morphology. The dense filaments are perpendicular to the local magnetic field direction, while lower-density filaments tend to be parallel to the magnetic field [50]. Figure 1.8 shows that sub-filaments or 'stria-

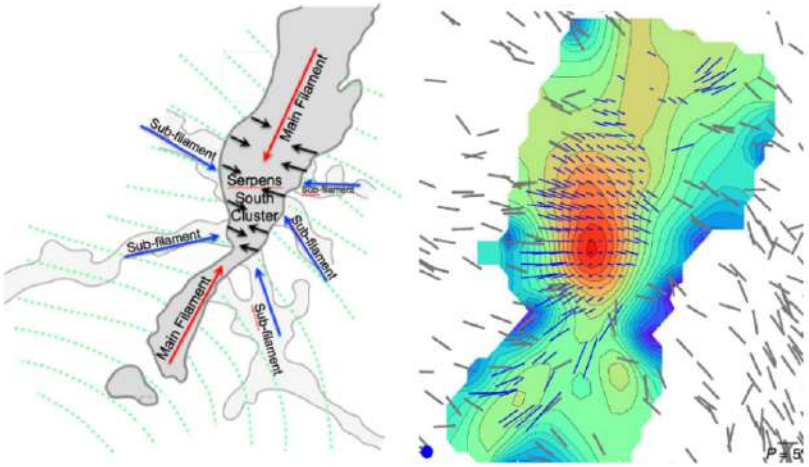

Figure 1.8: The Serpens South cloud. Left: An illustration of the model of magnetically-regulated filament formation [11]. Right: Magnetic field map (line segments) from HAWC+ 214 μm data [46].

tions' can be seen perpendicular to the main filament in the Serpens South molecular cloud, and parallel to the magnetic fields. Andre et al. [11] proposed a theory of magnetically-regulated material flows onto filaments along magnetic field lines, so that the material from outside the filament can flow to the main filament through striations.

1.2.4. Measuring Magnetic Fields

Measuring ISM magnetic fields is truly challenging; the magnetic field strengths in molecular clouds are thousands or tens of thousands of times lower than those of the Earth. Since the first discovery of interstellar magnetic fields in the ISM using starlight polarization caused by dichroic extinction of aligned dust grains [51, 52], the study of magnetism in star formation has attracted serious attention in the last few decades.

Several observational techniques have been developed to detect and characterize magnetic fields, including synchrotron radiation, Faraday rotation, Zeeman splitting, and dust polarization (including starlight polarization and thermal dust emission polarization).

Synchrotron radiation originates from relativistic electrons spiraling around magnetic field lines and emits strongly polarized radiation in the radio regime. This technique is especially effective for tracing large-scale magnetic fields in diffuse, ionized environments such as galactic halos or supernova remnants. However, synchrotron emission is generally absent in dense molecular clouds due to the lack of relativistic particles, making it unsuitable for studying the magnetic fields directly involved in star formation.

In the context of the ISM and molecular clouds, the most commonly used techniques are Faraday rotation, Zeeman measurements, and dust polarization. Each method probes different components of the magnetic field and is sensitive to different physical conditions. Therefore, in the following subsections, I describe these methods in more detail.

1.2.4.1. Faraday Rotation

Faraday rotation occurs when linearly polarized light passes through a magnetized medium, such as the ISM, which is permeated by free electrons and magnetic fields. As light travels through this medium, the polarization angle is changed, which depends on the magnetic field strength and the electron density along the line of sight. The amount of rotation, Ψ in Figure

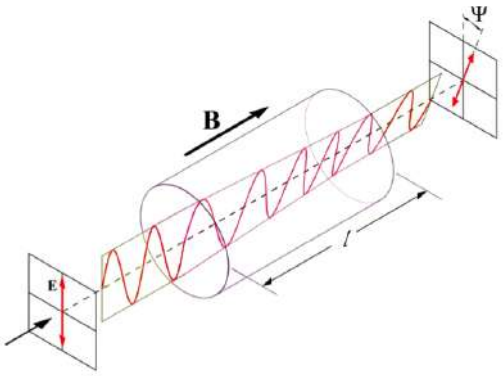

Figure 1.9: Polarization rotation due to the Faraday effect. When a linearly polarized light goes through a magnetized region with free electrons, its polarization plane is rotated by an angle Ψ.

1.9, is given by:

$$\Psi = \lambda^2 \left(0.812 \int n_e B.dl \right), \tag{1.10}$$

where B is the magnetic field strength in μG, Ψ is in radians, λ is the wavelength in m, dl is the path length through the magnetized region in pc, and n_e is the volume electron density in particles/cm^3.

Faraday rotation has not been commonly used to observe the magnetic fields in molecular clouds. One of the main reasons is that the molecular clouds are mostly neutral and could not possibly induce significant Faraday rotation. Moreover, it is difficult to estimate the electron density and the path length.

Tahani et al. [53] proposed and demonstrated a new method to use Faraday rotation measurements in and around filamentary molecular clouds, Orion A, Orion B, Perseus, and California. They found the direction and strength of the magnetic fields along the line of sight and suggested the bow-shaped magnetic morphology.

1.2.4.2. Zeeman Splitting

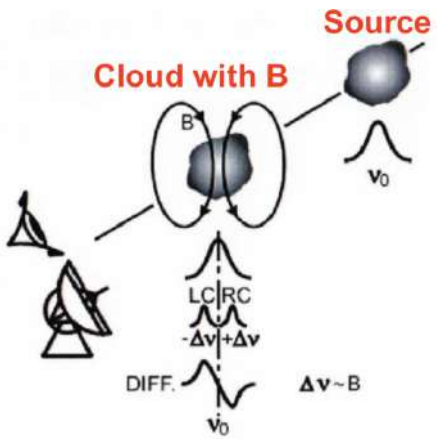

Figure 1.10: Schematic of the Zeeman effect in a cloud with the presence of a magnetic field, B), which causes the splitting of spectral lines.

Zeeman splitting of line emission is the only way to directly measure the strengths of the line-of-sight magnetic field component [54]. Zeeman splitting refers to the splitting of a single spectral line into multiple magnetically shifted components when molecular energy levels is lifted in the presence of an external magnetic field. Figure 1.10 illustrates the Zeeman effect in a cloud with a magnetic field, B, which causes the splitting of spectral lines. A source emits unpolarized radiation at a frequency v_0. As the radiation passes through the cloud, the magnetic field splits the frequency into two radiations at $v_0 + \Delta v$ and $v_0 - \Delta v$. Δv is proportional to the strength of the magnetic field, B, and can be calculated as:

$$\Delta v = \pm \frac{eB}{4\pi m_e c}, \tag{1.11}$$

where e is the charge of an electron, m_e is the mass of an electron, and c is the speed of light.

However, Zeeman splitting is typically very small, making Zeeman observations highly sensitive to noise and thus limited by sensitivity. Due to the relatively weak magnetic fields in molecular clouds, frequency shifts are very small. Even with very high-sensitivity instruments, Zeeman measurements require extremely high sensitivity and long telescope integration times. Therefore, Zeeman measurements are very time-consuming and costly. Although Zeeman measurements are the only direct way to provide the line-of-sight magnetic field component, there are limitations to Zeeman detections in molecular clouds because of these challenges.

1.2.4.3. Dust Polarization

The first observations of magnetic fields in the ISM started with polarization of starlight caused by dichroic extinction of aligned non-spherical grains [51, 52]. Thermal emission from such aligned dust grains in far-infrared and submm is also polarized due to dichroic emission, usually called dust polarization (see more details in Section 1.3.1.3). Dust polarization is the key observation for studying magnetic fields in terms of morphology and strength, which can be used at a wide range of wavelengths, most of which are ranges of density and size scales, from the ISM to protostellar environments. Furthermore, studying the dust polarization data also allows us to obtain dust properties such as size and structure, and to study dust alignment physics in magnetic fields. The main assumption in this technique is that dust grains align their major axis perpendicular to the magnetic fields (e.g. [55, 56] see Figure 1.13). The currently accepted explanation is the Radiative Torque Alignment (RAT-A) mechanism.

The dust polarization technique has been widely used to map magnetic fields in molecular clouds and giant molecular clouds. Specifically, the *Planck* Space Observatory observed the plane-of-sky map of the magnetic fields. Besides, there are several surveys that have provided dust polarization observations in different star-forming regions and at different scales, e.g., BLASTPol, James Clerk Maxwell Telescope BISTRO survey (B-fields in Star-forming Region Observations) [39, 57, 58].

The strength of the plane-of-sky component of the magnetic fields can be estimated using the Davis-Chandrasekhar-Fermi method (DCF; [36, 23]. The method assumes that the gas turbulent motions will lead to random distortion in the magnetic fields because of the field freezing in the gas.

$$B_{\rm POS} = Q\sqrt{4\pi\rho}\frac{\sigma_V}{\sigma_\theta} \approx 9.3\sqrt{n(\mathrm{H_2})}\frac{\Delta V}{\sigma_\theta} \quad (\mu G) \tag{1.12}$$

where Q is the factor applied to correct for the smoothing of magnetic field tangling, with a Q value of 0.5 [59]. σ_θ represents the dispersion of the angles of the polarization position in degrees, and $n(\mathrm{H_2})$ is in units of $\mathrm{cm^{-3}}$. ρ denotes the gas density, σ_V is the one-dimensional non-thermal velocity dispersion in km $\mathrm{s^{-1}}$, and $\Delta V = 2.355\sigma_V$.

Zeeman measurements provide direct constraints on the line-of-sight magnetic field, but they are observationally expensive due to their requirement for high spectral sensitivity and long integration times. While dust polarization enables detailed mapping of the plane-of-sky magnetic field morphology and allows for indirect estimation of magnetic field strength across various spatial scales and environments.

In this thesis, I focus on studying magnetic fields and dust in star-forming regions using thermal dust emission and polarization, which provides insights into both the structure and strength of magnetic fields in dense environments. Moreover, thermal dust polarization can also be used to probe dust physics, such as grain alignment and composition, which is crucial for interpreting polarization observations accurately.

1.3. Dust Physics

Although interstellar dust contributes a relatively small mass fraction of the ISM (less than 1%, [60]), dust plays an important role in astrophysics. Dust grains are important for the cooling mechanism, are central to the chemistry of interstellar gas, and for coupling the magnetic field to the gas. Moreover, dust also locks up much of the heavy elements in solid form and provides matter for the building pebbles, planetesimals, and planets. It is important to note that the field of dust physics is vast; in this Introduction, I focus on key observational aspects of dust, as well as the physics of grain alignment and grain evolution (disruption and growth).

1.3.1. Dust Observations

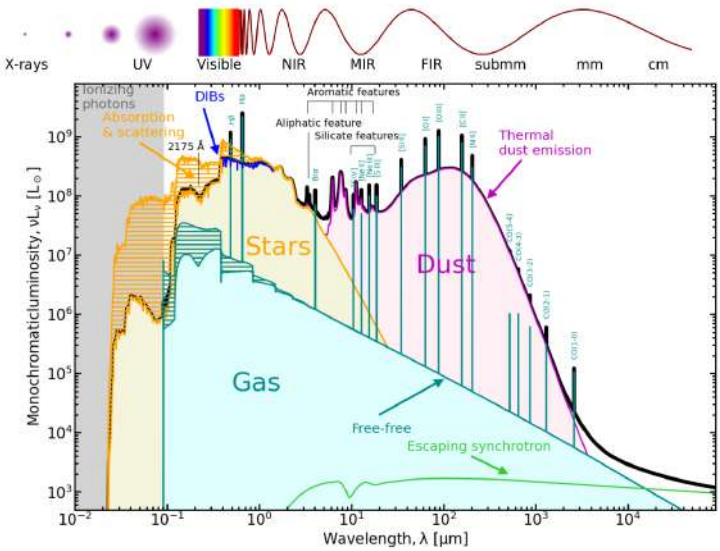

Figure 1.11: Spectral energy distribution (SED) of a synthetic, typical late-type galaxy. The top panel schematically indicates the different spectral regimes. In the main panel, the total simulated spectrum (black) is decomposed into several components: escaping stellar emission (orange), thermal dust continuum (magenta), gas emission lines, free-free continuum (dark cyan), and synchrotron continuum (green). Adopted from [61, 62].

When observing a galaxy or star-forming region at different wavelengths, from the UV

to the radio, Figure 1.11 shows the synthetic SED. This figure shows that the different stellar populations dominate the UV-optical domain, whereas dust dominates the infrared/submillimeter. Therefore, the study of dust physics is mainly in the infrared and (sub)millimeter wavelengths. Direct observational studies of interstellar dust all rely on our understanding of the interaction of grains with electromagnetic waves. The three primary methods used to observe dust are extinction, continuum emission, and polarization.

1.3.1.1. Interstellar Dust Extinction

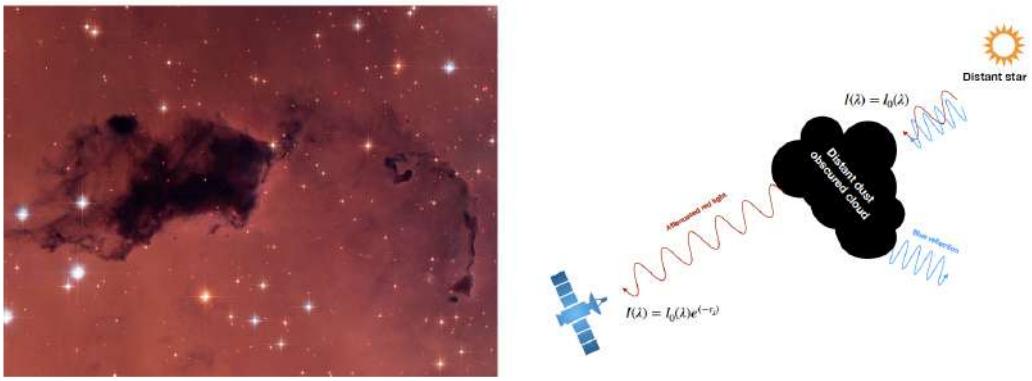

Figure 1.12: Dust extinction. Left: A dust-obscured cloud in NGC281 observed by the *Hubble* Space Telescope. Right: A schematic illustration of the dust extinction process. Blue light is almost entirely absorbed by dust, whereas part of the red light is able to pass through. A blue reflection, due to scattering by the dust grains, can be observed.

The phenomenon of extinction was first noted in the early 20th century by [63], who observed what appeared to be an "absence of stars" and correctly interpreted it as the presence of a "dark nebula." Later, [64] demonstrated that this dimming of starlight is caused by fine interstellar dust particles. When photons emitted by a star pass through an interstellar cloud containing both dust and gas, they can be absorbed or scattered by dust grains—an effect known as dust extinction.

If we consider an incident radiation field $I_0(\lambda)$ that enters in a cloud, the radiation field leaving this cloud (with the hypothesis that there are no sources of energy in the cloud) can be expressed as:

$$I(\lambda) = I_0(\lambda) exp(-\tau_\lambda), \tag{1.13}$$

with $\tau_\lambda = \tau_{\lambda,\text{abs}} + \tau_{\lambda,\text{sca}}$ is the optical depth of the cloud.

Dust extinction can be quantified by the following parameter, simply called the extinction, expressed in magnitudes:

$$A_\lambda = -2.5 \log\left(\frac{I(\lambda)}{I_0(\lambda)}\right) \tag{1.14}$$

or, for implications,

$$A_\lambda \simeq 1.086 \tau_\lambda \tag{1.15}$$

The extinction allows for the estimation of the optical depths of the cloud, which can be linked to the opacity and the grain properties.

By fitting the interstellar extinction curve from the infrared to the ultraviolet, and assuming that dust grains are composed of graphite and silicates, [60] derived a model for the grain size distribution in the diffuse ISM. This distribution, commonly known as the Mathis–Rumpl–Nordsieck (MRN) size distribution, is described by a power law with index α:

$$n(a_{\rm grain}) \propto a_{\rm grain}^{-\alpha} \tag{1.16}$$

with $n(a_{\rm grain})$ is the number density, and grain size is vary from nm to μm. The power-law index α is around 3.5 for ISM.

1.3.1.2. Continuum Emission

Interstellar dust studies often focus on the infrared/submillimeter spectrum. The shape of the FIR/submillimeter spectrum is roughly similar to a modified blackbody; it is usually used for SED fitting. It originates from the emission of large grains (0.02–0.3 μm), which are at equilibrium with the radiation field.

Incident stellar radiation heats the dust, which then emits thermal radiation according to its temperature, $T_{\rm d}$. The thermal emission from a dust grain at temperature $T_{\rm d}$ is described by the Planck function:

$$B_\nu(T_{\rm d}) = \frac{2h\nu^3}{c^2} \frac{1}{e^{\frac{h\nu}{k_B T_{\rm d}}} - 1} \tag{1.17}$$

where $T_{\rm d}$ is the temperature of the dust, h is the Planck constant, ν is the frequency of the observations, c is the speed of light in a vacuum, and k_B is the Boltzmann constant.

The emissivity (power per unit volume) of thermal dust emission is the integration over the different grain sizes of the given temperature T_d is calculated as

$$j_\nu(T_{\rm d}) = \int n(a) C_{\rm abs} B_\nu(T_{\rm d}) da \tag{1.18}$$

where $n(a)$ is the grain size distribution and $C_{\rm abs}$ is the absorption cross-section.

The intensity of thermal dust emission integrated along the line of sight is given by

$$I_\nu = (1 - e^{-\tau_\nu}) B_\nu(T_{\rm d}) \tag{1.19}$$

where the optical depth is given by

$$\tau_\nu = \kappa_\nu \times \mu_{\rm H} m_{\rm H} \times N_{\rm H} \tag{1.20}$$

where $\kappa_\nu = \int n_{\rm d}(a) C_{\rm abs} da$ is the dust opacity, and $\mu_{\rm H}$ is the molecular weight, and $N_{\rm H}$ is the hydrogen column density.

In far-IR/submillimeter of long wavelengths, the dust opacity can be approximately given by a power law:

$$\kappa_\nu = \kappa_0 \left(\frac{\nu}{\nu_0}\right)^\beta \tag{1.21}$$

where β is the dust emissivity spectral index, which ranges from 1 to 2, depending on the dust composition and size distribution, and κ_0 is the dust opacity measured at frequency ν_0.

As a result, in the case of optically thin of $\tau_\nu \ll 1$, the total emission intensity becomes

$$I_\nu(T_\mathrm{d}) \approx \tau_\nu B_\nu(T_\mathrm{d}) = \kappa_0 \left(\frac{\nu}{\nu_0}\right)^\beta B_\nu(T_\mathrm{d}) \mu_\mathrm{H} m_\mathrm{H} N_\mathrm{H}. \tag{1.22}$$

Equation 1.22 accounts for the emission from the modified blackbody and is valid for the case of optically thin, which is typical for the far-IR/submillimeter in the ISM and star-forming regions. From the above equation, one can derive the gas column density N_H when the continuum emission intensity I_ν is observed.

1.3.1.3. Dust Polarization

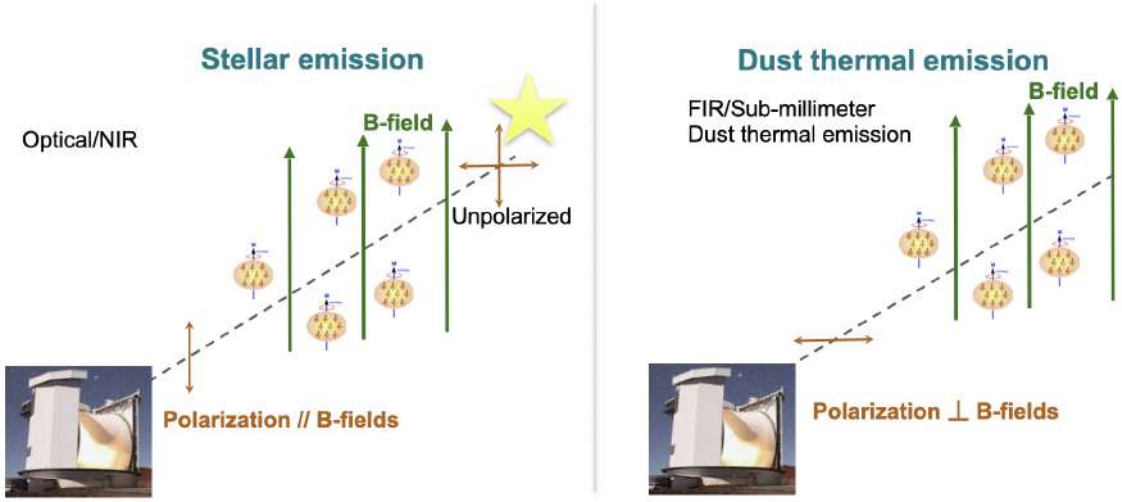

Figure 1.13: Cartoon of dust polarization by grain alignment theory. The major axis of the dust grains (orange ellipses) is aligned perpendicular to the cloud's magnetic field (green line). In optical or NIR wavelengths (left panel), the polarization direction (brown arrow) from distant starlight is parallel to the magnetic field. In FIR or sub-millimeter wavelengths (right panel), the polarization direction from dust thermal emission is perpendicular to the magnetic field.

Interstellar dust grains are typically non-spherical, and their elongated shapes are crucial in producing observable polarization signals. When these grains align with the magnetic field, they selectively absorb and emit radiation depending on their orientation. This alignment can be observed in two main contexts: polarization of starlight and polarization from dust thermal emission. Starlight polarization occurs because aligned grains preferentially absorb radiation polarized parallel to their long axes, thus transmitting radiation polarized parallel to the magnetic field. In contrast, polarization from dust thermal emission is due to the grains preferentially emitting radiation polarized along their longer axes, also perpendicular to the magnetic field lines. Hence, the thermal dust polarization direction is also perpendicular to the magnetic field. Both phenomena are complementary diagnostic tools for examining magnetic field structures and grain alignment processes in the ISM.

Figure 1.13 illustrates the starlight and dust thermal polarization. In optical or NIR wavelengths, the direction of starlight polarization is parallel to the direction of the magnetic fields. In the submillimeter wavelength, the direction of thermal emission polarization of the dust is perpendicular to the direction of the magnetic fields.

Stokes Parameters

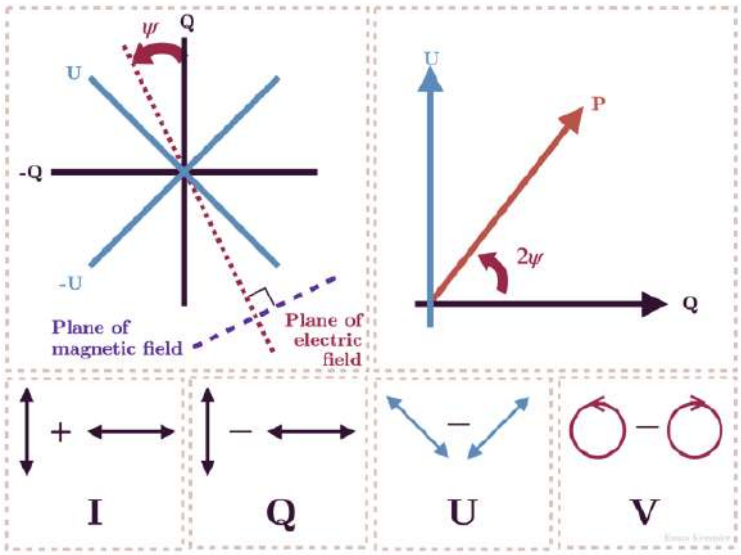

Figure 1.14: Illustration of the Stokes parameters, I, Q, U, V.

The measure of polarization used in astronomy is based on the set of four parameters introduced by Sir George Stokes in 1852, known as the Stokes parameters.

Let's consider a monochromatic plane wave propagating along the z-axis. The electric field vector $\boldsymbol{E}(t,z)$ oscillates in the transverse xy-plane and can be decomposed into two orthogonal components:

$$\boldsymbol{E}_x(t,z) = E_{0,x}\cos(\omega t - kz)\,, \tag{1.23}$$
$$\boldsymbol{E}_y(t,z) = E_{0,y}\cos(\omega t - kz + \delta_{xy})\,, \tag{1.24}$$

where $E_{0,x}$ and $E_{0,y}$ are the constant amplitudes along the x- and y-directions, respectively, and δ_{xy} is the phase difference between the two components. The polarization state of the wave depends on the amplitude ratio and phase difference. If $\delta_{xy} = 0$ and $E_{0,x}$, $E_{0,y}$ are constant, the wave is linearly polarized. If $E_{0,x} = E_{0,y}$ and $\delta_{xy} = \pm\pi/2$, the wave is circularly polarized. if $E_{0,x} \neq E_{0,y}$ and $\delta_{xy} \neq 0$, the wave is elliptically polarized.

In astronomy, the polarization is described using the Stokes parameters I, Q, U, V, introduced by Stokes (1852). These parameters, defined as time-averaged quantities, are given by:

$$I = \langle E_{0,x}^2\rangle + \langle E_{0,y}^2\rangle, \tag{1.25}$$
$$Q = \langle E_{0,x}^2\rangle - \langle E_{0,y}^2\rangle, \tag{1.26}$$
$$U = 2\langle E_{0,x}E_{0,y}\cos(\delta_{xy})\rangle, \tag{1.27}$$
$$V = -2\langle E_{0,x}E_{0,y}\sin(\delta_{xy})\rangle. \tag{1.28}$$

I represents the total intensity of the radiation, independent of polarization. Q and U characterize the linear polarization. Q quantifies the difference in intensity between horizontal and vertical polarization components, while U measures the difference between linear polarization at $+45^\circ$ and -45° orientations. V describes the circular polarization, representing the difference between right-handed and left-handed circularly polarized light. In the case

of thermal dust emission, V is typically negligible and is not measured in most astrophysical polarimetric observations.

Linear Polarization from Thermal Dust Emission

In the case of linear polarization, the state of polarization is described by the Stokes parameters I, Q, and U. Due to the presence of noise in the measurements of Q and U, a debiasing correction is typically applied when computing the polarized intensity. The debiased polarized intensity is calculated as [65]:

$$PI = \sqrt{Q^2 + U^2 - 0.5(\delta Q^2 + \delta U^2)}, \tag{1.29}$$

where δQ and δU are the uncertainties on Q and U, respectively. Assuming that δQ and δU are uncorrelated, the uncertainty on PI is [66]

$$\delta PI = \sqrt{\frac{Q^2\delta Q^2 + U^2\delta U^2}{Q^2 + U^2}}. \tag{1.30}$$

The polarization degree, P, and its uncertainty, δP, are calculated as

$$P(\%) = 100 \times \frac{PI}{I}, \tag{1.31}$$

and

$$\delta P(\%) = 100 \times \sqrt{\frac{\delta PI^2}{I^2} + \frac{\delta I^2(Q^2 + U^2)}{I^4}}, \tag{1.32}$$

where δI is the uncertainty on I which is provided together with I from observations.

The polarization angle, θ, and its uncertainty, $\delta\theta$, are calculated as follows:

$$\theta = \frac{1}{2}\text{atan2}\left(\frac{U}{Q}\right) \tag{1.33}$$

$$\delta\theta = 0.5 \times \frac{\sqrt{U^2\delta Q^2 + Q^2\delta U^2}}{(Q^2 + U^2)}. \tag{1.34}$$

For the *Planck* data, θ is calculated as $\theta = \frac{1}{2}\text{atan2}(-U/Q)$ because of the different convention used for the Stokes parameters [67].

The polarization direction of thermal dust emission is perpendicular to the plane-of-sky projection of magnetic fields; therefore, the plane-of-sky magnetic field orientation angles are obtained by rotating 90° from the polarization angle θ. Following the IAU convention, the angles of the magnetic field lines are east of north, ranging from 0° to 180°.

Wavelength Dependence: Serkowski Law for Starlight Polarization

The wavelength dependence of starlight polarization due to dust extinction follows the empirical Serkowski law [68]:

$$P(\lambda) = P_{\max} \exp\left[-K \ln^2\left(\frac{\lambda}{\lambda_{\max}}\right)\right] \tag{1.35}$$

$P_{\max}$ is the maximum polarization fraction at wavelength $\lambda_{\max}$, and K parameterizes the width of the curve [68]. The Serkowski Law reflects how the size, composition, and alignment of dust grains influence polarization. The parameter $\lambda_{\max}$ is particularly important because it correlates with the typical grain size in the intervening medium. A shorter $\lambda_{\max}$ implies smaller grains, while a longer $\lambda_{\max}$ suggests larger grains.

1.3.2. Dust Formation and Evolution

Dust forms from stellar ejecta produced by core-collapse supernovae, asymptotic giant branch stars, giant and supergiant stars, and Wolf-Rayet stars. The composition of dust depends on the type of asymptotic giant branch star, whether it is oxygen-rich or carbon-rich, resulting in different carbon-to-oxygen ratios. The dust mass produced by asymptotic giant branch stars is estimated to be around $10^{-2} - 10^{-3}\ M_{\odot}$ [69]. Supernovae contribute to both types of dust, with a dust yield of approximately 0.1–1 $M_{\odot}$ [70]. Besides, dust grains can grow in dense molecular clouds via accretion from the gas phase.

Interstellar dust evolves through a complex interplay of destruction (sputtering, shattering, and fragmentation), growth, chemical processing, and radiative effects. Dust in diffuse interstellar environments is frequently affected by destructive processes, especially in supernova shock waves and hot gas. Sputtering in shocks, collisions of energetic ions or atoms with grain surfaces, is identified as a main dust destruction mechanism in fast shocks [e.g., 71]. Besides, grain-grain collisions in high-velocity shocks lead to shattering, fragmenting larger grains into many smaller pieces [e.g., 72, 73]. In the dense molecular clouds, UV radiation is attenuated, and gas densities are high ($n_H \sim 10^3 - 10^5$ cm^{-3}); these conditions tend to dust grain growth rather than destruction [e.g., 74]. One important mechanism is coagulation: collisions between grains can lead to sticking and aggregation. Another growth channel is the accretion of gas-phase atoms and molecules onto grain surfaces, forming mantles. These ice mantles not only add mass to the grains (growth by accretion) but also increase the coagulation efficiency. Chemical processing modifies the grain composition and structure, especially in cold, dense regions. Ices, mainly composed of H_2O, CO, CH_3OH, and other simple molecules, can undergo photolysis or cosmic-ray-induced reactions, forming more complex molecules, including organic molecules. UV radiation can photodissociate bonds in small grains, erode their surfaces, and transform carbonaceous grain structures (e.g., from aliphatic to aromatic). When dust grains are illuminated by high radiation fields, large grains will be disrupted into smaller ones by RAT. This process also plays a crucial role in the grain size distribution.

Observational techniques used to constrain dust grain size include extinction curves, SEDs, and polarization measurements. The shape of extinction curves, wavelength-dependent absorption, and scattering of starlight by dust, from the UV through IR, is highly sensitive to the grain size distribution and composition. This can be parametrized by the ratio $R_V = A_V / E(B-V)$, where a higher R_V indicates a flatter (grayer) extinction curve. Diffuse clouds typically have $R_V \simeq 3.1$, whereas some molecular clouds, e.g, Ophiuchus and Perseus cloud, show $R_V \simeq 4 - 6$ [75, 76]. SEDs in the infrared and submillimeter trace dust thermal emission, where a shift to longer wavelengths and increased far-IR opacity signal the presence of larger, more emissive grains. *Planck* 's all-sky analysis noted that dust optical depth rises faster with gas column in molecular clouds than expected from diffuse dust calibrations, and the dust spectral index β tends to be larger in cold regions. This is consistent with fluffier, larger grains that have $\beta \sim 2$, versus $\beta \sim 1.5 - 1.7$ for diffuse ISM dust [77]. Polarization of starlight and dust emission helps infer grain shape and alignment, and elongated grains.

1.3.3. Composition of Dust Grain and Dust Model

Dust refers to a population of solid particles, typically ranging in size from a few nanometers up to about $\sim 1\ \mu$m in the ISM. Figure 1.15 shows an example of a cosmic dust grain collected in the stratosphere, taken with a scanning electron microscope, and presented by [78]. The aggregate is non-spherical, about 10x20 μm. They are mainly composed of O, C, Si, Mg, and Fe, and they have compositions of oxygen (e.g., Al_20_3, Mg_2SiO_4, Fe_3O_4) or carbon-rich

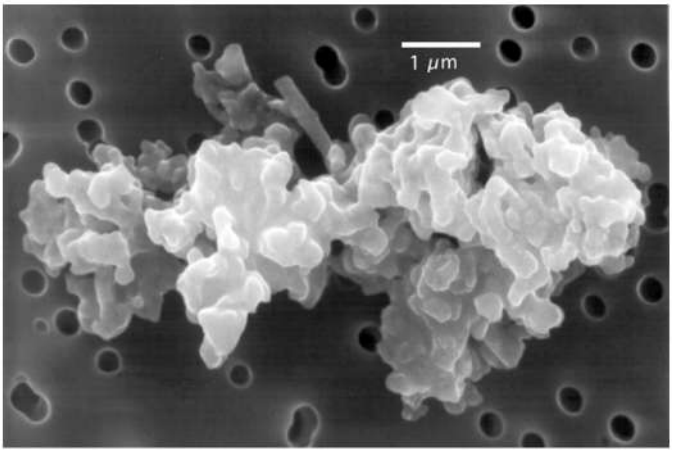

Figure 1.15: Cosmic dust grain collected in the stratosphere taken from [78].

(e.g., SiC, TiC, graphite, amorphous carbon) and mixed with the interstellar gas (e.g., [79]).

A model for interstellar dust must specify the composition of the dust as well as the geometry (shape and size) of the dust particles. Many different interstellar dust models have been proposed; they can be divided into these two broad categories:

- The composite dust model is a mixture of silicate and carbon in a dust grain. The expansion of this model includes polycyclic aromatic hydrocarbons (e.g., [80]).
- The separate dust model is a model where silicate and carbon exist separately. The core-mantle models are composed of a core of silicate or aliphatic carbon, both surrounded by an aromatic carbon mantle.

The silicate dust or composite dust can be aligned with magnetic fields. Note that observational constraints favor the composite model for interstellar dust, such as Astrodust [81] and the THEMIS model [82]. During dust evolution, grains can transition between the composite dust model and the separate dust model. In denser regions of the ISM, coagulation processes can lead to the formation of composite dust grains. Conversely, composite dust can be disrupted under certain conditions, reverting to separate dust grains. These processes can change the shapes and sizes of dust grains.

In the ISM, heavy elements are often depleted from the gas phase and incorporated into dust grains (e.g., [83]), especially iron, with a high condensation temperature (about 1000 K), is efficiently incorporated into dust grains in denser regions of the ISM. Iron atoms may exist in the form of free-flying nanoparticles and/or are incorporated into big grains (either diffuse or cluster distribution), which produce various magnetic materials.

Magnetic materials are classified into the following types: paramagnetic, ferromagnetic (metallic iron), ferrimagnetic, and antiferromagnetic (e.g., [84]). Paramagnetic materials, such as silicates, have a weak magnetization that is aligned with an external magnetic field. The magnetization in these materials is proportional to the strength of the applied field and depends on the material's paramagnetic susceptibility. Ferromagnetic materials, such as metallic iron, cobalt, and nickel, have unpaired electrons, which result in intrinsic magnetization even without an external field. These materials have strong, permanent magnetization and have much higher magnetic susceptibility than paramagnetic materials. Iron particles at low temperatures tend to be ferromagnetic, while at higher temperatures, the particles become superparamagnetic. Ferrimagnetic materials, like iron oxides (Fe_3O_4, Fe_2O_3), also possess intrinsic magnetization, but net magnetization that is weaker than that of ferromagnetic materials. Finally, antiferromagnetic materials, such as Fe_2SiO_4, have a structure where

the magnetic moments of adjacent atoms or ions are aligned in opposite directions, canceling each other out and resulting in no net magnetization in the absence of an external field. Each type of material has distinct properties that influence its behavior in magnetic environments, as well as its alignment with the magnetic fields in the ISM (e.g., [85]).

1.3.4. Theory of Grain Alignment

The polarization of light induced by interstellar dust grains is a long-standing problem in astrophysics; it suggests that dust grains having an aspherical shape must be aligned systematically in the ISM (e.g., [52, 51]). Over the last 70 years, several physical mechanisms have been proposed to align dust grains.

Before the development of RAT theory, grain alignment was explained by the paramagnetic relaxation mechanism, also known as the Davis–Greenstein (DG) mechanism [86]. In this process, rotating paramagnetic grains experience a lag in their magnetization relative to the external magnetic field, resulting in magnetic dissipation. This energy loss gradually aligns the grain's angular momentum vector with the magnetic field. However, the DG mechanism alone is generally too inefficient in dense molecular clouds due to its long alignment timescale compared to the randomization timescale by gas collisions [55].

The key mechanism to align dust grains in the ISM and molecular clouds is by radiative torques (RATs), first introduced by [87] and later developed numerically by [88]. A more comprehensive analytical formulation was provided by [55, 89]. The RAT theory describes how anisotropic radiation fields exert torques on irregularly shaped dust grains, spinning them up to suprathermal rotation and aligning them with the ambient magnetic field (e.g., [89, 56]).

Besides magnetic fields, depending on grain properties and the local environment, dust grains can also align with other preferred directions, such as the radiation field. However, in molecular clouds and the ISM, dust grains are most likely to align with magnetic fields [90].

In this thesis, I focus only on the RAT paradigm, which includes both Radiative Torque Alignment (RAT-A) and Radiative Torque Disruption (RAT-D).

1.3.4.1. Radiative Torque Alignment (RAT-A)

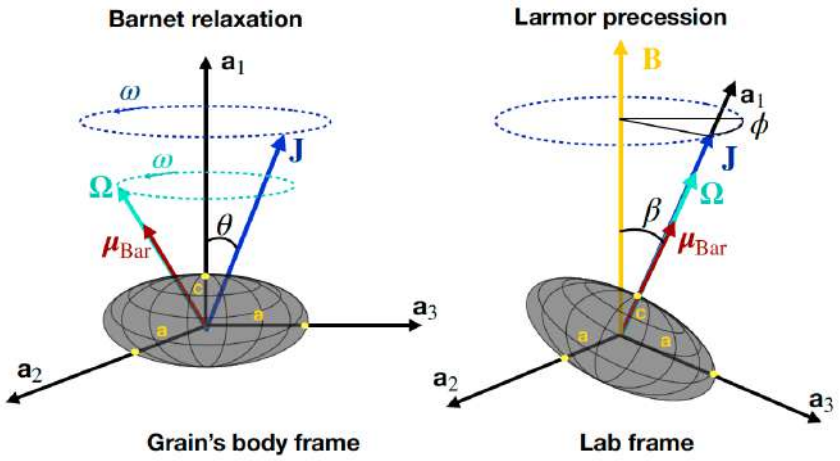

Figure 1.16: Left-hand panel: Illustration of the internal alignment due to Barnett relaxation. Right-hand panel: Illustration of Larmor precession due to the magnetic torques. This figure is taken from [91].

The process of grain alignment includes two processes (1) internal alignment: the alignment of the axis of the maximum moment of inertia, $\boldsymbol{a}_1$, with the grain angular momentum, $\boldsymbol{J}$; and (2) external alignment: the alignment of the angular momentum with ambient magnetic fields, $\boldsymbol{B}$. When non-spherical dust grains are exposed to an anisotropic radiation field, the interaction between the incident photons and the grain's asymmetric shape generates radiative torques. The radiative toques spin up the dust grains. Magnetically dust grains are composed of paramagnetic or ferromagnetic materials. The rotating dust grain can generate a magnetic moment, $\boldsymbol{\mu}_{\rm Bar}$, through the Barnett effect [92], alignment of unpaired electron spins due to grain rotation. The time-varying magnetization in a grain whose angular momentum $\boldsymbol{J}$ is not aligned with its principal axis $\boldsymbol{a}_1$ leads to dissipation of rotational energy in the grain body, a process known as Barnett relaxation. Together with inelastic relaxation, these internal relaxation mechanisms drive $\boldsymbol{a}_1$ to align with $\boldsymbol{J}$, producing internal alignment [93], see left panel of Figure 1.16.

The Barnett effect induces the grain's magnetic moment. Then, the interaction between the grain's magnetic moment, $\boldsymbol{\mu}_{\rm Bar}$, and the magnetic field, $\boldsymbol{B}$, causes the precession of the angular momentum around the external magnetic field direction. This motion is known as Larmor precession, see right panel of Figure 1.16. If the Larmor precession of the grain angular momentum around the magnetic field is very fast compared to the gas damping time, the magnetic field becomes an axis of grain alignment. The two processes require magnetic material, as introduced in Section 1.3.3, to align with the magnetic field.

Let's consider a radiation field having a total energy density $u_{\rm rad} = \int u_\lambda d\lambda$ (erg cm^{-3}). The radiation strength is defined as $\mathcal{U} = u_{\rm rad}/u_{\rm ISRF}$, where $u_{\rm ISRF} = 8.64\times10^{-13}$ (erg cm^{-3}) is the radiation energy density of the interstellar radiation field (ISRF) in the solar neighborhood [94].

These radiative torques cause the grain to spin up, reaching high angular velocities. Grains can reach suprathermal rotation speeds due to the effect of RATs [95]. However, competing processes, such as gas collisions and infrared (IR) re-emission, act to spin down the grains. The equilibrium between these spin-up and spin-down mechanisms determines the maximum angular velocity that a grain can achieve due to RATs (e.g., [96]) :

$$\begin{aligned}\frac{\omega_{\rm RAT}}{\omega_{\rm T}} &\simeq 48.7\hat{\rho}a_{-5}^{3.2}\mathcal{U}\left(\frac{\gamma}{0.1}\right)\left(\frac{30\,{\rm cm}^{-3}}{n_{\rm H}}\right)\left(\frac{\bar{\lambda}}{1.2\ \mu{\rm m}}\right)\\ &\quad\times\left(\frac{100\ {\rm K}}{T_{\rm gas}}\right)(1+F_{\rm IR})\end{aligned} \tag{1.36}$$

where a is the grain size, $a_{-5} = a/(10^{-5}\,{\rm cm})$, ρ is grain mass density, $\hat{\rho} = \rho/(3\,{\rm g\,cm}^{-3})$, and $\bar{\lambda} = 1.2\ \mu$m is a mean wavelength of the ISRF [95].

$F_{\rm IR}$ is a dimensionless coefficient of rotational damping by IR emission and is calculated as:

$$F_{\rm IR} \simeq 0.91\left(\frac{\mathcal{U}^{2/3}}{a_{-5}}\right)\left(\frac{30\,{\rm cm}^{-3}}{n_{\rm H}}\right)\left(\frac{100\ {\rm K}}{T_{\rm gas}}\right)^{1/2}. \tag{1.37}$$

The minimum size for grain alignment, aka alignment size, $a_{\rm align}$, is defined by the grain size at which $\omega/\omega_T = 3$ [56].

1.3.4.2. *Magnetically Enhanced Radiative Torque Alignment (MRAT)*

Dust grains that contain embedded iron atoms are naturally paramagnetic. When these iron atoms are concentrated in clusters within the grains, the grains can become superparamagnetic (e.g., [90]). The combined effect of enhanced magnetic relaxation and radiative torques can drive grains to achieve perfect alignment with the magnetic field. This mechanism is known as Magnetically Enhanced Radiative Torque Alignment (MRAT) [85].

Following [85], the dimensionless relaxation parameter

$$\delta_{\rm mag} \equiv \frac{\tau_{\rm gas}}{\tau_{\rm mag}}$$

quantifies how rapidly magnetic dissipation acts relative to gas damping, where $\tau_{\rm gas}$ is the gas damping timescale due to collisions, and $\tau_{\rm mag}$ is characteristic time of the magnetic relaxation.

For grains with embedded iron clusters, which are plausible for grains in dense regions due to grain evolution, one has

$$\delta_{\rm mag,sp} = \frac{\tau_{\rm gas}}{\tau_{\rm mag,sp}} = 56 a_{-5}^{-1} \frac{N_{cl}\phi_{\rm sp,-2}\hat{p}^2 B_3^2}{\hat{\rho} n_4 T_{\rm gas,1}^{1/2}} \frac{k_{\rm sp}(\Omega)}{T_{\rm d,1}}, \tag{1.38}$$

where $B_3 = B_{\rm tot}/(10^3\ \mu{\rm G})$, $a_{-5} = a/(10^{-5}\ {\rm cm})$, $n_4 = n_{\rm H}/(10^4\ {\rm cm}^{-3})$ with $T_{\rm gas,1} = T_{\rm gas}/(10\,{\rm K})$, $T_{\rm d,1} = T_{\rm d}/(10\,{\rm K})$, $n_{\rm H} \approx 2n({\rm H}_2)$ for molecular gas. The parameter $\hat{p} = p/5.5$ normalizes the coefficient $p \approx 5.5$, which describes the magnetic moment of an iron atom. $N_{\rm cl}$ denotes the number of iron atoms per cluster, and $\phi_{\rm sp}$ is the volume filling factor of iron clusters, with $\phi_{\rm sp,-2} = \phi_{\rm sp}/0.01$, and $k_{\rm sp}(\Omega)$ is a function of the grain rotation frequency Ω, of order unity (see [90] for details).

Magnetic relaxation becomes effective when $\delta_{\rm mag,sp} > 1$, meaning that magnetic dissipation acts faster than collisional damping. However, paramagnetic relaxation alone ($\delta_{\rm mag} \ll 1$) is generally too weak to account for the observed alignment degrees in dense regions [85]. Numerical calculations by [85] show that the combined effects of suprathermal rotation driven by RATs and magnetic relaxation can significantly enhance the alignment degree, allowing superparamagnetic grains to reach nearly perfect alignment when $\delta_{\rm mag,sp} > 10$.

1.3.4.3. *Radiative Torque Disruption (RAT-D)*

Radiative Torque Disruption (RAT-D) was proposed by [97]. The RAT-D mechanism is that radiative torques can spin up dust grains to rotational speeds high enough for them to break apart due to centrifugal forces in an intense radiation field. When the centrifugal stress induced by grain rotation exceeds the grain's tensile strength, large grains will be disrupted into smaller ones. This process plays a crucial role in shaping the grain size distribution in astrophysical environments.

Consider a spinning dust grain with an angular velocity ω. The tensile stress experienced by the grain is calculated as $S = \rho\omega^2 a^{2/4}$ where ρ is the mass density of the grain. The maximum tensile strength of the grain is $S_{\rm max}$ for large grains, based on the material. RAT can spin the grain up until the centrifugal stress exceeds $S_{\rm max}$ in the strong radiation field. When this threshold is surpassed, the grain undergoes rotational disruption, fragmenting into smaller pieces [97]. The critical angular velocity for the disruption is given by:

$$\omega_{\rm crit} = \frac{2}{a}\left(\frac{S_{\rm max}}{\rho}\right) \simeq \frac{3.6\times10^8}{a_{-5}} S_{\rm max,7}^{1/2}\hat{\rho}^{-1/2}, \tag{1.39}$$

with, $S_{\rm max,7} = S_{\rm max}/(10^7\,{\rm erg\,cm^{-3}})$.

The critical size $a_{\rm disr}$ which grains are disrupted following this equation:

$$\left(\frac{a_{\rm disr}}{0.1\ \mu{\rm m}}\right)^{2.7} \simeq 5.1\gamma_{0.1}^{-1}\mathcal{U}^{-1/3}\bar{\lambda}_{0.5}^{1.7}S_{\rm max,7}^{1/2}, \tag{1.40}$$

with, $\bar{\lambda}_{0.5} = \bar{\lambda}/(0.5\ \mu{\rm m})$, and strong fields of $U \gg 1$ [97].

The maximum size for which RAT-D still disrupts grains is given by [97]:

$$a_{\rm disr,max} \simeq 1.7\gamma\bar{\lambda}_{0.5}\left(\frac{\mathcal{U}}{\bar{n}\bar{T}_{\rm gas}^{1/2}}\right)^{1/2}\left(\frac{1}{1+F_{\rm IR}}\right), \tag{1.41}$$

where $\bar{n} = n_{\rm H}/(30\,{\rm cm^{-3}})$ and $\bar{T} = T_{\rm gas}/(100\ {\rm K})$.

Under the RAT-D mechanism, dust grains with sizes in the range $a_{\rm disr}$ to $a_{\rm disr,max}$ are fragmented into smaller grains with $a < a_{\rm disr}$, leading to a modification of the initial grain size distribution.

1.3.4.4. Implications of Radiative Torque Paradigm

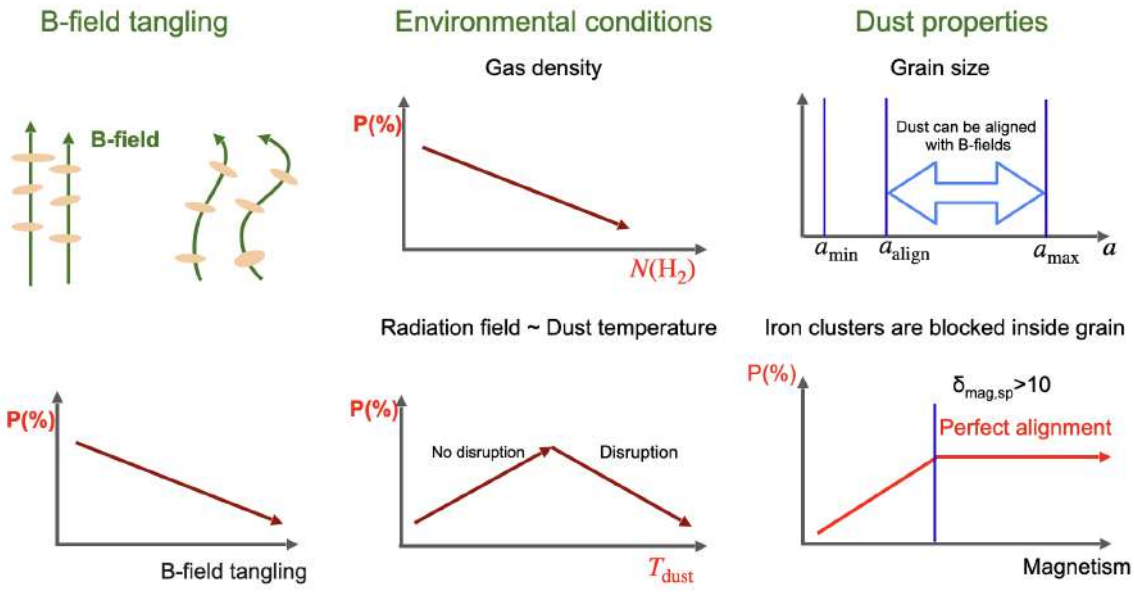

Figure 1.17: Summary of key factors affecting the dust polarization degree.

Multiple physical mechanisms can influence the polarization degree, P, including magnetic field geometry, local environment, and the properties of the dust grains.

Figure 1.17 summarizes the key factors affecting P under the RAT paradigm. Tangled magnetic fields along the line of sight can cause partial cancellation of polarization vectors, thereby lowering the observed polarization degree. As shown in the left panel of Figure 1.17,

increasing B-field disorder leads to a decrease in P. In the middle panels, we see how the environment affects alignment. In dense molecular regions, high gas column densities $N(H_2)$ reduce the penetration of radiation and increase collisional damping, both of which reduce P. Additionally, dust temperature T_d, which correlates with radiation strength, has a non-monotonic effect. Low T_d implies weak RATs and low alignment, while high T_d can lead to grain disruption via the RAT-D mechanism, thus decreasing P in the warmest regions. Hence, the polarization fraction increases with increasing dust temperature, then it decreases when the RAT-D effect happens. Grain alignment requires dust grains to exceed a minimum size threshold, a_{align}, to be aligned by RATs. The top right panel shows that grains in the range $a_{align} < a < a_{max}$ can align with the magnetic field. Additionally, embedded magnetic inclusions such as iron clusters can greatly enhance the alignment efficiency through the MRAT mechanism. When $\delta_{mag,sp} > 10$, grains can achieve nearly perfect alignment.

Observationally, the RAT theory has been crucial in interpreting polarization data from various astronomical environments. It explains the linear polarization observed in starlight due to aligned dust grains, thus allowing astronomers to infer properties of both dust grains and magnetic fields. Observations in infrared and sub-millimeter wavelengths, such as those from *Planck*, ALMA, and SOFIA, extensively rely on RAT theory to interpret polarized thermal emission, which is key to mapping magnetic field morphology in star-forming regions, molecular clouds, and protoplanetary disks [98, 50]. Consequently, RAT theory serves as a vital tool for constraining grain size distributions, compositions, and shape parameters directly from observational polarization signatures [99].

Numerical modeling of thermal dust polarization by [100, 101], using a `DustPOL-py` code based on the RAT-A and RAT-D mechanisms, demonstrated that the depletion of large grains by RAT-D leads to a decrease in polarization fraction at long wavelengths when the dust temperature is sufficiently high. This successfully reproduces the anticorrelation observed in observational data. RAT theory has been integrated into simulations. The first is the POLArized RadIation Simulator (`POLARIS`) code [102]. Recent studies by [91, 103] using the updated version of `POLARIS` highlighted the significant impact of grain magnetic properties and grain size variations on simulated dust polarization. Their findings emphasize that accurately modeling polarization requires careful consideration of magnetically enhanced RAT alignment mechanisms and grain size evolution.

1.4. Motivation and Outline of Thesis

The formation of stars is one of the most fundamental processes. The general outline of how stars are born, from the gravitational collapse of dense regions in molecular clouds, existing models cannot fully explain the observed low efficiency of star formation [35]. However, the exact role of magnetic fields in star formation is one of the unanswered questions [e.g., 37]. Magnetic fields have been attracting increasing attention over the past decades, especially with advances in observational polarimetry and theoretical modeling [e.g., 44, 104].

Dust grains, although only a minor component of the ISM by mass (1%), provide critical insights into the dynamics of star-forming regions [e.g., 2]. Their ability to align with magnetic fields and emit polarized radiation allows us to trace the morphology and strength of magnetic fields in various environments. Moreover, the dust alignment, disruption, evolution, and properties, which depend on local conditions, have not been carefully studied.

Recent observational surveys with high-sensitivity polarimeters on ground- and space-based telescopes and modeling tools have opened new windows for testing theories of dust grain alignment and magnetic fields in star formation.

This PhD thesis aims to study the role and characteristics of magnetic fields and dust physics in star formation. Specifically, I aim to: (1) investigate the role of magnetic fields in star formation by measuring the structure and strength of magnetic fields in molecular clouds and filaments, and (2) test the Radiative Torque Alignment (RAT-A) and Radiative Torque Disruption (RAT-D) using polarization observations and numerical modeling.

I focus on combining polarimetric data from two powerful instruments, JCMT/POL-2 and SOFIA/HAWC+, to study thermal dust polarization in five interesting star-forming regions: Auriga (LkHα 101), M17, G11.11–0.12, Musca, and OMC-1. The diversity of these regions allows us to probe environments with different densities, temperatures, and radiation fields.

This thesis is organized as follows:

Chapter 2: Far-IR and submillimeter Polarization Observations presents the observational data and instrumentation used in this study. It introduces the target star-forming regions of this thesis, Auriga (LkHα 101), M17, G11.11–0.12, Musca, and OMC-1.

Chapter 3: Magnetic Fields focuses on the analysis of magnetic fields using polarization data, presents results of magnetic fields, including morphology and strength, and a discussion of the role of magnetic fields in star formation.

Chapter 4: Observational Constraints on Grain Alignment and Evolution investigates dust physics and grain alignment mechanisms through observational studies of Auriga, M17, and G11.11–0.12. I examine the variation of polarization fraction with total intensity, dust temperature, and column density, and assess the roles of RAT-A and RAT-D effects. I also evaluate the importance of magnetic field tangling and magnetic relaxation, and present evidence for grain growth in dense environments.

Chapter 5: Numerical Modeling of Thermal Dust Polarization presents numerical modeling of thermal dust polarization based on the RAT paradigm using the `DustPOL-py` code. I apply modeling to Musca and OMC-1 to test the RAT-A and RAT-D effects in these regions.

Chapter 6: Conclusions and Future Work summarizes the main findings of the thesis, discusses their implications for dust physics and the role of magnetic fields in star formation, and outlines potential studies for future work.

Chapter 2

Far-IR and submillimeter Polarization Observations

In this chapter, I present the observational data used throughout this dissertation, focusing on polarization measurements in different star-forming regions. The data were obtained from several facilities, mainly from the James Clerk Maxwell Telescope (JCMT) and the Stratospheric Observatory for Infrared Astronomy (SOFIA). I describe the selected targets, Auriga, M17, G11.11–0.12, Musca, and OMC-1, highlighting their astrophysical significance and the specific datasets associated with each. I also introduce the key polarimetric instruments and observatories that provided the data. This chapter also outlines the data reduction and selection criteria applied to ensure the quality of the polarization measurements. The observations are the basis on which the analysis in the following chapter is presented.

2.1. Polarimetric Instrumentations

In the last decade, significant advancements have been made in polarimetric instrumentation, particularly at FIR and submillimeter wavelengths. As introduced in Chapter 1, polarized light can be detected due to dust grain alignment mechanisms, primarily via the RAT mechanism, which aligns dust grains with the local magnetic field.

One of the most important milestones in this field was the launch of the *Planck* satellite, which mapped polarized thermal dust emission across the entire sky at a frequency of 353 GHz [105]. Ground-based facilities have also seen major improvements. For example, the POL-2 polarimeter [106] mounted on the JCMT telescope represents a major advance in submillimeter polarimetry. It plays a central role in the BISTRO survey, which focuses on magnetic fields in star-forming regions [58]. Another key facility is HAWC+ (High-resolution Airborne Wideband Camera Plus), a FIR imaging polarimeter onboard SOFIA [107]. SOFIA, a unique airborne platform, enabled cutting-edge FIR observations above most of the atmospheric water vapor. Although its final science flight was on September 29, 2022, the large archive of SOFIA/HAWC+ data remains invaluable for ongoing studies. Balloon-borne instruments such as BLASTPol and PILOT have also contributed significantly to our understanding of polarized dust emission. However, with no space-based FIR polarimeters planned until at least 2030, the focus has shifted to ground-based efforts. Instruments NIKA-2 on the IRAM 30-meter telescope and A-MKID on the APEX telescope are in the late stages of commissioning at (sub)millimeter wavelengths. The ALMA and NOEMA have also developed polarimetric capabilities for interferometric studies.

Table 2.2 summarizes key polarimetric instruments that operate in the (sub)millimeter

Instrument	Platform	Wavelength	FWHM	Start date	Status
Stokes	Airborne	100	35	1990	Finished
HERTZ	Ground	353	20	1995	Finished
SCUPOL	Ground	850	14	1997	Finished
SPARO	Ground	450	30	2000	Finished
BLASTPol	Balloon	250, 350, 500	150	2010	Finished
SHARP/SHARC	Ground	350, 450	9	2005	Finished
Planck	Space	850	300	2009	Finished
HAWC+	Airborne	53–214	4.8–18.2	2016	Finished
PILOT	Balloon	214	120	2015	Finished
POL-2	Ground	450, 850	10, 14	2016	Active
NIKA-2	Ground	1150, 2000	11, 18	2019	Commissioning
A-MKID	Ground	350, 850	19	2019	Commissioning

Table 2.1: Dust polarimetric instruments operating at infrared and submillimeter wavelengths. This table is modified from [44].

and infrared regimes. Only mapping-capable instruments are included; those restricted to single-point measurements are excluded. The table highlights that POL-2 remains a leading instrument in submillimeter polarimetry, while SOFIA/HAWC+ was a key facility in the FIR domain. Therefore, in this PhD thesis, I use mostly data from JCMT and SOFIA, which are presented below.

2.1.1. JCMT/POL-2

The JCMT is a 15-m diameter submillimeter telescope located near the summit of Maunakea. It is the largest single-dish facility operating at wavelengths between 0.4 and 1.4 mm. Since 2015, JCMT operations have been managed by East Asian countries (China, Taiwan, South Korea, and Japan), in collaboration with partners from the UK and Canada. Vietnam has been participating as an observer country since 2017, which allows Vietnamese researchers to propose observations and access JCMT data.

The POL-2 instrument is a linear polarimetry module designed to work with the Submillimetre Common User Bolometer Array-2 (SCUBA-2) bolometer camera [108, 109]. SCUBA-2 contains an array of approximately 10,000 pixels. POL-2 is not a detector itself; its operation requires SCUBA-2. SCUBA-2 and POL-2 perform simultaneous observations at 450 μm and 850 μm. The optical setup covers the full SCUBA-2 field of view. The beam sizes at 850 and 450 μm are 14.1″and 9.6″, respectively.

The POL-2 system includes three key optical components: a calibration wire-grid polarizer, a rotating half-wave plate (HWP), and an analyzer polarizer. The HWP is a birefringent optical element that modulates the incoming polarization signal by rotating the polarization angle of light by twice its rotation angle. By continuously rotating the HWP, POL-2 modulates the signal on timescales faster than atmospheric or instrumental drifts, allowing for accurate recovery of the Stokes parameters.

JCMT/POL-2 polarimetric observations are typically performed using the “CV Daisy” (CV = constant velocity) scan pattern. This mode is optimized for compact and moderately extended sources, providing uniform, high-sensitivity coverage over the central 3 arcmin radius region. The telescope traces a continuous, petal-shaped path around the target, ensuring repeated sampling and high signal-to-noise (S/N) near the map center. The outer region, ex-

tending to a 6′radius, is also covered with lower sensitivity. Dedicated software, such as the `Starlink SMURF/POL-2` pipeline [110], is used to reduce and debias the resulting polarimetric data.

2.1.2. SOFIA/HAWC+

HAWC+ [107] was a FIR imaging polarimeter and photometer designed to measure the linear polarization of thermal dust emission in five broadband filters centered at 53, 63, 89, 154, and 214 μm. These wavelengths are particularly sensitive to warm dust grains (T $\sim$ 30 – 100 K), commonly found in high-mass star-forming regions, HII regions, and galactic centers. The instrument's spatial resolution ranged from approximately 5″at 53 μm to 18″at 214 μm. The field of view varied with wavelength but typically ranged between 2′and 10′. HAWC+ uses three 31 $\times$ 40 pixel arrays: two for the reflective component and one for the transmitted component of linear polarization.

To perform polarimetric measurements, HAWC+ used a HWP with the Chop-Nop technique for observation. This technique rapidly switches between the target and a nearby reference position on the sky, assumed to be free of polarized emission, by moving the secondary mirror. This method for single-dish infrared observations effectively removes background polarization from the sky and telescope. However, the technique requires a significant amount of time and can be limited by the assumption that the reference fields contain no intrinsic polarization.

2.2. Targets

In this study, I use polarization data from several observational facilities, targeting different star-forming regions. The relevant information of their corresponding polarization data is summarized in Table 2.2. These regions were selected to represent different environments and evolutionary stages in the star formation process.

Table 2.2: Properties of targets' polarization observations.

Objects	Distance pc	Facility	Wavelength μm	Beam size	Representative for
Auriga	466	JCMT	850	14.″6	Low-mass star formation
M17	1980	SOFIA	154	13.″6	Photodissociation region
G11	3600	SOFIA	214	18.″2	IRDC
Musca	170	*Planck*	850	5′	Simple filament
OMC-1	388	SOFIA	214	18.″2	High-mass star formation

These regions span a broad range of distances, sizes, and physical conditions. Auriga and Musca represent relatively nearby and low-mass star-forming environments, while G11 and M17 are more distant, high-mass regions. OMC-1, located in the Orion Molecular Cloud complex, provides a key example of nearby massive star formation. The diversity of these targets enables a comprehensive study of magnetic fields and dust physics, as well as their connection to star formation across different environments.

2.2.1. Auriga

The first target is LkHα 101, located in the densest part of the Auriga-California Molecular Cloud (AMC). This region surrounds the early B-type star, LkHα 101, using new data taken

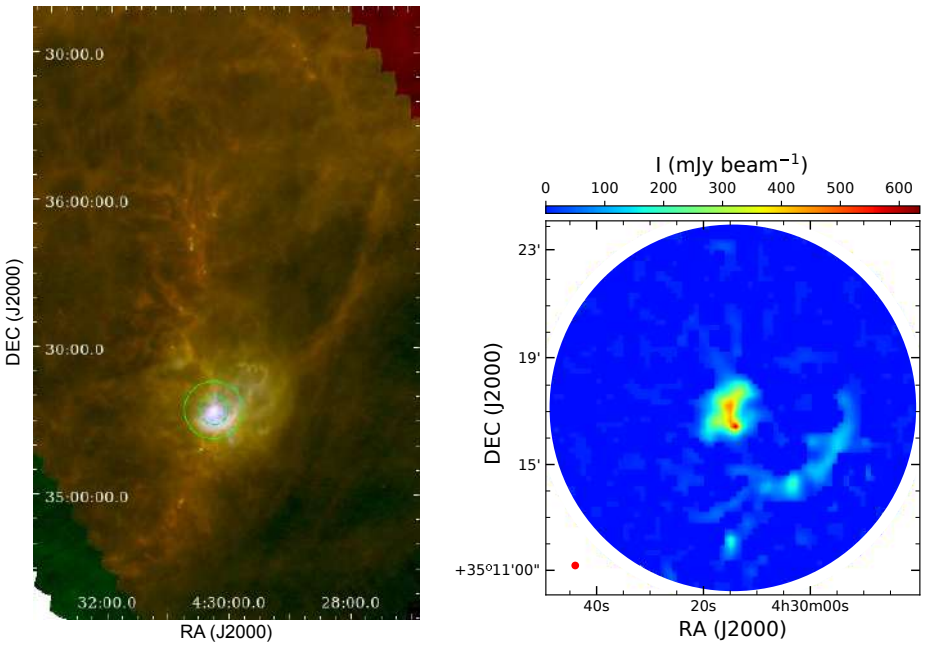

Figure 2.1: Left: Observed field of LkHα 101 by JCMT/POL-2 at 850 μm wavelength (green circle) overlaid on an RGB composite image from *Herschel* (R=250 μm, G=160 μm, B=70 μm) [111]. The outer green circle outlines the 6′ field of view of POL-2, while the inner circle marks the central 3′ area with the best sensitivity. Right: 850 μm intensity map. The red circle in the lower left corner denotes the JCMT beam size, which is 14″.

by POL-2. The observed field corresponds to the region labeled LkHα 101-S (S stands for South) of [112].

The Auriga-California cloud is a component of the Gould Belt and has an estimated total mass of about 10^5 $M_\odot$. It is located at $\sim$ 466 $\pm$ 23 pc from Earth [113] and extends ~80 pc. Based on SCUBA-2 observations at 450 and 850 μm, 59 candidate protostars were identified in the cloud, 35 of which are located in the LkHα 101 region [112]. Auriga provides an ideal testbed for studying magnetic fields in a low-density environment with low star formation efficiency. Although being similar in size, mass, and distance, Auriga forms far fewer stars, 20 times fewer, than OMC, which contains around 50 OB stars, while Auriga hosts only one early B-type star, LkHα 101, a member of the cluster in NGC 1579 [114]. Additionally, observations by [53] revealed that both Auriga-California and Orion-A share similar large-scale line-of-sight magnetic field morphologies. Parallax measurements of the H_2O maser in the L1482 filament indicate a distance of 532±28 pc [115], while Gaia DR2 estimates LkHα 101's distance to be 567±68 pc [116]. Understanding the magnetic field in Auriga-California is particularly valuable for exploring the factors that regulate star formation efficiency in molecular clouds. The left panel of Figure 2.1 displays the location of the POL-2 field.

2.2.2. M17

M17 is a well-known high-mass star-forming region [117, 118] located within the Omega Nebula, also commonly known as the Swan or Horseshoe Nebula, in the Sagittarius constellation. M17 is considered a valuable reference region for studying high-mass star formation, particularly regarding the effects of strong stellar feedback from OB-type stars. It provides insights into the characteristics of magnetic fields within energetic environments such as bright

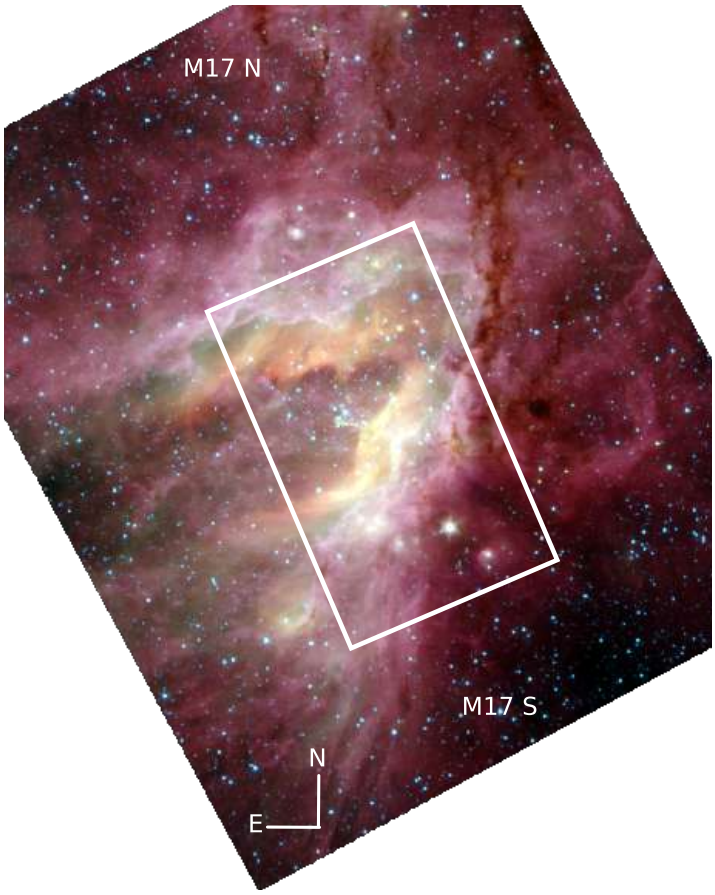

Figure 2.2: An RGB image toward M17 observed by *Spitzer* (R = 8 μm, G = 4.5 μm, and B = 3.6 μm). The white box indicates the area observed by SOFIA/HAWC+, which is analyzed in the present study.

photodissociation regions and massive stellar clusters. M17 is at a distance of ∼1.98 pc [119]. The distance to the central regions of star-forming activity in M17 was measured through trigonometric parallaxes of methanol masers using observations from the Very Long Baseline Array [119]

Figure 2.2 shows a three-color composite image created using mid-infrared data from *Spitzer*[1]. As the nearest giant H II region to Earth, M17 provides an excellent environment to study magnetic field structures, dust grain properties, and the impact of stellar feedback driven by a nearby massive cluster, the photodissociation region, and infrared-bright sources such as UC 1, IRS 5, CEN 92, Anon 1, and Anon 3 [118]. The studied region is shown in Figure 2.2.

2.2.3. G11.11 -0.12

The filament G11.11−0.12 (hereafter G11, also commonly known as the Snake filament) represents an early-stage massive filament, offering an excellent opportunity to investigate the initial conditions of high-mass star formation. Its evolutionary state provides an important comparison to more evolved regions like M17 and OMC-1. Currently, there are only a handful of studies on magnetic fields within massive filaments, including G35.39 −0.33 [120], G34.43 +0.24 [121, 122], G14.225 −0.506 [123], NGC 6334 [124], and G47.06 +0.26 [125].

[1] https://www.spitzer.caltech.edu

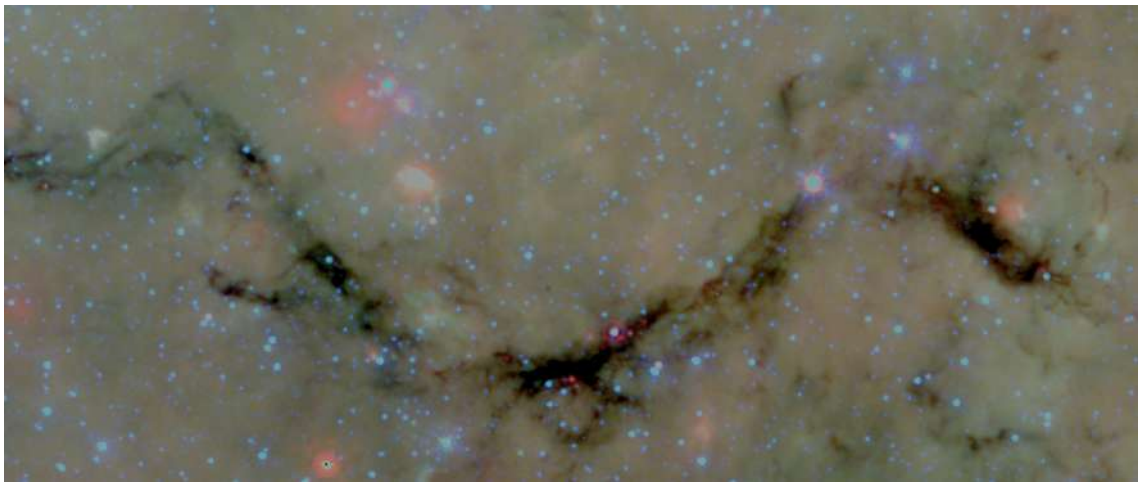

Figure 2.3: A RGB image of G11 observed by *Spitzer* (R = 24 μm, G = 8 μm, and B = 5.8 μm).

G11 is an infrared-dark cloud (IRDC) filament located within the Galactic plane on the near side of the Scutum-Centaurus arm [126]. It represents a high-mass star-forming region that is currently cold, dense, and in a very early evolutionary stage [127]. G11 is located at a distance of approximately 3.6 kpc from Earth [128]. G11 extends about 22 pc in length and approximately 1.0 pc in width, 22 pc long, and has a mass of 1.5×10^4 $M_\odot$ [17]. The filament's linear mass density is about 600 $M_\odot$/ pc, already fragmented [129]. Along its spine, G11 hosts seven dense clumps identified by JCMT/SCUBA [130], and 18 protostellar cores [131]. Among these clumps, two massive ones (P1 and P6 shown in Figure 3.14), each with masses around $1000 M_\odot$ and sizes less than 1 pc, are sites for the formation of high-mass stars [126]. Given these characteristics, G11 provides an exceptional environment to investigate initial physical conditions and the role of magnetic fields during the early phases of IRDC formation and, more generally, in high-mass star formation. Moreover, G11 offers an ideal laboratory to test the RAT theory, as the region lacks bright embedded sources, making the interstellar radiation field the main radiation source controlling dust grain alignment. Furthermore, observations of dust polarization within this dense filament can allow us to constrain grain growth [132, 96].

In this study, I analyze polarization data from SOFIA/HAWC+ observations taken at a wavelength of 214 μm. These data represent the first measurement of polarized thermal dust emission across the entire G11 region. An RGB composite image of G11 is presented in Figure 2.3. Previously, magnetic fields in the central part of G11 were investigated using JCMT/SCUPOL polarimetric data at 850 μm with a spatial resolution of 20″ ($\sim$ 0.35 pc) [133]. Their results showed that magnetic fields in this region are predominantly oriented perpendicular to the filament's spine, with an estimated lower limit of the plane-of-sky magnetic field strength of $\sim$200 μG.

2.2.4. Musca

Musca, which appears as the dark region in Figure 2.4, is situated at a distance of 170 pc [134] and represents an early-stage filament lacking active star formation [135]. Only one T Tauri star candidate has been identified near its northern edge [136]. Musca is recognized as an isothermal filament in hydrostatic equilibrium and has already undergone fragmentation, suggesting potential future star formation activity [137, 138]. Previous polarization measure-

Figure 2.4: Optical image of Musca, adopted from iceinspace.com.au.

ments of starlight [139] and thermal dust emission [140, 135] revealed that local magnetic fields are predominantly perpendicular to the filament spine. *Herschel* data revealed that magnetic fields trace low-column-density striations, suggesting that Musca may be accreting interstellar material along these structures [135]. Recently, observations by SOFIA/HAWC+ at higher spatial resolution toward a part of Musca also confirmed the magnetic fields perpendicular to the filament spine [141].

In this study, I use polarization maps obtained by *Planck* at ~850 μm (353 GHz), the highest frequency and most sensitive dust polarization from *Planck* [140]. The Stokes parameters I, Q, and U were mapped at a resolution of $5'$, equivalent to a physical scale of approximately 0.24 pc. The pixel size of these maps is $112''$. Musca stands out as one of the regions with notably high S/N measurements within the *Planck* full-sky polarization data [140].

2.2.5. OMC-1

The Orion Nebula, located at a distance of approximately 388 ± 5 pc from Earth [142], is the closest region of high-mass star formation [143]. Figure 2.5 displays the RGB map of OMC-1. The Orion Molecular Cloud 1 (OMC-1), also known as Orion A, lies behind an H II region ionized by massive O-B stars in the Trapezium cluster. OMC-1 comprises two major clumps: the northern Becklin-Neugebauer/Kleinmann-Low (BN/KL) clump [144, 145] and the southern Orion S clump [146]. The BN/KL region hosts a particularly energetic molecular outflow characterized by a wide opening angle and several ejected components. Previous studies have shown that the magnetic fields within OMC-1 have an hourglass-shaped morphology with estimated strengths on the order of mG (e.g., [147, 148, 149]).

In this thesis, I analyze thermal dust polarization data from observations of the Orion BN/KL region from SOFIA/HAWC+ at a wavelength of 214 μm and a beam size of $18\farcs2$. These data were first published with an emphasis on magnetic field structures [148, 149]. A depolarization hole was subsequently identified [148]. Additional evidence for the RAT-D

Figure 2.5: OMC-1 is taken by James Webb Space Telescope/NIRcam, adopted from https://science.nasa.gov/mission/webb/multimedia/images/.

mechanism in this region was later reported in the BN/KL clump [150] and in the Orion Bar [151].

2.3. Data Selection

This section reviews the criteria used to select reliable polarization data from the POL-2 and HAWC+ observations toward Auriga (LkHα 101), M17, and G11. Careful data selection is essential to ensure the quality of polarization measurements. In this section, I focus on the data quality selection on the Auriga, G11, and M17 regions. These datasets are being analyzed for the first time in these studies; therefore, they require a thorough evaluation of data reliability and consistency. The details of this process are described in the following subsections for each target. Typically, selection is based on S/N thresholds in Stokes I and derived quantities such as polarization intensity or polarization fraction. Among the regions, Auriga has relatively faint emission and lower S/N ratios. As a result, special attention is given to defining selection criteria that can effectively retain high-confidence polarization vectors.

Besides, the polarization data for Musca and OMC-1 have already been presented and analyzed in previous works [140, 148]. Therefore, I adopt the previously established selection criteria for the two filaments.

2.3.1. Auriga

In this work, I analyze polarized thermal emission from the LkHα 101 region at 850 μm, obtained as part of the BISTRO (B-fields in Star-forming Region Observations) survey. The left panel of Figure 2.1 displays the location of the POL-2 field, while the right panel shows the corresponding 850 μm intensity map, I-map.

The data from Auriga was collected over nine days between 2017 and 2019, comprising 21 visits with a total integration time of approximately 14 hours. he final two observations were carried out on January 8$^{\text{th}}$, 2019. The data were read and reduced using Starlink [152].

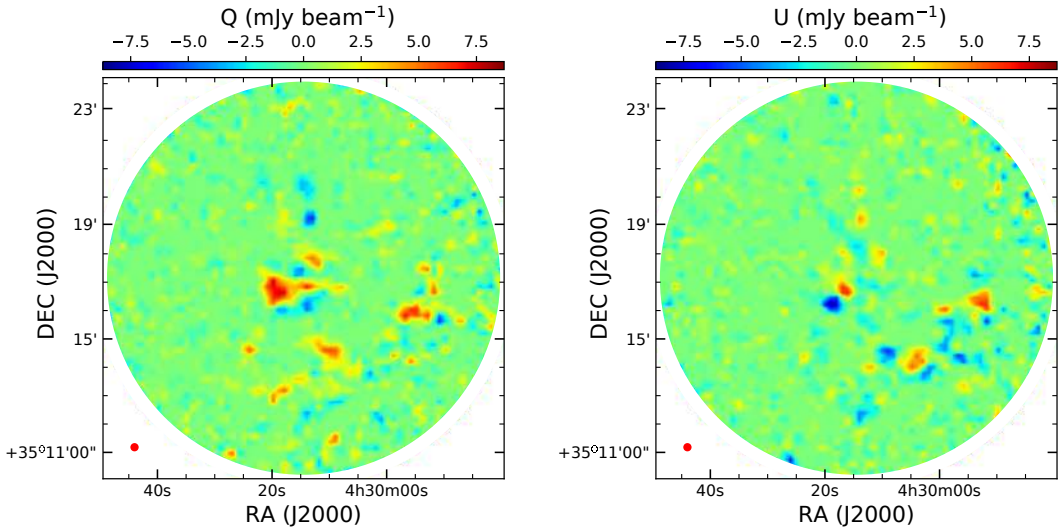

Figure 2.6: Q (left) and U (right) maps; the red circles at the lower left corners indicate the JCMT beam size at 850 μm of 14″.

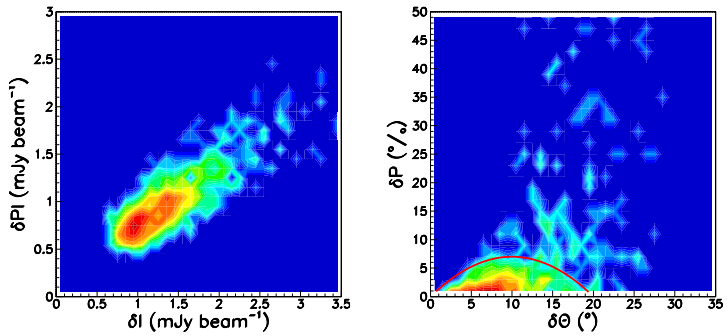

Figure 2.7: Correlations of measurement uncertainties, where color indicates the number of data points on a logarithmic scale: δPI versus δI (left) and δP versus $\delta\theta$ (right). A strong correlation is observed for δPI versus δI (left panel). Pixels with well-defined polarization fractions ($\delta P \lesssim 7\%$) and polarization angles ($\delta\theta \lesssim 20°$) are enclosed by the red parabola in the right panel.

In this work, I use the gridded maps with a pixel size of $12'' \times 12''$, which is comparable to the telescope beam size. The Stokes I, Q, and U time-streams were processed with `pol2map`, a POL-2-specific version of the iterative map-making algorithm `makemap` [108]. For each pixel, the data provide the total intensity I, the Stokes parameters Q and U, and their corresponding uncertainties, δI, δQ, and δU

Figure 2.6 presents the maps of the measured Stokes Q (left) and U (right). To identify measurements suitable for further analysis, correlations among the parameter uncertainties are shown in Figure 2.7, without any cuts applied. The left panel clearly indicates a strong correlation between δI and δPI. The parabola described by $\delta P = -0.07\delta\theta^2 + 1.4\delta\theta$ illustrates the relation between δP and $\delta\theta$, which are inherently connected quantities. In the following analysis, only data satisfying $\delta P < -0.07\delta\theta^2 + 1.4\delta\theta$ (hereafter the δP–$\delta\theta$ cut) are used. Because the 850 μm polarized emission from the LkHα 101 region is particularly weak, likely the weakest among all regions surveyed by BISTRO, the best compromise between retain-

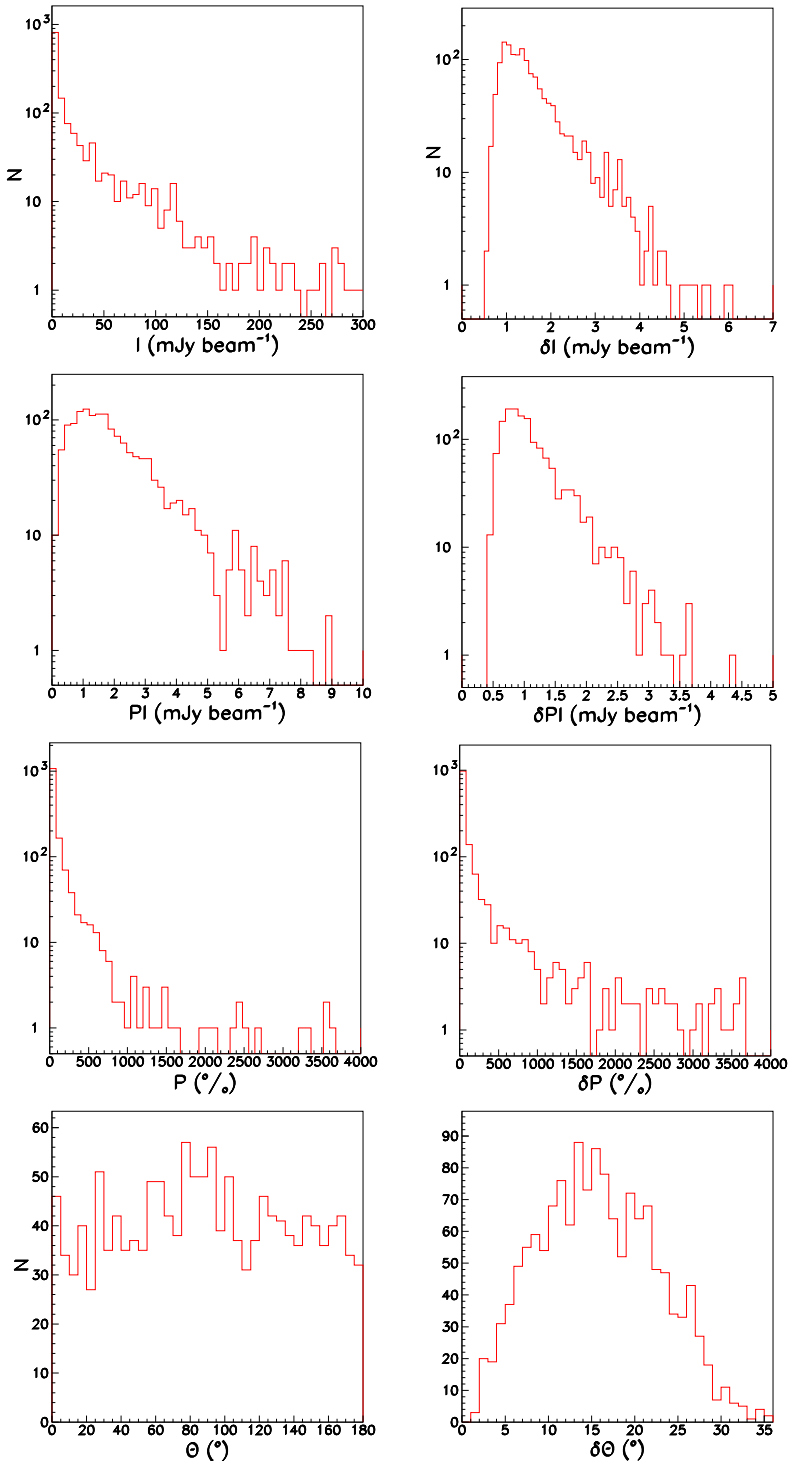

Figure 2.8: From left to right, top to bottom: distributions of I, δI, PI, δPI, P, δP, θ, and $\delta\theta$.

ing high-quality data and ensuring sufficient statistics was achieved by adopting this δP–$\delta\theta$ cut, which maintains the robustness of the results and conclusions. These S/Ns indicate the measurement quality of the corresponding quantities I, PI, and P. The dimensionless mean and RMS values are (12.1, 19.8), (2.1, 1.9), and (1.7, 2.0) for $I/\delta I$, $PI/\delta PI$, and $P/\delta P$, respectively. After applying the δP-$\delta\theta$ cut, these values increase to (38.5, 22.7), (4.0, 2.4), and (3.9, 2.4), showing that this cut removes the low-S/N part of the distributions. Following this

selection, 419 line segments remain in the map. Since this map is directly derived from the observations, it is used for further analysis and discussion in the following sections.

Figure 2.8 shows the distributions of I, PI, P, δI, δPI, δP, θ, and $\delta\theta$ for the raw data set, with no cuts applied. Values of P exceeding 100% arise from noise in PI and I (i.e., random noise spikes can yield $PI > I$). In total, 1466 pixels satisfy $I > 0$, $PI > 0$, and $P > 0$, out of the $90 \times 90 = 8100$ pixels in the entire map.

2.3.2. M17

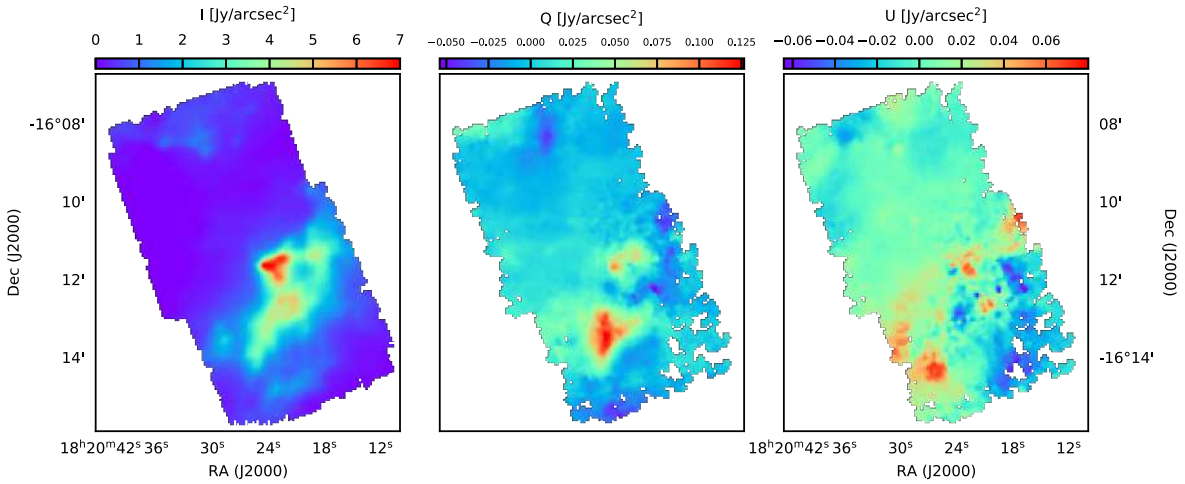

Figure 2.9: From left to right: Stokes I, Q, and U maps of M17 from SOFIA/HAWC+ at 153 μm-wavelength.

Polarimetric observations of thermal dust emission toward M17 were obtained from SOFIA, having a beam size of 13.6″ and an original pixel size of 6.9″ [107]. Figure 2.9 presents the resulting Stokes I, Q, and U maps from left to right, respectively. One-dimensional histograms illustrating the distributions of the raw data for I, σ_I, PI, σ_{PI}, P, σ_P, θ, and σ_θ. are shown in Figure 2.10.

For this analysis, data are initially selected based on two S/N criteria: S/N(I) > 250 and S/N(P) > 3. This combined threshold is hereafter referred to as the 'master cut'. Additionally, applying this master cut automatically satisfies the third SOFIA quality recommendation of excluding pixels with unphysically high polarization fractions ($P > 50\%$) [66]. After implementing the master cut, 5139 pixels remain, representing ~23% of the original 138×162 pixel map. This approach effectively removes low-level emissions, thereby significantly enhancing data quality. All the following analyses presented in the subsequent chapters are carried out using this master cut.

2.3.3. G11.11 -0.12

In this work, I use archival far-infrared polarimetric observations of G11 taken with SOFIA/HAWC+ at 214 μm, obtained within the FIELDMAPS legacy program (PI: Ian W. Stephens, Worcester State University). These data have an angular resolution of 18.″2, which corresponds to a spatial scale of about 0.32 pc at a distance of ~3.6 kpc. The G11 region was covered by combining four HAWC+ fields observed on July 13, 2018, with a total integration time of 2316 s. The observations were performed using the chop-nod imaging technique [107]. The Level 4 data products were downloaded from the SOFIA archive[2] and reduced with the HAWC DRP

[2]https://irsa.ipac.caltech.edu/Missions/sofia.html

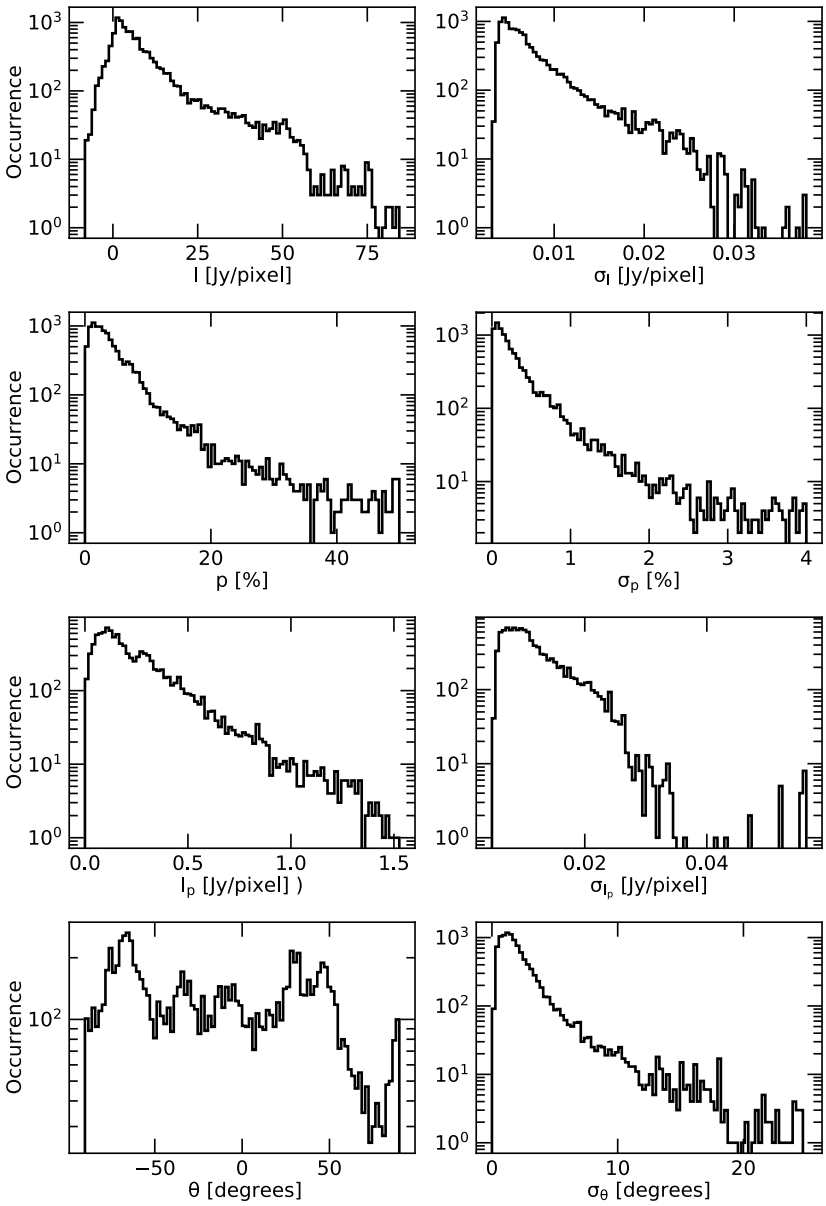

Figure 2.10: Distributions of of I, σ_I, PI, σ_{PI}, P, σ_P, θ, and σ_θ derived from the original SOFIA/HAWC+ dataset, arranged from left to right and top to bottom, respectively.

pipeline v1.3.0, which performs standard steps including chop-nod subtraction, flat-fielding, flux calibration, background removal, polarization angle correction, and mosaic construction.

Figure 2.11 presents the Stokes I, Q, and U maps of G11 (left to right panels). Figure 2.12 shows one-dimensional histograms of the raw data for I, σ_I, PI, σ_{PI}, P, σ_P, θ, and σ_θ. The mean S/N values of the original I, Q, and U data are 28.3, 0.2, and 0.5, respectively. Because of the low S/N ratios, the original $4''.55$ pixels were binned to $9''.1$ to improve the statistics, yielding a pixel size about half of the SOFIA/HAWC+ beam at 214μm. After binning, the mean S/Ns increase by a factor of two: 57.4 for I, 0.4 for Q, and 1.0 for U, respectively. For further analyses, I only use the data satisfying: S/N$(I) > 10$, S/N$(P) > 3$, S/N$(\theta) > 3$, and $P < 30\%$.

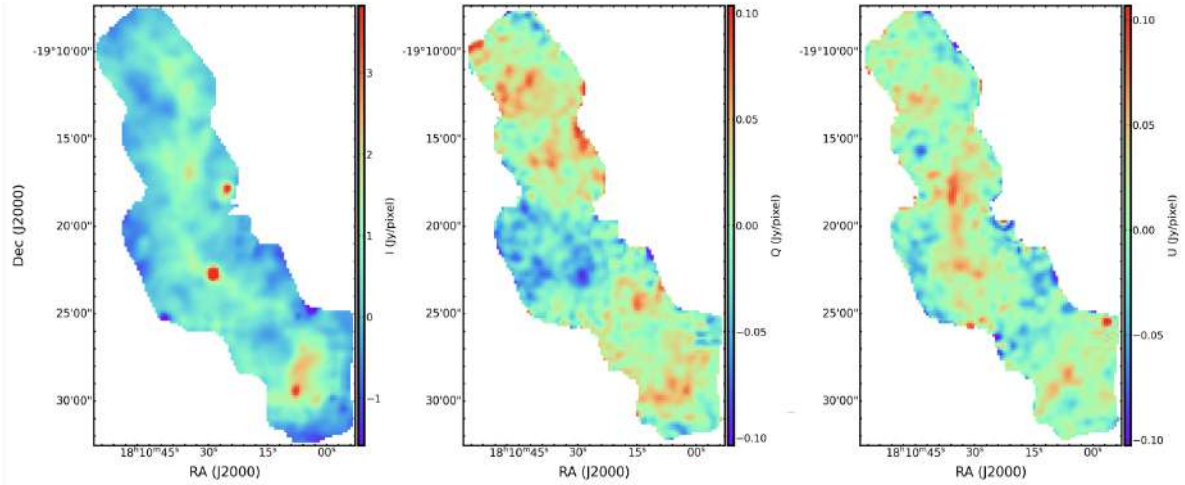

Figure 2.11: From left to right: SOFIA/HAWC+ 214 μm Stokes I, Q, and U maps of G11.11 -0.12.

2.3.4. Auxiliary Data

Column density and dust temperature maps

To understand the physical environment, I investigate the dust temperature and column density of each target. These maps were derived from archival data, obtained by fitting a modified blackbody function to the SED (see 1.17). Most of the data are based on *Herschel* data with some modifications, and Musca from *Planck* for consistency with the polarization data.

LkHα 101: The dust column density of the Auriga-California molecular cloud has been constructed by [111] using four *Herschel* wavebands at 160, 250, 350, and 500 μm.

M17: The column density, $N(\mathrm{H_2})$, has been derived using modified blackbody fit to *Herschel* Space Observatory data and JCMT/SCUBA-2 850 μm. The data is taken from [118].

G11: The dust column density map of the Auriga-California molecular cloud was derived by [111] using four *Herschel* wavebands at 160, 250, 350, and 500 μm.

Musca: The *Planck* Collaboration used *Planck* data at 850, 550, and 350 μm, together with IRAS data at 100 μm, and fitted them with a modified blackbody function to produce all-sky maps of dust temperature, optical depth, and spectral index [77]. The resulting maps have an angular resolution of 5′. The dust temperature and column density maps of Musca shown in Figure 5.1 (center and right panels) are extracted from these *Planck* all-sky products.

OMC-1: The dust temperature and column density maps for OMC-1 are adopted from [148]. They were produced from SED fitting using multi-wavelength emission data covering 53 μm to 35 mm. The dataset includes SOFIA observations at 53, 89, 154, and 214 μm, *Herschel* observations at 70, 100, 160, and 250 μm, and JCMT observations at 850 μm. To correct for free-free emission associated with UV radiation in the region, the longest-wavelength data from combined Green Bank Telescope and Very Large Array observations at 3.5 and 35 mm were also included. The resulting dust temperature and column density maps have a resolution of 18.″2.

2.3.5. Polarization Angle Dispersion Function

To measure the small-scale tangling of the magnetic field, I calculate the polarization angle dispersion function, $\mathcal{S}$ (see Section 3.3 of [67]). For each pixel located at $\boldsymbol{x}$, the value of

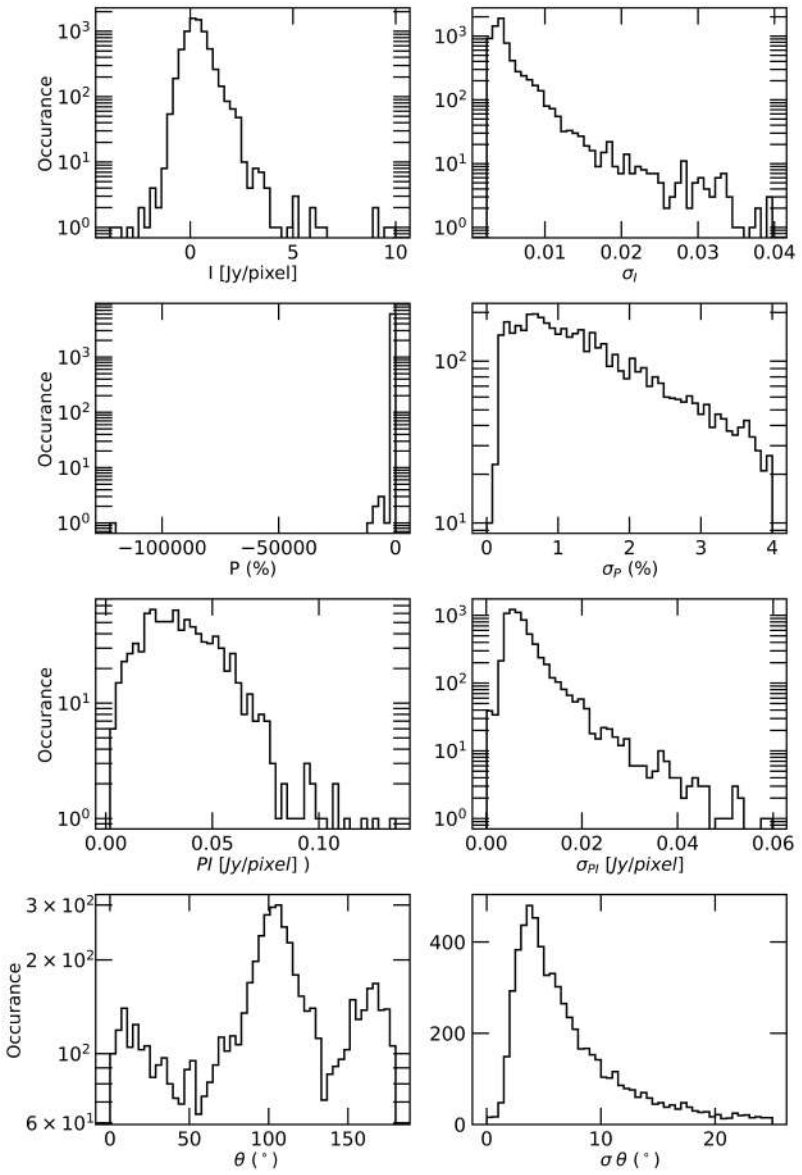

Figure 2.12: From left to right, top to bottom: Distributions of of I, σ_I, PI, σ_{PI}, P, σ_P, θ, and σ_θ for the SOFIA/HAWC+ data of G11.11 -0.12.

$\mathcal{S}(\boldsymbol{x}, \delta)$ is defined as the root mean square of the polarization angle differences between the reference pixel at $\boldsymbol{x}$ and the surrounding pixels. In particular, the angle difference is written as $\mathcal{S}_{xi} = \theta(\boldsymbol{x}) - \theta(\boldsymbol{x} + \delta)$, where pixel i lies on a circle centered at $\boldsymbol{x}$ with radius δ:

$$\mathcal{S}^2(\boldsymbol{x}, \delta) = \frac{1}{N} \sum_{i=1}^{N} \mathcal{S}_{xi}^2, \tag{2.1}$$

where N is the number of pixels located on the circle. In this study, I compute $\mathcal{S}(\boldsymbol{x}, \delta)$ by setting δ equal to one beam size of the observations. Because of the noise in the Stokes parameters Q and U, $\mathcal{S}$ is affected by bias. The uncertainty of the angle dispersion function, $\sigma_{\mathcal{S}}$, and the debiased value, $\mathcal{S}_{\rm db}$, for each pixel at position $\boldsymbol{x}$ are calculated as follows (see Section 3.5 of [67]):

$$\sigma_{\mathcal{S}}^2 = \frac{\delta\theta^2(\boldsymbol{x})}{N^2\mathcal{S}^2}\left(\sum_{i=1}^{N}\mathcal{S}_{xi}\right)^2 + \frac{1}{N^2\mathcal{S}^2}\sum_{i=1}^{N}(\mathcal{S}_{xi})^2\delta\theta^2(\boldsymbol{x}+\boldsymbol{\delta}), \tag{2.2}$$

and

$$\mathcal{S}_{\rm db}^2 = \mathcal{S}^2 - \sigma_{\mathcal{S}}^2. \tag{2.3}$$

Here, $\mathcal{S}_{\rm db}$ may be either positive or negative, depending on whether the true value is larger or smaller than the random polarization angle of 52° [153, 154]. Data points with $\mathcal{S} \leq \sigma_{\mathcal{S}}$ are excluded from the analysis. In the following, I use $\mathcal{S}$ to denote $\mathcal{S}_{\rm db}$ for simplicity.

Chapter 3

Magnetic Fields in Star-Forming Regions

In this Chapter, I present a detailed analysis of magnetic fields in three star-forming regions: LkHα 101, M17, and G11.11 -0.12. I apply two methods to estimate magnetic field strength: one for calculating the mean magnetic field strength in LkHα 101 and M17, and an updated approach to create a magnetic field strength map for G11. To investigate the role of magnetic fields in star formation, I examine the relative importance of magnetic fields with other key physical factors, including gravity and turbulence. The results provide insights into how magnetic fields influence the formation and evolution of stars within molecular clouds.

3.1. Introduction

Magnetic fields are believed to play a crucial role in the formation and evolution of interstellar clouds and protostars, alongside other key factors such as self-gravity, turbulence, and stellar feedback. Understanding the precise role of magnetic fields in molecular cloud evolution and star formation remains a major challenge in modern astrophysics.

Over the past few decades, growing evidence has highlighted the importance of magnetic fields in the dynamics of molecular clouds and the star formation process [1]. Two contrasting models describe the influence of magnetic fields. In the strong-field model, magnetic pressure resists gravitational collapse. This magnetic support is lost until the ratio of core mass to magnetic flux exceeds a critical value, leading to gravitational collapse and the formation of a new star [38]. In the weak-field model, magnetic fields are relatively weak, allowing turbulence to dominate cloud dynamics and drive star formation through the formation of filaments at the intersections of supersonic turbulent flows [e.g., 37]. Dust grains tend to align with their major axes perpendicular to the local magnetic field direction, which allows the magnetic field morphology (see [55, 155] for reviews). Polarimetric observations at FIR and sub-millimeter wavelengths have been widely used to investigate the morphology and strength of magnetic fields (see [44] for a review). To test these theoretical models, it is essential to directly observe and analyze magnetic fields in specific molecular clouds. In this study, I focus on three molecular clouds —Auriga, M17, and G11 —to investigate how magnetic fields influence star formation.

3.2. Methods for Calculating Magnetic Field Strength

3.2.1. Davis-Chandrasekhar-Fermi (DCF) Method

The strength of the plane-of-sky component of the magnetic field, $B_{\rm POS}$, can be estimated using the DCF method [156, 23]. This method assumes that, in a magnetized medium where the magnetic field is effectively frozen into the gas, the dispersion in magnetic field arises

from turbulent motions within the cloud. When the perturbations are small, turbulent gas motions perturb the field lines and excite small-amplitude Alfvénic fluctuations superposed on a large-scale, ordered magnetic field B_0. In this regime, the kinetic energy density of the turbulent motions is assumed to be comparable to the magnetic energy density in the fluctuating component of the magnetic field,

$$\frac{1}{2}\rho\,\sigma_V^2 = \frac{(\delta B)^2}{8\pi},$$

where ρ is the gas mass density and σ_V is the one-dimensional non-thermal velocity dispersion, δB is the fluctuating component of the magnetic field. From this relation we obtain

$$\delta B \approx \sqrt{4\pi\rho}\sigma_V.$$

The polarization angles trace the orientation of the plane-of-sky component of the magnetic field. Assuming that the fluctuation angles are small (small-angle approximation), the dispersion of polarization angles, σ_θ (in radians), is approximately proportional to the relative magnetic perturbation,

$$\sigma_\theta \simeq \frac{\delta B}{B_0}.$$

Since the dispersion in position angles, σ_θ, is for plane-of-sky (POS) observations we can only calculate the plane-of-sky magnetic field strength, $B_{\rm POS}$, which is then given by

$$B_{\rm POS} \approx Q\sqrt{4\pi\rho}\frac{\sigma_V}{\sigma_\theta}.$$

where Q is a correction factor for line-of-sight and beam-integration effects. $\rho = \mu m_H n(\mathrm{H_2})$, is measured in g cm^{-3} $\mu = 2.8$ is the mean molecular weight, σ_V in km s^{-1}, σ_θ is the dispersion of the polarization angles about a mean magnetic field in degrees. Q is a dimensionless correction factor that accounts for the fact that real molecular clouds are more complex than the idealized DCF assumptions. In particular, line-of-sight averaging, beam smoothing, and curvature of the large-scale field reduce the observed angular dispersion compared to the true three-dimensional perturbations, causing the uncorrected DCF formula to overestimate the magnetic-field strength. Magnetohydrodynamic simulations indicate that Q typically lies in the range $Q \sim 0.4$–0.7, with a commonly used value being $Q = 0.5$ [e.g., 59].

[37] proposed a variant of the method, the plane-of-sky magnetic field strength can be calculated as:

$$B_{\rm POS} \approx 9.3\sqrt{n(\mathrm{H_2})}\frac{\Delta V}{\sigma_\theta} \quad (\mu\mathrm{G}), \tag{3.1}$$

where $n(\mathrm{H_2})$ is the number density of hydrogen molecules in cm^{-3}; ΔV is the FWHM of the non-thermal velocity component in units of km s^{-1}. For the DCF method to be applicable, the polarization angle dispersion should remain below approximately $\sim 25°$ [59].

The uncertainties of $B_{\rm POS}$ are computed using using the following relation:

$$\frac{\delta B_{\rm POS}}{B_{\rm POS}} = \sqrt{\left(\frac{1}{2}\frac{\delta n(\mathrm{H_2})}{n(\mathrm{H_2})}\right)^2 + \left(\frac{\delta\Delta V}{\Delta V}\right)^2 + \left(\frac{\delta\sigma_\theta}{\sigma_\theta}\right)^2}, \tag{3.2}$$

where $\delta n(\mathrm{H_2})$, $\delta\Delta V$, and $\delta\sigma_\theta$ are the uncertainties in the number density, velocity dispersion, and polarization angle dispersion, respectively.

3.2.2. Structure Function and Unsharp Masking Methods

A key challenge in applying the DCF method is accurately separating the turbulent component of the polarization angle dispersion from large-scale variations in the magnetic field. If the large-scale variation is not removed correctly, the calculated polarization angle dispersion, σ_θ, may be unrealistically large, leading to an overestimate of the magnetic field strength. Several methods have been proposed to account for the effects of ordered magnetic field variation [see, e.g. 44].

In this thesis, I will use the structure function and the unsharp masking methods to calculate the polarization angle dispersion.

Polarization Angle Dispersion: Structure Function

The structure-function technique was originally introduced by [157, 158] as a method for estimating the polarization angle dispersion, σ_θ, in the plane of the sky. It is defined as follows.

We analyze pairs of pixels at locations $\boldsymbol{x}$ and $\boldsymbol{x}+\boldsymbol{l}$. For a specified pixel separation l, the structure-function is expressed as the mean square angle between the polarization half-vectors of the pair:

$$\langle \Delta\theta^2(l) \rangle = \frac{1}{N(l)} \sum_{i=1}^{N(l)} [\theta(\boldsymbol{x}) - \theta(\boldsymbol{x}+\boldsymbol{l})]^2, \tag{3.3}$$

where $N(l)$ denotes the number of such pairs. We assume that the magnetic field $\boldsymbol{B}$ can be approximated by the sum of a large-scale ordered field of mean amplitude B_0, and a turbulent component, δB. Additionally, it is assumed that the correlation length of the turbulent component is significantly smaller than the distance over which $\boldsymbol{B}$ varies significantly. For small separations l, this can be written as:

$$\langle \Delta\theta^2(l) \rangle = b^2 + m^2 l^2 + \sigma_M^2(l), \tag{3.4}$$

where b represents the root mean square contribution from the turbulent component, and m quantifies the effect of the gradient of $\boldsymbol{B}$. Furthermore, the contribution from measurement uncertainties, $\sigma_M(l)$, is accounted for. The polynomial given in equation 3.4, when fitted to the measured structure-function, provides values of b and m. For $b \ll 1$, $\sigma_\theta \simeq b/\sqrt{2}$ (where b is measured in radians).

The ratio of the turbulent field, δB, to the large-scale underlying field (i.e., the mean field), B_0, was defined [158].

$$\frac{\delta B}{B_0} = \frac{b}{\sqrt{2-b^2}}, \tag{3.5}$$

We note that Equations 3.4 and 3.5 hold only if the correlation length of the turbulent component satisfies $\delta < l$ [158].

We apply the strcture-fuction method for Lkhα 101 and M17. The detailed analysis for Lkhα 101 is presented in Section 3.3.1.2, and the corresponding analysis for M17 is provided in Section 3.4.1.1.

Polarization Angle Dispersion: Unsharp Masking Method

The unsharp masking method, originally introduced by [147], removes large-scale variations by subtracting a smoothed version of the polarization angle map from the original data.

We start from the measured polarization angle map, $\theta_{\rm obs}$), and create a smoothed map $\langle\theta\rangle$, which represents the large-scale (ordered) magnetic field on the plane of the sky.

To obtain $\langle\theta\rangle$, we apply a boxcar (or a moving-average filter) filter to the angle map. For each pixel, we take a square box centered on that pixel and compute the average of all angles inside the box:

$$\langle\theta\rangle = \frac{1}{N_{\rm box}} \sum_{i=1}^{N_{\rm box}} \theta_{\rm obs},$$

where $N_{\rm box}$ is the number of pixels in the box. The box size is chosen so that the smoothing length is smaller than the radius of curvature of the magnetic field; for example, a 3×3 pixel box was adopted in [147]. In practice, this is done by iterating over all pixels in the map and computing the smoothed angle within a pixel box centered on the considered pixel.

Then, the residual unsharp-masked angle at each pixel is computed by subtracting the smoothed angle from the original angle:

$$\Delta\theta = \theta_{\rm obs} - \langle\theta\rangle.$$

The standard deviation of the residual angle map, $\Delta\theta$, reflects the turbulent component of the field and provides the angular dispersion for the region.

We apply the unsharp masking method for Lkhα 101. The detailed analysis for LkHα 101 is presented in Section 3.3.1.1. The updated unsharp masking approach for constructing a two-dimensional magnetic-field map, following [159], is described in Section 3.5.1.1 for G11.

3.2.3. Mass-to-Flux Ratio and Alfvénic Mach Number

Several key parameters are used to assess the relative importance of magnetic fields in the ISM, including the mass-to-flux ratio and the Alfvénic Mach number. The equations used to calculate both the mass-to-flux ratio and the Alfvénic Mach number are restated below.

Mass-to-flux Ratio

Physically, the mass-to-flux ratio compares the amount of mass per unit magnetic flux in the cloud to the critical value required for gravity to overcome magnetic support [e.g., 37]. The mass-to-flux ratio is given by the following formula:

$$\lambda = \frac{(M/\Phi)_{\rm observed}}{(M/\Phi)_{\rm critical}},$$

where M is the cloud mass and Φ is the magnetic flux.

The mass of cloud can be calculated by $M = \mu\, m_{\rm H}\, N({\rm H}_2) A$ in an area A. The magnetic flux through an area A is $\Phi = BA$, so the observed mass-to-flux ratio becomes

$$\left(\frac{M}{\Phi}\right)_{\rm observed} = \frac{\mu\, m_{\rm H}\, N({\rm H}_2) A}{BA} = \frac{\mu\, m_{\rm H}\, N({\rm H}_2)}{B}. \tag{3.6}$$

This expression is then normalized by the theoretical critical mass-to-flux ratio for a uniformly magnetized, self-gravitating sheet, $(M/\Phi)_{\rm critical} = 1/(2\pi\sqrt{G})$ [38], where G is the gravitational constant. The dimensionless mass-to-flux ratio is defined as

$$\lambda = \frac{(M/\Phi)_{\rm observed}}{(M/\Phi)_{\rm critical}} = 2\pi\sqrt{G}\,\frac{\mu\, m_{\rm H}\, N({\rm H}_2)}{B}. \tag{3.7}$$

By substituting the physical constants in cgs units, and expressing the magnetic field strength in μG and the column density in cm^{-2}, the above relation can be written in the convenient numerical form [e.g., 54]

$$\lambda = 7.6 \times 10^{-21} \frac{N(\mathrm{H_2})}{B_{\mathrm{POS}}}, \tag{3.8}$$

where $N(\mathrm{H_2})$ is in cm^{-2} and B_{POS} is the plane-of-sky magnetic-field strength in μG.

A region is considered magnetically subcritical if $\lambda < 1$, magnetic fields are strong enough to resist gravitational collapse. If $\lambda > 1$, the region is supercritical, gravity overcomes magnetic support, allowing collapse and potential star formation.

Alfvénic Mach Number

The interaction between magnetic fields and turbulence in the ISM can be quantified using the Alfvénic Mach number. The Alfvén Mach number, $\mathcal{M}_A$, is defined as:

$$\mathcal{M}_A = \frac{\sigma_{\mathrm{V}}}{v_A} \tag{3.9}$$

Here, $v_A = B_{\mathrm{tot}}/\sqrt{4\pi\rho} = Q \times \sigma_{\mathrm{V}}/\sigma_\theta$ is the Alfvénic velocity; both σ_{V} and v_A are calculated in km s^{-1}. Substituting v_A into Equation 3.9, I obtain a simplified relation, $\mathcal{M}_A = \sigma_\theta/Q$. In this study, I adopt $Q = 0.5$, as commonly used in the literature. When σ_θ is expressed in degrees [160], this relation becomes:

$$\mathcal{M}_A \approx 3.5 \times 10^{-2} \sigma_\theta, \tag{3.10}$$

where σ_θ is measured in degrees. A sub-Alfvénic value ($\mathcal{M}_A < 1$) means the cloud has a strong magnetic field, while a super-Alfvénic value ($\mathcal{M}_A > 1$) implies a weak magnetic field compared to turbulence.

3.3. Magnetic Fields in Auriga

Figure 3.1 shows the magnetic field orientation map of the LkHα 101 region, maintaining only pixels after the cut. The calculation of magnetic field strength is presented in Section 3.3.1. The results are presented in Section 3.3.2.

The central region is defined as the area within $R < 120''$ from the map center. The dust lane is identified by an elliptical area centered at RA $\sim$ 4h30m4.7s and DEC $\sim +35°14'47.8''$, with major and minor axes of $300'' \times 108''$ and a position angle of 135° (see the white contours in Figure 3.5). Hereafter, these two subregions are referred to as CR and DL, respectively.

3.3.1. Calculating Magnetic Field Strength

3.3.1.1. Application of Unsharp Masking in Auriga

Table 3.1: Dependence of angle dispersion and number of remaining half-vectors, N_{rm}, on δI-cuts.

	δI (mJy beam^{-1}) <	1.0	1.5	2.0	2.5	3.0
Central Region	$\sigma_\theta(°)/N_{\mathrm{rm}}$	16.0/94	17.1/135	17.5/141	17.6/142	17.3/144
Dust Lane	$\sigma_\theta(°)/N_{\mathrm{rm}}$	5.8/12	17.1/192	17.1/195	17.1/195	17.1/195

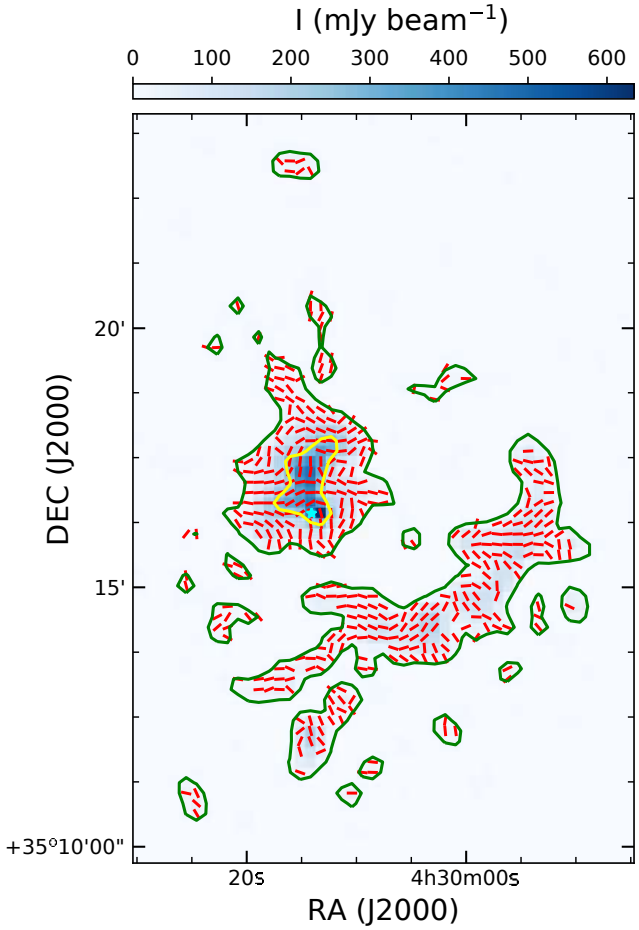

Figure 3.1: Magnetic field orientation (red line segments) overlaid on the 850 μm dust continuum intensity map. Green contours indicate emission at 15 mJy beam^{-1}, and the yellow contour marks the 250 mJy beam^{-1} level. Only polarization vectors that satisfy the δP–$\delta\theta$ selection criteria are shown. The B-type star LkHα 101 is indicated by a cyan star located at RA $= 4^{\rm h}30^{\rm m}14.4^{\rm s}$, DEC $= 35°16'24''$.

I employ the unsharp masking technique to compute the angle dispersion for both the CR and DL regions using a 3×3 pixel box. This process is shown in Figure 3.2: the original polarization angle (left panel), the smoothed polarization angle (center panel), and the residual polarization angle (right panel). The angle dispersion, determined by applying the condition $|\Delta\theta| < 90°$ (to avoid the effect of the $\pm 180°$ ambiguity of the magnetic field lines), results in $\sigma_\theta = 17.2° \pm 0.4°$ and $17.1° \pm 0.5°$ for the CR and the DL, respectively.

To examine how the measured dispersion is affected by observational uncertainties, Table 3.1 lists the polarization angle dispersion for different cuts in δI, in addition to the δP-$\delta\theta$ selection. As shown in Table 3.1, the angle dispersion changes very little when stricter S/N criteria are imposed on both the total intensity and the polarized intensity. This suggests that the δP-$\delta\theta$ cut provides a robust selection. A noticeable difference appears only for the most stringent case in the dust lane, where $\delta I < 1$ mJy beam^{-1}. In this case, the number of remaining half-vectors is reduced sharply from 195 to 12, and the angle dispersion decreases from $\sigma_\theta \sim 17°$ to 5.8°.

The uncertainties in the polarization angle dispersion are also examined using the same

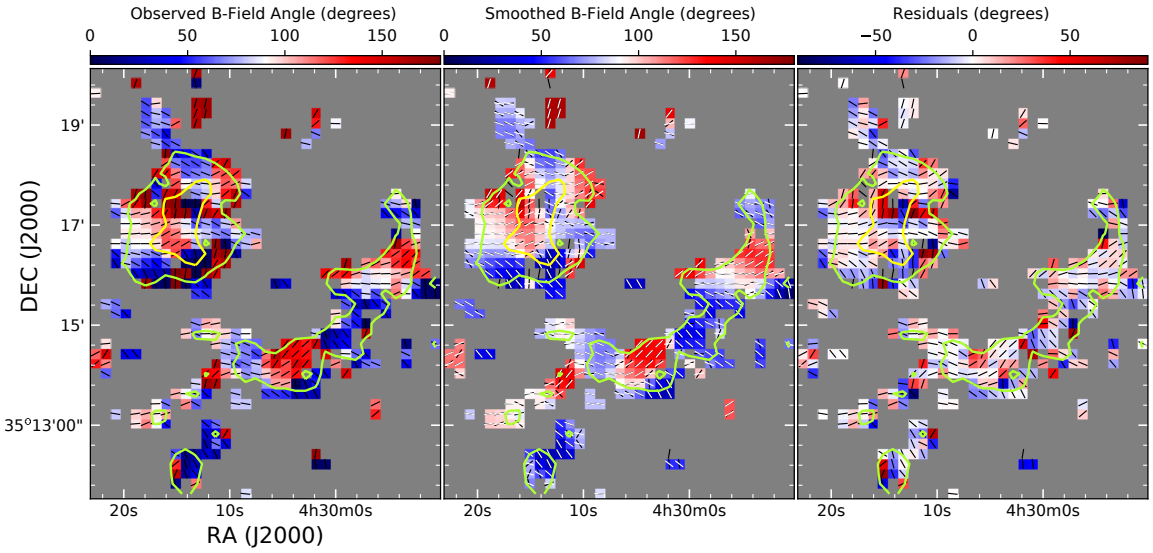

Figure 3.2: Magnetic field angle maps: original (left), smoothed (center), and residual (right). Green contours indicate emission at 50 mJy beam^{-1}, while the yellow contour corresponds to the 250 mJy beam^{-1} level. In all panels, the observed magnetic field half-vectors are shown in black. In the central panel, the smoothed half-vectors derived from the unsharp masking method are overlaid in white.

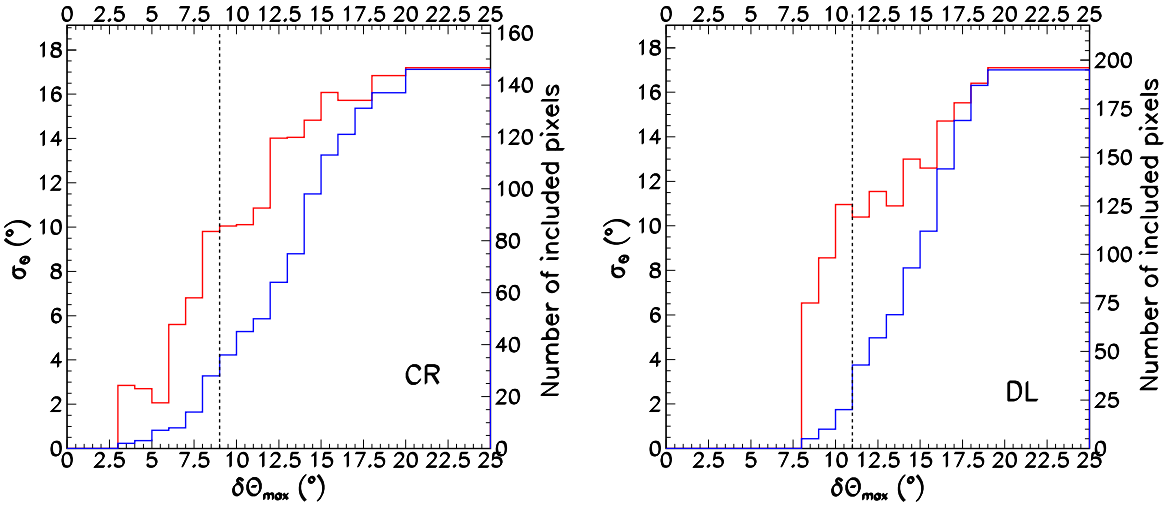

Figure 3.3: Dependence of polarization angle dispersion (red) and the number of included pixels (blue) on the maximum allowed uncertainty, $\delta\theta_{\max}$, for the central region (left) and dust lane (right). The black dashed lines indicate the minimum value of $\delta\theta_{\max}$ above which the average polarization angle dispersion is calculated.

method [147]. Figure 3.3 illustrates the relationship between angle dispersion and the maximum allowed uncertainty, $\delta\theta_{max}$, for each boxcar filter. This means that the angle dispersion of the map is calculated by requiring the condition that the maximum uncertainty of all pixels in each 3×3 boxcar filter be smaller than $\delta\theta_{max}$. The polarization angle dispersion is expected to rise with an increase in the maximum allowed uncertainty of the boxcar filters. Indeed, as shown in 3.3 (left for CR and right for DL), the angle dispersion increases as $\delta\theta_{max}$ increases. As was done by [161] and [162], from the angle dispersion for different $\delta\theta_{max}$ (see

Figure 3.3), I estimate the mean angle dispersion± uncertainties of $\sigma_\theta = 14.9° \pm 2.7°$ and $14.7° \pm 2.6°$ for CR and DL, respectively. These values are retained as the final polarization angle dispersion for further analysis. It is important to note that the results exclude the first few bins of $\delta\theta_{max}$, where the number of included pixels is fewer than 20, and are calculated with the application of the δP-$\delta\theta$ cut.

3.3.1.2. Application of Structure Function in Auriga

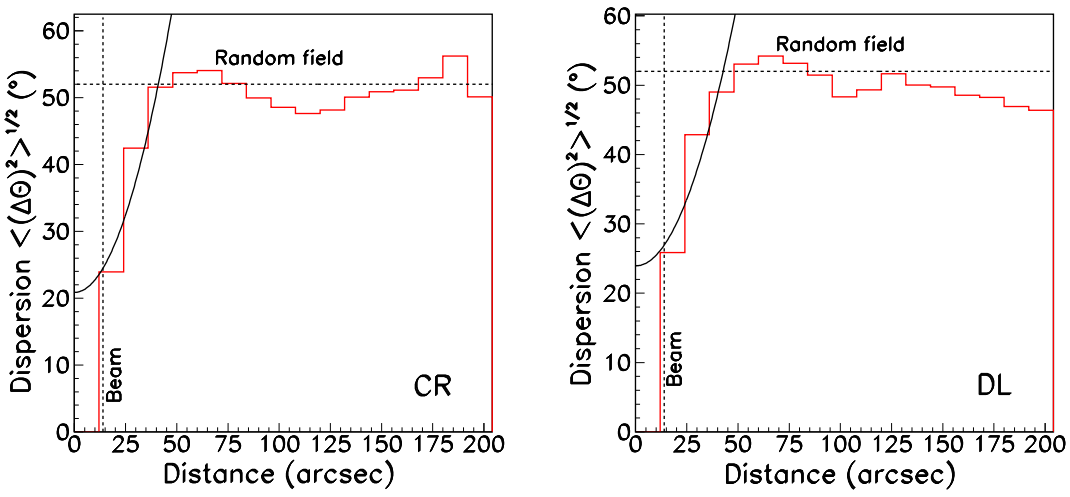

Figure 3.4: Structure functions calculated for the central region (left) and the dust lane (right). The horizontal dashed lines indicate the expected polarization angle dispersion for a random field (52°). The solid black curves show the best-fit results based on Equation (3.4), used to estimate the polarization angle dispersion. Vertical dashed lines mark the beam size of the JCMT telescope.

I calculate the structure functions method for both CR and DL; the result is shown in Figure 3.4. At distances > 50 arcsec, the structure functions approach the random field value of ~52° [154]. A fit to Equation 3.4 for short distances, $12'' < l < 36''$, gives $b = 20.9° \pm 6.8°$ and $23.9° \pm 7.1°$, which correspond to $\sigma_\theta = 14.8° \pm 4.8°$ and $16.9° \pm 5.0°$ for CR and DL, respectively. When additional cuts on δI, $\delta I < 1$ ($\delta I < 1.5$) mJy beam^{-1} I get values of $\sigma_\theta = 14.3° \pm 6.1°$ ($14.5° \pm 4.9°$) for CR. For DL, the 1 mJy beam^{-1} cut cannot be used because too few half-vectors are retained. However, with the 1.5 mJy beam^{-1} cut, I get $\sigma_\theta = 14.6° \pm 3.1°$.

The angle dispersion values remain consistent within one standard deviation when additional δI cuts are applied, compared to those obtained using only the δP-$\delta\theta$ criterion. This result supports the robustness of the δP-$\delta\theta$ cut.

3.3.1.3. Column and Number Densities

Using CO($J = 2 - 1$) and CO($J = 3 - 2$) observations from the KOSMA 3-m telescope, [163] investigated the structure of the L1482 molecular filament in the Auriga-California molecular cloud, which contains the region studied here. In their work, they identified 23 clumps along L1482 and derived their column and number densities. The CR region considered in this study, defined by a circle with a radius of 120″, contains their Clump 10, which

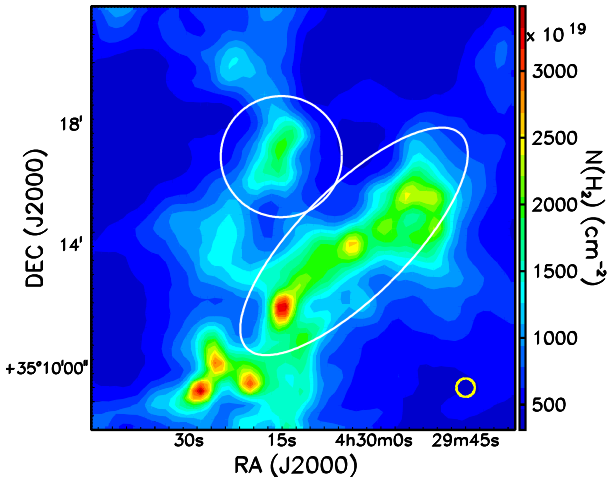

Figure 3.5: Locations of the central region (white circle) and the dust lane (white ellipse) overlaid on the *Herschel* column density map [111]. The *Herschel* beam size (36.6″) is indicated in the lower right corner of the figure.

was described as an ellipse with major and minor axes of 228″ × 110″. The DL region, with an extent of 600″ × 216″, overlaps with their Clump 12, whose size is 195″ × 68″, although the DL region used here is larger.

We use the column density map (Figure 3.5) from [111] to compute the average column densities and number densities. I find $N(\mathrm{H_2}) = (0.96 \pm 0.39) \times 10^{22}$ cm^{-2} and $n(\mathrm{H_2}) = 1.22 \times 10^4$ cm^{-3} for CR, and $N(\mathrm{H_2}) = (1.44 \pm 0.53) \times 10^{22}$ cm^{-2} and $n(\mathrm{H_2}) = 1.25 \times 10^4$ cm^{-3} for DL (summary in Table 3.2). The number densities are estimated following the same strategy used by [163]. The volume density $n(\mathrm{H_2})$ is given by

$$n(\mathrm{H_2}) = \frac{3M}{4\pi R^3 m_{\mathrm{H_2}}} = \frac{3\beta N_{\mathrm{total,H_2}} (D\Delta)^2}{4\pi R^3} \quad (\mathrm{cm^{-3}}), \tag{3.11}$$

where $\beta = 1.39$ is a correction factor that accounts for the contribution of helium in addition to $\mathrm{H_2}$ to the total mass, $N_{\mathrm{total,H_2}}$ is the total column density, $m_{\mathrm{H_2}}$ is the mass of a hydrogen molecule, and $\Delta = 14''$ is the pixel size of *Herschel* data. R is the effective radius of the clump under consideration, equal to $R = \sqrt{(ab)/2}$, and a and b are the major and minor axes of an ellipse covering the clump [163]. For consistency, as performed by [111], I adopt the same distance of $D = 450$ pc to the LkHα 101 region when calculating the column densities. We assume that the relative uncertainties in the number densities are identical to those of the column densities, with values of 42% for the CR region and 37% for the DL region.

3.3.1.4. Velocity Dispersion

The line-of-sight non-thermal velocity dispersion was derived from ^{13}CO(1–0) observations obtained with the Purple Mountain Observatory 13.7-m radio telescope [163]. For Clump 10, the measured value is $\sigma_V = 0.52$ km s^{-1}, which corresponds to $\Delta V = 1.22$ km s^{-1}. For Clump 12, the value is $\sigma_V = 0.64$ km s^{-1}, giving $\Delta V = 2.355\sigma_V = 1.52$ km s^{-1}.

We used archival CO(3–2) data from JCMT/HARP [164] to evaluate the velocity dispersion. Figure 3.6 (left) presents the velocity-integrated intensity map, while the right panel

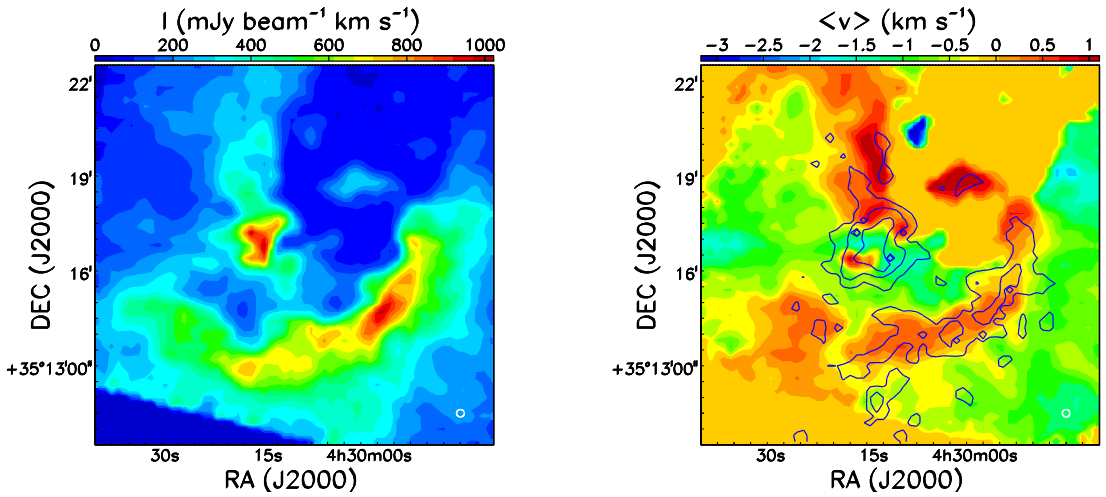

Figure 3.6: HARP CO(3–2) data. Left: Integrated intensity map over the velocity range ±5.5 km s^{-1}. Right: Intensity-weighted mean Doppler velocity map relative to the cloud's mean VLSR. Blue contours indicate 850 μm POL-2 polarized emission at 15, 100, and 250 mJy beam^{-1}. The HARP beam size (14″) is shown in the lower right corner of the figure.

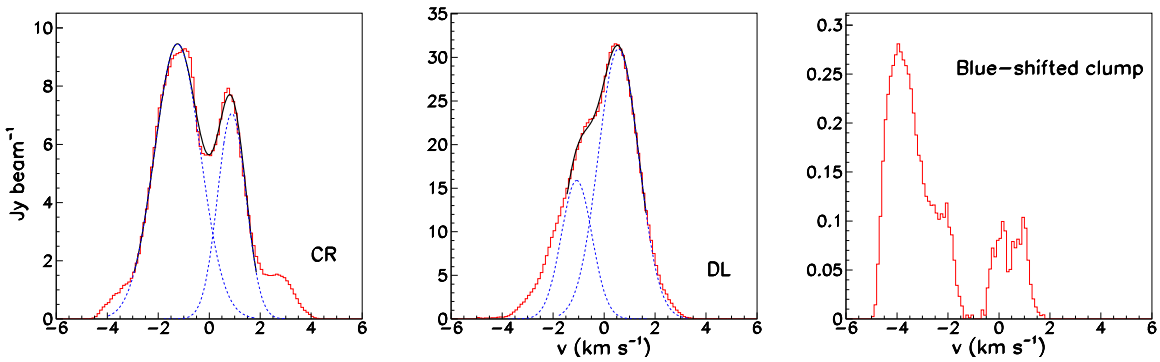

Figure 3.7: HARP CO(3–2) integrated spectra. Left: Central region. Center: Dust lane. Right: Blue-shifted clump located at RA ~ $4^h30^m07^s$, DEC ~ +35°13′20.5″. The blue dashed curves show the individual Gaussian components, while the black curves correspond to the combined two-Gaussian fits (see Section 3.3.1.4 for details).

shows the intensity-weighted mean Doppler velocity map obtained from the HARP observations. Notably, when I overlay the 850 μm dust emission contours observed with POL-2 (blue contours in Figure 3.6, right) on the velocity map, a strong spatial correlation is evident between the dust emission and the red-shifted arc structure of the cloud. It suggests that the emitting region, which produces polarized light, is receding from us relative to a more blue-shifted background (Figure 3.6 right). A small clump located in the northern part of the map appears to account for the majority of the blue-shifted emission beyond −2 km s^{-1}; its corresponding spectrum is displayed in the right panel of Figure 3.7.

The left panels of Figure 3.7 present the integrated CO(3–2) spectra for the central region (left) and the dust lane (center); they display a two-component profile. Fitting these spectra with two Gaussian components yields standard deviations for the blue- and red-shifted components, (σ_B, σ_R) of (0.90 ± 0.02, 0.56 ± 0.01) km s^{-1} for the central region and (0.60 ± 0.03, 0.79 ± 0.02) km s^{-1} for the dust lane, with corresponding mean velocities of (−1.25, 0.89) km

s^{-1} and (−1.08, 0.57) km s^{-1}, respectively. The mean dust temperatures, taken from [111], are 29.7 K for the central region and 20.8 K for the dust lane. Given these temperatures, the contribution of thermal broadening to the total line width is minimal (at the per mil level), and thus can be considered negligible. The resulting non-thermal FWHM line widths are (ΔV_B, ΔV_R) = (2.12 ± 0.05, 1.32 ± 0.02) km s^{-1} for the central region, and (1.41 ± 0.07, 1.86 ± 0.05) km s^{-1} for the dust lane. Since the red-shifted spectral components align well with the regions of 850 μm polarized dust emission, their associated velocity dispersions are used in the magnetic field strength calculations discussed in the following section. However, to ensure conservative error estimates, I adopt uncertainties on the velocity dispersion based on the quadrature sum of three independent sources: ^{13}CO(1–0) line measurements from [163], and both the blue- and red-shifted CO(3–2) HARP spectra. The final adopted velocity dispersions are 1.32 ± 0.40 km s^{-1} and 1.86 ± 0.19 km s^{-1} for the central region and the dust lane, respectively. Although the velocity dispersions derived from the CO(3–2) red-shifted component and the ^{13}CO(1–0) emission agree within 20%, supporting the use of the CO(3–2) line to trace gas kinematics, I caution that the CO(3–2) line may not be optically thin. In this study, magnetic field strength estimates are made under the assumption that the CO(3–2) emission adequately traces the same dust volume probed by polarization observations.

3.3.2. Results

3.3.2.1. Magnetic Field Morphology

The magnetic field has been mapped across a region of roughly 1.6 pc, with a spatial resolution of ∼0.03 pc. The uneven mass distribution, together with multiple protostar candidates and the presence of an early-type B star, suggests that the magnetic field morphology in this area is likely to be highly complex. In the central part of the map, the brightest emission from LkHα 101, the field lines are oriented nearly along the north–south and east–west directions. Such a pattern is indicative of significant magnetic field turbulence or tangling within the dense core. This interpretation is further supported by the measured polarization angle dispersion of $\sigma_\theta \sim 15°$. Moving outward from the central region, where the gas density decreases, the magnetic field vectors tend to follow the boundary of the matter distribution. In the outermost areas, particularly where the emission contours (e.g., the green curve in Figure 4.1) exhibit high curvature, the magnetic field appears to align perpendicular to the contour shape. Within the dust lane, the dominant magnetic field orientation tends to follow the northwest–southeast filamentary structure. This trend is more evident in elongated clumps, where the magnetic field vectors are generally aligned with the filament axis.

The dust lane is identified as a subcritical filament (see Section 3.3.2.3), and the observed magnetic field orientation, mostly aligned with the filament's long axis, is consistent with the overall picture of magnetic field evolution in star-forming environments. Magnetic fields are generally perpendicular to gravitationally supercritical filaments but parallel to those that are subcritical [165, 58]. Observations from *Planck* and BLASTPol have revealed a transition from parallel to perpendicular alignment occurring at a visual extinction of $A_V \sim 3$ mag [39, 166]. More recently, observations in Serpens South using SOFIA data identified an additional transition, from perpendicular back to parallel, at higher extinction levels of $A_V \gtrsim 21$ mag [46]. Comparing this value with the Serpens South results, the dust lane region having a mean column density of 1.44×10^{22} cm^{-2} (see Table 3.2) has $A_V \sim 15.3$ mag with conversion factor between column densities and visual extinction $N(H_2) = 9.4 \times 10^{20}$ cm^{-2} A_V mag. The dust lane region is within the range where the magnetic field is expected to be perpendicular to the filament, and close to the transitional zone where the median relative orientation

between the magnetic field and filament approaches 45° (see Figure 3 of [46]). These findings suggest that the parallel-to-perpendicular transition may not be determined only by visual extinction but may also depend on other cloud-specific physical conditions. The central region is also subcritical. Its magnetic field morphology is highly complex, likely influenced by the early-type B star. This complexity highlights the need for broader statistical studies to better understand the governing parameters behind magnetic field–filament alignment in various environments.

3.3.2.2. Magnetic Field Strength

Table 3.2: Summary of physical parameters estimated for the central region and the dust lane.

		Central Region	Dust Lane
Herschel	$n(\mathrm{H_2})$ ($\mathrm{cm^{-3}}$)	$(1.22 \pm 0.50) \times 10^4$	$(1.25 \pm 0.46) \times 10^4$
	$N(\mathrm{H_2})$ ($\mathrm{cm^{-2}}$)	$(0.96 \pm 0.39) \times 10^{22}$	$(1.44 \pm 0.53) \times 10^{22}$
HARP	ΔV (km $\mathrm{s^{-1}}$)	1.32 ± 0.40	1.86 ± 0.19
Unsharp Masking	σ_θ (°)	14.9 ± 2.7	14.7 ± 2.6
	B_{POS} (μG)	91 ± 32	132 ± 27
	$\mathcal{M}_A$	0.52	0.52
	λ	0.27 ± 0.15	0.28 ± 0.12
Structure Function	σ_θ (°)	14.8 ± 4.8	16.9 ± 5.0
	B_{POS} (μG)	92 ± 42	144 ± 36
	$\mathcal{M}_A$	0.52	0.59
	λ	0.27 ± 0.16	0.32 ± 0.15

The magnetic field strengths derived using the two methods are summarized in Table 3.2 for both the central region and the dust lane. As shown, the results from the unsharp masking and structure function methods are consistent, B_{POS} ~91 μG for the central region and B_{POS} ~138 μG for the dust lane. Notably, the average field strength across the two regions, about 115 μG, closely matches the value of 100 μG studied by [167] to explain the observed fragmentation length scale in the star-forming filaments of the X-shaped Nebula in the California molecular cloud.

3.3.2.3. Mass-to-flux Ratio and Alfvénic Mach Number

By replacing the measured values of B_{POS} and $N(\mathrm{H_2})$ for the central region and the dust lane into Equation 3.2.3, I obtain the mass-to-flux ratios, λ, which are listed in Table 3.2.

The left panel of Figure 3.8 displays B_{POS} as a function of column density, $N(\mathrm{H_2})$, for these regions using the present results alongside data from previous POL-2 studies [147, 161, 168, 122, 41]. The dashed line represents the boundary between subcritical and supercritical conditions, calculated from Equation 3.2.3 by setting $\lambda = 1$, which corresponds to the threshold where gravitational and magnetic support are equal. Among the regions shown, LkHα 101 exhibits notably low $N(\mathrm{H_2})$ values. The Auriga-California region is above the critical boundary, indicating it is magnetically subcritical.

The right panel of Figure 3.8 presents the relation between B_{POS} and the mass-to-flux ratio, λ, for the same set of regions. The Auriga-California region has a rather low value of λ,

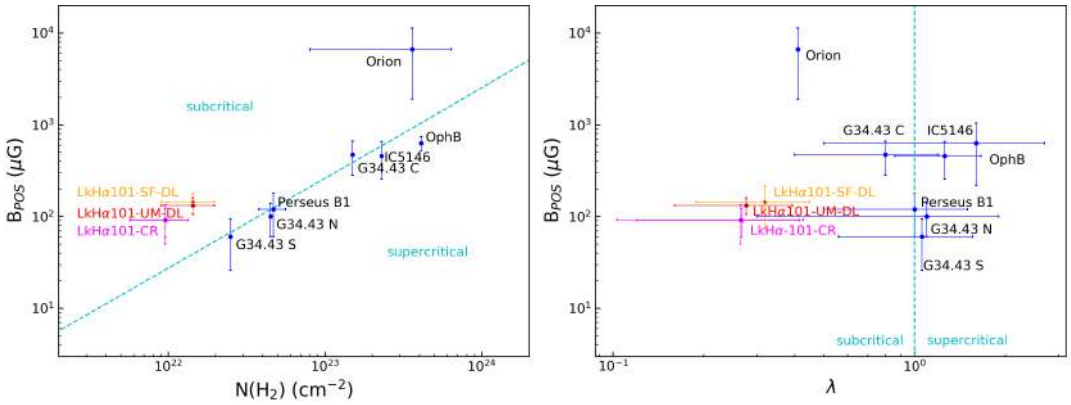

Figure 3.8: Dependence of the plane-of-sky magnetic field strength, $B_{\rm POS}$, on column density, $N(\mathrm{H_2})$ (left), and on the mass-to-flux ratio, λ (right). Red and yellow markers correspond to the dust lane, derived using the unsharp masking (UM) and structure function (SF) methods, respectively. Purple markers represent values for the central region. The dashed lines indicate the boundary between supercritical and subcritical regimes; in the left panel, this threshold is computed using Equation 3.2.3.

confirming its subcritical regime. The fact that the LkHα 101 region is both the densest part of Auriga-California and magnetically subcritical may help explain its very low star formation efficiency [112]. In addition, the measured Alfvénic Mach number, $\mathcal{M}_A \sim 0.52$–0.59, indicates that the magnetic field dominates over turbulence in this region, further emphasizing the significant role of magnetic support in regulating star formation.

3.4. Magnetic Fields in M17

Figure 3.9 shows the magnetic field orientation map of M17, maintaining only pixels after the master cut. The calculation of magnetic field strength is presented in Section 3.4.1. The results are presented in Section 3.4.2.

To investigate the magnetic field in M17, I divide the region into two sub-regions: North and South. As shown in Figure 3.13, the two ellipses outline areas that are distinct both spatially and in terms of their physical conditions, including differences in density, temperature, and kinematics, as further illustrated in Figures 3.11, 3.13, and 4.6. The northern ellipse is centered at R.A. $18^{\rm h}20^{\rm m}31^{\rm s}.6$, Dec. $-16°08'04''.3$, with major and minor axes of $137''$ and $69''$, respectively, and a position angle of $14°$. The southern ellipse is centered at R.A. $18^{\rm h}20^{\rm m}23^{\rm s}.2$, Dec. $-16°12'24''$, with major and minor axes of $200''$ and $143''$, and a position angle of $0°$. Based on these definitions, the map is divided into two corresponding sub-regions, referred to as M17-N and M17-S, which are used for all the following analyses. In the following sections, I identify the input parameters required for the DCF method to estimate the magnetic field strengths in each region.

3.4.1. Calculating Magnetic Field Strength

We derive the structure functions separately for M17-N and M17-S. Both regions exhibit a similar trend: the structure function rises at small separations, l, and then tends toward the angular dispersion expected for a random magnetic field, $52°$, at larger separations (see Figure 3.10; [154]). Since M17-N has a smaller spatial extent than M17-S, the largest separation sampled in M17-N is correspondingly smaller. The structure functions are fitted as a function of l using Equation 3.5. To exclude unresolved scales, only points with $l > 13.6''$, equal to

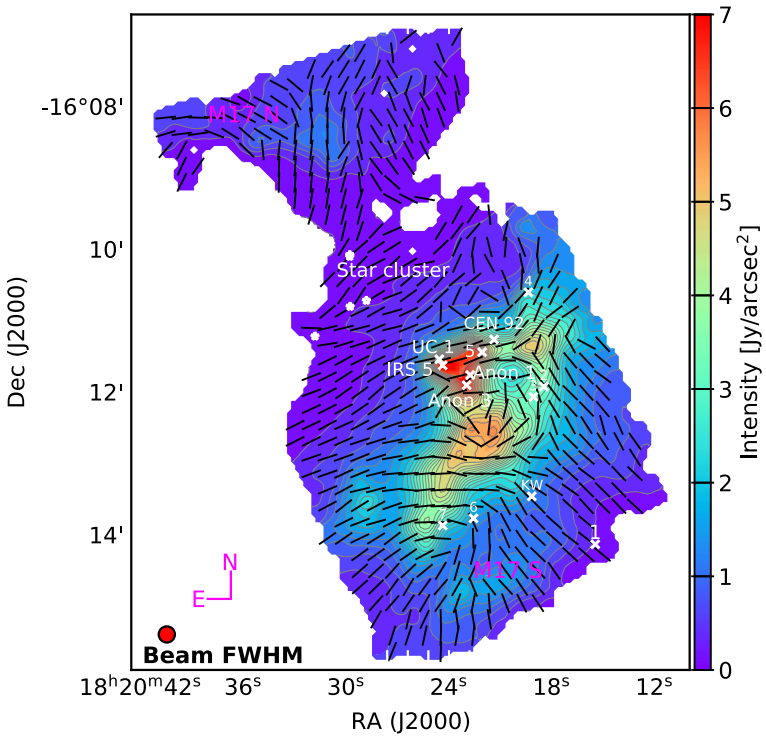

Figure 3.9: Magnetic field structure in M17 shown on the intensity map. Uniform half-vectors indicate the polarization angles after a 90° rotation, tracing the magnetic field orientation projected on the plane of the sky. Star symbols mark the positions of the most massive stars (spectral type > O7) in NGC 6618 [169]. M17-S contains several infrared sources, namely UC 1, IRS 5, CEN 92, Anon 1, and Anon 3. The Kleinmann–Wright (KW) object is a binary star system [170]. Source coordinates are adopted from [118].

the SOFIA/HAWC+ beam size, are included in the fit. The upper bound in l is selected to provide the best representation of the small-scale structure, as shown by the black curves in Figure 3.10.

Table 3.3 summarizes the values obtained, $b = 4.9° \pm 0.2°$ and $8.8° \pm 0.7°$, equivalent to $\sigma_\theta = 3.5° \pm 0.2°$ and $6.2° \pm 0.5°$ for M17-N and M17-S, respectively. The uncertainties on b are derived from the fitting process. These values are notably smaller than the dispersion measured by [158], who reported $\sigma_\theta \sim 10°$ in M17 using data from the Caltech Submillimeter Observatory at 350 μm and a resolution of $\sim 20''$. Table 3.3 also includes the ratios between the turbulent and large-scale components of the magnetic field. These ratios indicate that, in both regions, the turbulent magnetic field is significantly weaker than the large-scale ordered field, highlighting the dominance of ordered magnetic structure in M17.

3.4.1.1. Polarization Angle Dispersion: Structure function

3.4.1.2. Velocity Dispersion

For M17, the velocity dispersion is derived from archival ^{13}CO (J = 1 – 0) observations taken with the Nobeyama 45-m radio telescope [171]. These observations were performed at a central frequency of approximately 110.201 GHz and have a spectral resolution of 0.1 km s^{-1}. The resulting data cube has a pixel size of $7''.5$ and a beam size of $14''.9$. Figure 3.11 shows the integrated intensity map in the left panel and the intensity-weighted mean velocity

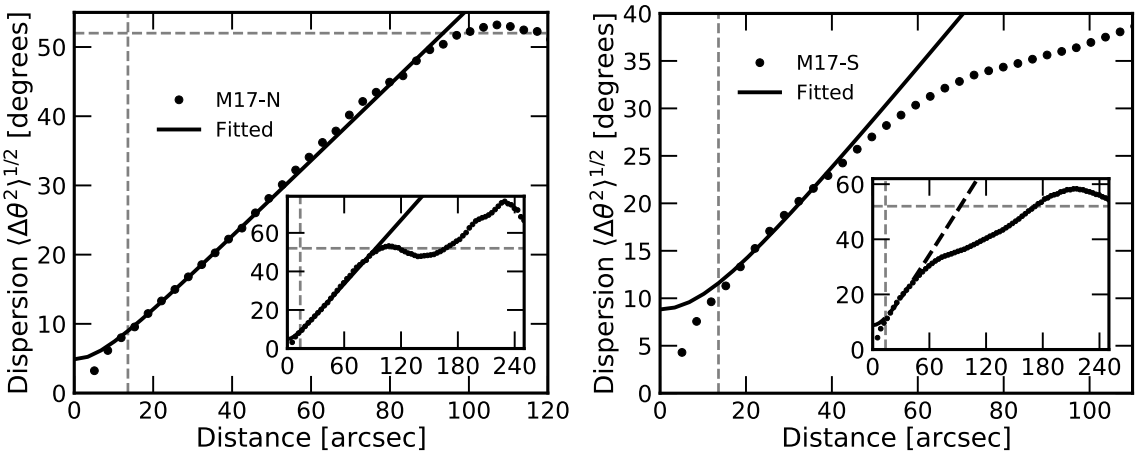

Figure 3.10: Structure functions $\langle \Delta\theta^2(l) \rangle^{1/2}$ for M17-N (left) and M17-S (right). Black markers represent the data, and black curves show the best-fit models. Insets display $\langle \Delta\theta^2(l) \rangle^{1/2}$ across the full range of separations l for each region. The horizontal dashed lines indicate the expected angular dispersion for a random magnetic field, $\pi/\sqrt{12} \approx 52°$ [154]. The vertical dashed lines denote the SOFIA/HAWC+ beam size of 13.6″ at 154 μm.

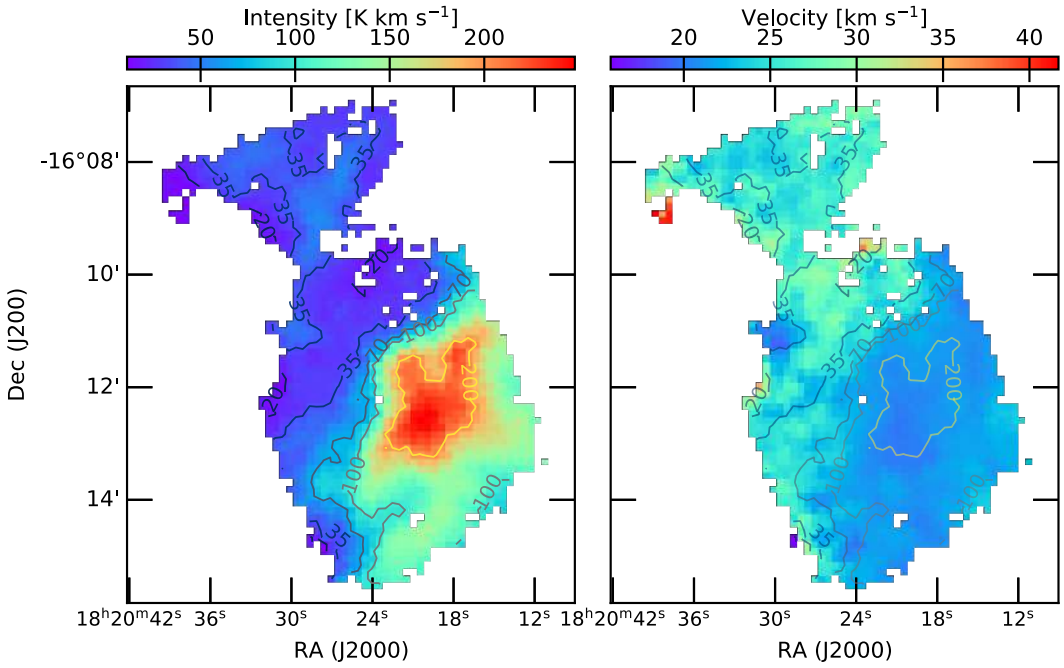

Figure 3.11: Left: Velocity-integrated intensity map of the ^{13}CO (J = 1 – 0) emission observed with the Nobeyama 45-m telescope. Right: Intensity-weighted mean velocity map. Contour levels for both panels are set at 20, 35, 70, 100, and 200 K km s^{-1}.

map in the right panel, both calculated over the local standard of rest velocity interval from -20 to 60 km s^{-1}.

Figure 3.12 presents the ^{13}CO spectra averaged in the M17-N (left) and M17-S (right) sub-regions. In both cases, the spectra are well described by two-component Gaussian fits, from which I extract the central velocities and velocity dispersions ($\sigma_{v;^{13}\mathrm{CO}}$) of the components. The main spectral peaks are found at 22.7 ± 1.6 km s^{-1} for M17-N and 19.9 ± 2.3 km s^{-1} for M17-S, respectively. As these primary components are significantly brighter than their secondary components, I adopt only the velocity dispersions of the main peaks for estimating the magnetic field strengths in the two sub-regions. The fitted results are summarized in Table 3.3, and are consistent with previous findings from [171, 172], although those studies covered larger areas of M17. The statistical uncertainties from the Gaussian fits are smaller than the spectral resolution of the Nobeyama observations. Therefore, I conservatively adopt the spectral resolution of 0.1 km s^{-1} as the uncertainty in the velocity dispersion measurements. We note that M17-N is influenced by outflows and shocks originating from G015.128 [118], a massive young stellar object, likely an A-type supergiant [173]. This source lies partially outside the coverage of the SOFIA/HAWC+ data. This object contributes to a higher level of turbulence in M17-N compared to M17-S.

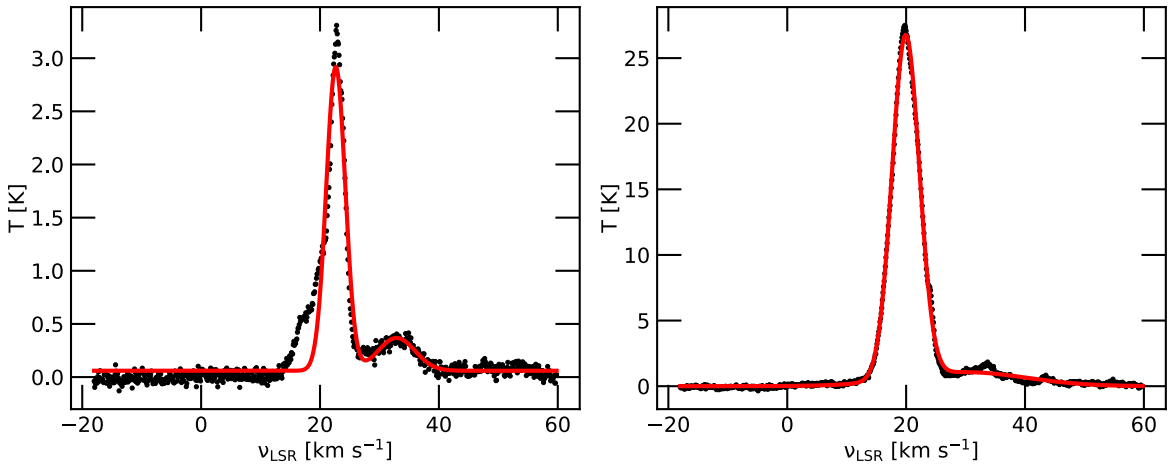

Figure 3.12: Average integrated Nobeyama 45m telescope ^{13}CO $(J = 1 - 0)$ spectra (black) with two-Gaussian fits (red) for M17-N (left) and M17-S (right).

The measured velocity dispersions are converted to non-thermal components. Adopting an average gas temperature of 20 K, as reported by [172], the thermal contribution to the total velocity dispersion is found to be negligible. Hence, I take the non-thermal velocity dispersions for the M17-N and M17-S sub-regions to be equal to the standard deviations of the main Gaussian components, as detailed in Table 3.3.

3.4.1.3. Column and Volume Densities

Figure 3.13 presents the resulting $N(\mathrm{H_2})$ column density map, overlaid with contours of dust temperature. The corresponding dust temperature distribution is shown separately in Figure 4.6. Using the column density map, I compute the total column densities, $N_{\mathrm{total,H_2}}$, and the average column densities, $\langle N(\mathrm{H_2})\rangle$, along with their associated uncertainties, $\sigma_{N(\mathrm{H_2})}$, for the M17-N and M17-S regions. These values are summarized in Table 3.3.

To estimate the volume density, $n(\mathrm{H_2})$, I follow the approach described in Section 3.3.1.3 of Lkhα 101 and by [163]. Using Equation 3.11, with $D = 1.98$ kpc is the adopted distance

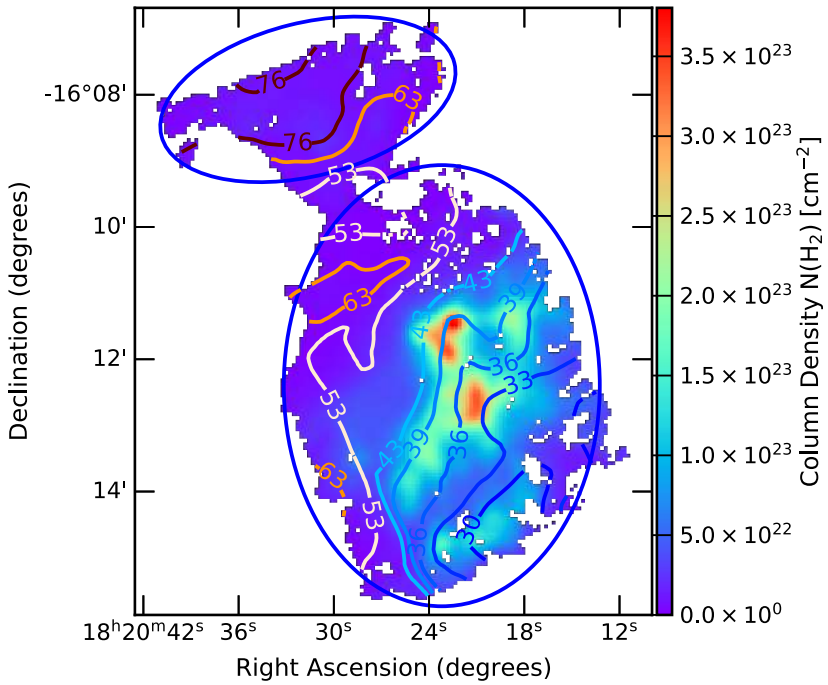

Figure 3.13: Column density map of M17, $N(\mathrm{H_2})$. Contours represent the dust temperature (T_d), as in Figure 4.6. The blue ellipses display the M17-N and M17-S sub-regions, as in Figure 4.5. In M17-S, the relation between T_d and $N(\mathrm{H_2})$ is non-monotonic: T_d increases with column density up to about 43 K, but decreases beyond this temperature.

to M17 [119], and $\Delta = 4''$ is the pixel size of the $N(\mathrm{H_2})$ map. The volume density is derived under the assumption that the molecular clumps have spherical geometry. As shown in Figure 3.13, I define two ellipses to enclose the observed M17-N and M17-S regions, with angular radii of $69''$ and $120''$, respectively.

The volume densities, $n(\mathrm{H_2})$, are presented in Table 3.3. The associated uncertainties are estimated under the assumption that the fractional uncertainty in $n(\mathrm{H_2})$ is equal to that of the total column density, $N_{\mathrm{total,H_2}}$, i.e. $\dfrac{\sigma_{n(\mathrm{H_2})}}{n(\mathrm{H_2})} = \dfrac{\sigma_{N(\mathrm{H_2})}}{\langle N(\mathrm{H_2})\rangle}$.

3.4.2. Results

3.4.2.1. Magnetic Field Morphology

The morphology of interstellar magnetic fields plays a critical role in shaping the star formation process. Observational data, therefore, offer a valuable key to test theoretical predictions on the role of magnetic fields in star-forming regions.

In the outer low-density region of M17, the magnetic field tends to be oriented perpendicular to the local matter distribution. This trend is visible in Figure 3.9, where many polarization half-vectors in low-density areas are aligned orthogonally to the intensity contours.

In the M17-N region, the magnetic field primarily runs in a north–south direction through the highest-density area, curving toward the eastern and western edges of the region (see Figure 3.9). The magnetic field morphology in M17-N resembles that of a gravitationally collapsing core in the presence of a strong magnetic field, commonly referred to as an hourglass morphology, characterized by straight field lines in the central region and curved lines at the two wings. This classical structure is frequently observed in both simulations and observa-

Table 3.3: Summary of the results from the DCF analysis of M17. The parameter b represents the rms contribution of the turbulent magnetic field component to the polarization angle dispersion, σ_θ, while m accounts for the contribution from the large-scale magnetic field. The ratio $\delta B / B_0$ quantifies the relative strength of the turbulent field component compared to the ordered (large-scale) field. Detailed definitions and discussion of these parameters are provided in the main text.

Parameters	M17-N	M17-S
b	4.9 ± 0.2	8.8 ± 0.7
m	0.55 ± 0.002	0.55 ± 0.01
$\delta B / B_0$	0.06	0.11
Polarization angle dispersion, σ_θ (deg)	3.5 ± 0.2	6.2 ± 0.5
Peak position, $v_{\rm LSR}$ (km s^{-1})	22.7 ± 0.1	19.9 ± 0.1
Velocity dispersion, $\sigma_{v,^{13}{\rm CO}}$ (km s^{-1})	1.6 ± 0.1	2.3 ± 0.1
Column density, $\langle N({\rm H_2}) \rangle$ (cm^{-2})	$(9.1 \pm 4.0) \times 10^{21}$	$(6.2 \pm 6.5) \times 10^{22}$
Volume density, $n({\rm H_2})$ (cm^{-3})	$(9.3 \pm 4.1) \times 10^{3}$	$(4.2 \pm 4.4) \times 10^{4}$

tions [e.g., 174, 175, 44]. However, it is important to note that M17-N, as defined here, is only a small portion of the larger M17-N region, which is not fully covered by the current SOFIA/HAWC+ observations. As such, the observed hourglass-like morphology could be coincidental, potentially resulting from magnetic fields tracing emission by polycyclic aromatic hydrocarbons observed by Spitzer at 8 μm. Distinguishing between these two scenarios will require wider-field observations with higher angular resolution.

In the M17-S region, the magnetic field generally appears oriented perpendicular to the major axis of the dense filament and forms an asymmetric, large-scale hourglass-like structure (Figure 3.9). In the southern part of the region, just below Anon 1 and Anon 3, the field vectors extend roughly east–west and gradually bend to the south. On the northern side, just above UC 1 and CEN 92, the field lines again appear curved. This hourglass-shaped configuration likely results from gravitational infall onto massive cores located near the center of M17-S, while the asymmetry may reflect the complex mass distribution in the central and northwestern parts of the region. An interesting feature in M17-S is the presence of a pillar-like structure, typical of photodissociation regions (see, e.g., [176]). I find a 'triangular' pillar, with the top end coincident with the locations of UC 1 and IRS 5, and a 'base' to the west. Notably, the magnetic field configuration around this pillar is consistent with what is seen in other photodissociation regions: the field lines run parallel to the pillar in regions close to the H II boundary, but become perpendicular to it behind the base, as reported by [176]. Earlier observations by [177] found that magnetic field morphology in M17 is elongated into the cloud core and bulges outward away from the H II region, which is thought to be heated by OB stars. This morphology is consistent with a scenario in which the H II region is actively expanding into the surrounding molecular cloud [178]. Taken together, the observations support a scenario in which the magnetic fields are distorted by the H II region, several IR sources, and nearby stellar clusters.

3.4.2.2. Magnetic Field Strength

We estimate the plane-of-sky magnetic field strength using Equation 3.1, based on the measured values of polarization angle dispersion (σ_θ), one-dimensional non-thermal velocity dis-

Table 3.4: Measured plane-of-sky magnetic field strengths, Alfvénic Mach numbers, and mass-to-flux ratios for M17-N and M17-S.

Region	$B_{\rm POS}$ (μG)	Mach number $\mathcal{M}_A$	Mass-to-flux ratio λ
M17-N	980 ± 230	0.12	0.07 ± 0.04
M17-S	1665 ± 885	0.22	0.28 ± 0.33

persion (σ_v), and volume density ($n(\mathrm{H_2})$) detailed in Table 3.3. This gives magnetic field strengths of $B_{\rm POS} = 980 \pm 230$ μG for M17-N and 1665 ± 885 μG for M17-S (see Table 3.4 for details). The higher magnetic field strength in M17-S is mainly due to its higher gas density.

We also note that the DCF method is valid in this case, as the measured polarization angle dispersions in both regions are below 25°, which is within the recommended limit for applying the method [54]. The uncertainties in $B_{\rm POS}$ are calculated by propagating the errors in σ_θ, σ_v, and $n(\mathrm{H_2})$ using Equation 3.2.

An earlier study by [179] reported a peak magnetic field strength of approximately 600 μG in the southwestern part of the M17 photodissociation region. The magnetic field strength along the line of sight was directly estimated using Zeeman splitting of H I lines toward the H II region, yielding $B_{\rm LOS} \sim -450$ to -550 μG [180]. A rough estimate of the magnetic field strength toward M17-S was also obtained from polarization measurements of point sources in the NIR and FIR [181]. They derived a total magnetic field strength of $B = \sqrt{B_{\rm LOS}^2 + B_{\rm POS}^2} \sim 230$ μG and estimated the inclination angle of the magnetic field vector relative to the plane of the sky to be around 40°. The measured plane-of-sky magnetic field strengths, $B_{\rm POS} = 980 \pm 230$ μG for M17-N and 1665 ± 885 μG for M17-S, are broadly consistent with these earlier results within their rather large uncertainties.

Several factors influence our estimates of the magnetic field strengths. One major source of uncertainty arises from the assumption of spherical geometry when estimating the radii of the molecular clumps, which is used in calculating the volume densities. Depending on the true 3D geometries of the clouds, this assumption could lead to a high error in the derived values of $B_{\rm POS}$. Another factor is the integration of emission along the entire line of sight, leading to an underestimation of σ_θ and, consequently, an overestimation of the magnetic field strength. It is also worth noting that the DCF method can statistically overestimate $B_{\rm POS}$ by up to a factor of two in individual molecular clouds [54]. In addition, the DCF method relies on the assumption that the magnetic and turbulent energies are balanced.

3.4.2.3. Mass-to-flux Ratio and Alfvénic Mach Number

In this analysis, using Equation 3.2.3, we find $\lambda = 0.07$ for M17-N and $\lambda = 0.28$ for M17-S (see Table 3.4). These values indicate that the M17 cloud is magnetically subcritical overall, suggesting that it is supported by magnetic fields and follows the strong-field model of star formation [38]. However, since these values are calculated as averages across the entire subregions, it is still possible for dense cores within them to become locally supercritical and collapse to form stars. These inferred values are also consistent with the ambipolar diffusion model, in which magnetic fields are gradually dragged inward from the cloud's outer layers into the dense cores. This interpretation is supported by previous findings that massive star formation is limited in M17, and that the region lacks gravitationally bound clumps [172].

Using the polarization angle dispersions listed in Table 3.3, I calculate $\mathcal{M}_A = 0.12$ for M17-N and 0.22 for M17-S by Equation 3.10. These low values confirm that both sub-regions are sub-Alfvénic, meaning that magnetic fields are stronger than turbulent motions. This is consistent with the relatively well-ordered magnetic field morphology observed in the region (see Figure 3.9).

3.5. Magnetic Fields in G11

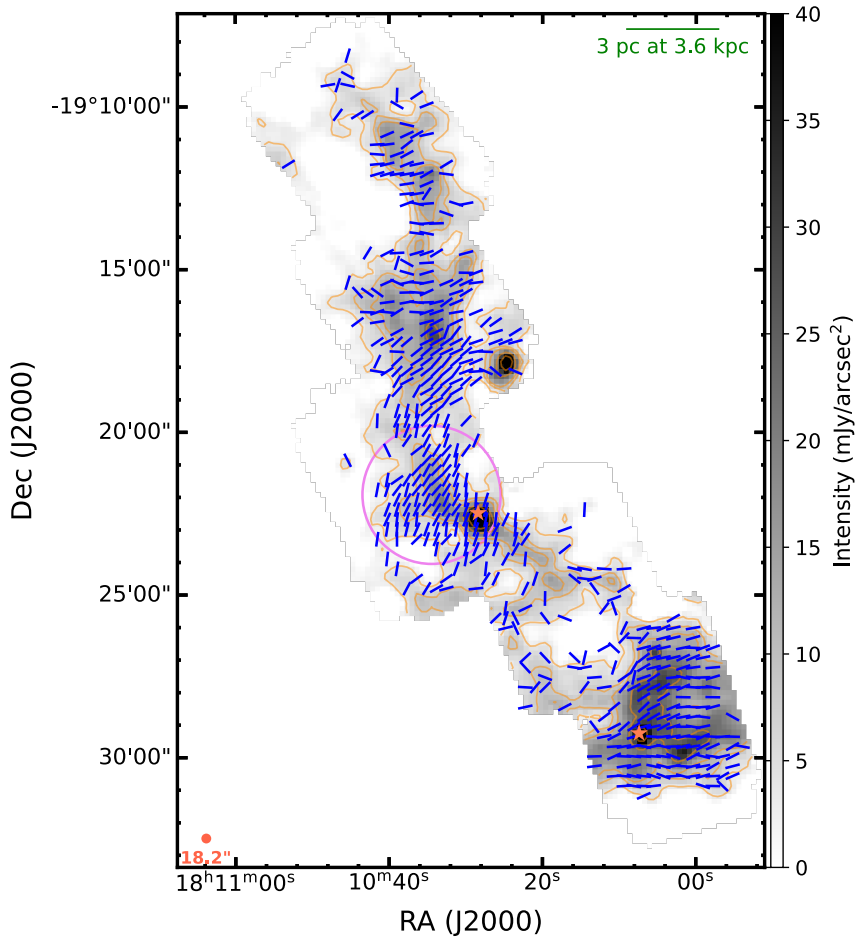

Figure 3.14: Map of magnetic field orientation toward G11 at 214 μm, observed with SOFIA/HAWC+. Blue line segments represent the inferred magnetic field orientation, with spacing between segments equal to the beam size. The SOFIA/HAWC+ beam at this wavelength is 18.″2, indicated by the red circle in the lower-left corner. The segments are overlaid on a grayscale map of total intensity (I). Orange contours correspond to intensity levels of $I = 3.6$, 8.4, 12.0, 24.0, and 42.0 mJy arcsec^{-2}. Red stars mark the positions of two massive protostellar candidates, P1 (central) and P6 (southern), identified by [131]. The violet circle indicates the region observed with JCMT/SCUPOL; its corresponding magnetic field map is shown in Figure 3.18.

Figure 3.14 presents the magnetic field orientation map of the G11 filament, showing only the pixels retained after applying the master selection criteria. The method used to calculate the magnetic field strength is described in Section 3.5.1, and the corresponding results are provided in Section 3.5.2.

3.5.1. Calculating Magnetic Field Strength in G11

Unlike the calculations performed for LkHα 101 and M17 in previous sections, here I compute a map of the magnetic field strength for G11. To derive this map using Equation 3.1, I generate three corresponding parameter maps: polarization angle dispersion (σ_θ), velocity dispersion (ΔV), and volume density ($n(\mathrm{H_2})$). The methods used to construct these maps are described in the following sub-sections.

3.5.1.1. Polarization Angle Dispersion

To estimate the polarization angle dispersion caused by the turbulent component of the magnetic field, I apply the unsharp masking method, originally introduced by [147]. This technique was first used to estimate the mean magnetic field strength in OMC-1 within the Orion A filament. Later, Hwang et al. [159] adapted the method to compute the polarization angle dispersion pixel by pixel, thereby enabling the construction of a magnetic field strength map for the same region.

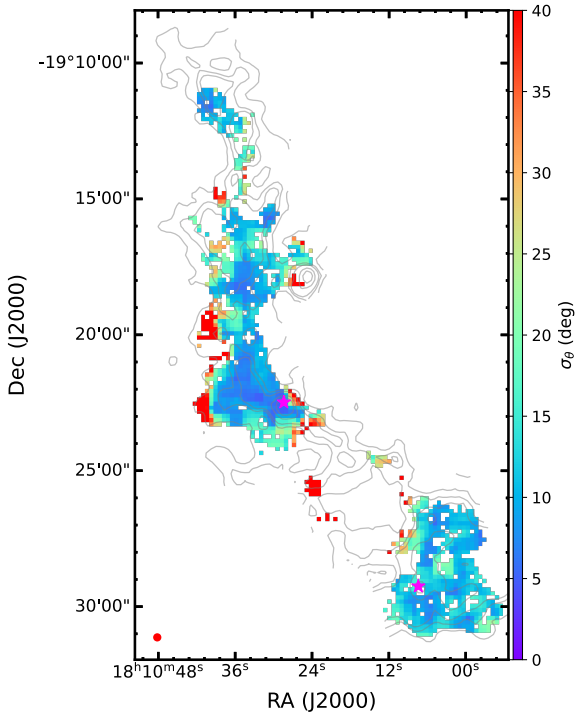

Figure 3.15: Polarization angle dispersion map of G11. The overlaid contours are the same as those shown in Figure 3.14.

In this study, I follow a similar approach. First, I calculate the mean polarization angle, $\bar{\theta}$, within a 5×5 pixel box, corresponding to approximately two times the beam size, following practices adopted in previous works such as [159, 149]. Next, I compute the angle dispersion as the root-mean-square (RMS) of the differences between the polarization angle at each pixel (θ_i) and the mean angle in the box ($\bar{\theta}$), $\sigma_\theta = \sqrt{\sum_{i=1}^{N}(\theta_i - \bar{\theta})^2 / N}$, where N is the number of valid pixels within the box after applying the general data selection criteria described in Chapter 2. To ensure statistical significance, I require $N > 13$ (i.e., more than 50% of the 25 pixels in the box). This calculation is repeated across the entire map by slipping the box from pixel to pixel. The resulting polarization angle dispersion map is shown in Figure 3.15.

3.5.1.2. *Velocity Dispersion*

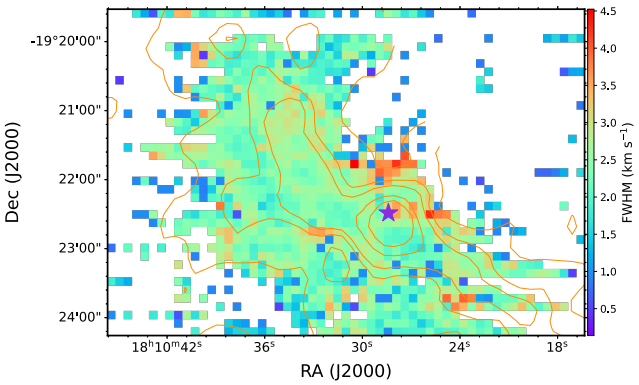

Figure 3.16: Map of the FWHM of the non-thermal component derived from ^{13}CO spectral line observations for the central region. The overlaid contours are identical to those shown in Figure 3.14. The star symbol marks the position of the protostellar source P1.

To construct a pixel-by-pixel map of magnetic field strengths, the velocity dispersion at each pixel is needed. This, in turn, demands high S/Ns and high spectral resolution to ensure reliable Gaussian fitting of the line profiles. Archival data of sufficient quality is only available around the central region of G11.

I use ^{13}CO(3–2) spectral line data from the JCMT Science Archive[1] to derive the FWHM map of the non-thermal component, ΔV. CO emission traces a broad range of H_2 number densities from 10^2 to 10^4 cm^{-3}, with ^{13}CO typically probing moderate densities around 10^3 cm^{-3} [182, 183, 184].

The ^{13}CO(3–2) observations of the G11 central region come from JCMT proposal M15AI41 and were obtained on 2 April 2015. They were taken with HARP, which was set to a central frequency of 330.587 GHz. The total on-source integration time was 1675 s, and the atmospheric opacity at 225 GHz varied between 0.039 and 0.047. Reduction of the data was carried out with the ORAC pipeline [164] and the `Kernel Application Package (KAPPA)` [152], both provided within the Starlink software. The spectra originally had a velocity resolution of 0.055 km s^{-1}, which was subsequently smoothed to a final resolution of 0.2 km s^{-1}. Each pixel's spectrum was then fitted with a Gaussian profile using the `fit1d` task from the `SMURF` package [110], resulting in a FWHM map of the total line width, $\Delta V^2_{\mathrm{total},^{13}\mathrm{CO}}$. The non-thermal velocity dispersion, ΔV, was calculated by removing the thermal contribution. Assuming an average gas temperature of 20 K, the thermal component is negligible. The resulting non-thermal velocity dispersion map for the central region is shown in Figure 3.16.

3.5.1.3. *Volume Densities*

To calculate the volume densities, I use the column density ($N(\mathrm{H_2})$) and dust temperature (T_d) maps derived by [17] from multi-wavelength *Herschel* observations. These maps have an angular resolution of 43″ and a pixel size of 11.″5 × 11.″5. The spine of the G11 filament was identified with the `RadFil` algorithm [185], resulting in a length of 22 pc and a width of 1.0 pc [17].

[1] https://www.cadc-ccda.hia-iha.nrc-cnrc.gc.ca/en/jcmt/

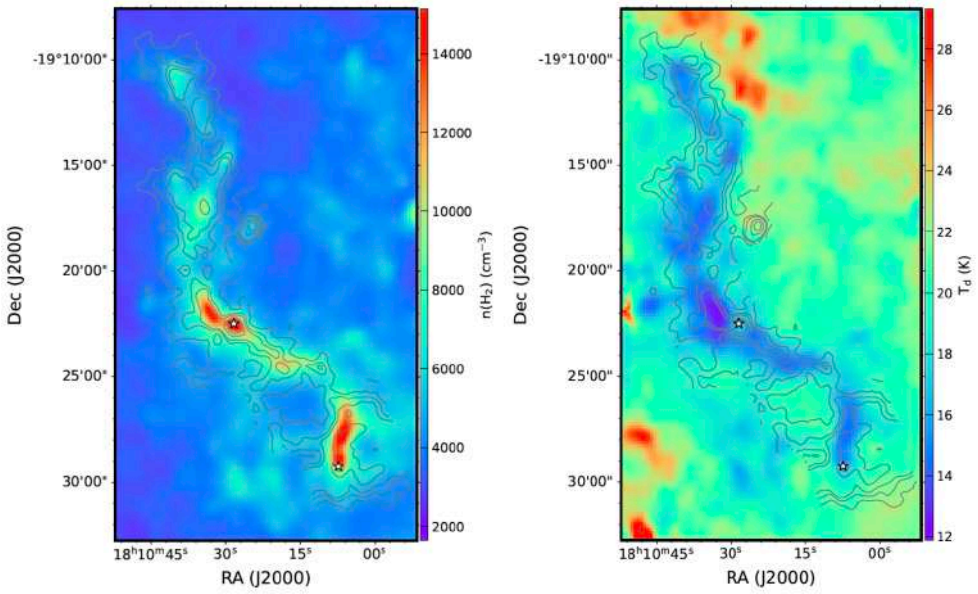

Figure 3.17: Maps of volume density $n(\mathrm{H_2})$ (left) and dust temperature T_d (right) for G11. Contours are the same as in Figure 3.14.

.

Assuming that the filament has a cylindrical geometry, I take the depth along the line of sight to be equal to its width. The volume density is then computed using: $n(\mathrm{H_2}) = \frac{\mathrm{N(H_2)}}{\mathrm{W}}$, where $W = 1.0$ pc is the assumed depth of the filament. The resulting maps of $n(\mathrm{H_2})$ and T_d are shown in Figure 3.17. The derived volume densities range from 10^3 to 10^5 cm^{-3}.

3.5.2. Results

3.5.2.1. Magnetic Field Morphology

To compare the magnetic field morphology observed by SOFIA/HAWC+ with that from JCMT/SCUPOL[2] [186, 133], I overlay the magnetic field segments from both instruments in Figure 3.18, focusing on the central region where SCUPOL data are available. The JCMT/SCUPOL data are filtered using the criteria: S/N in polarization $S/N(P) > 3$, polarization angle uncertainty $\delta\theta < 8°$, and polarization fraction $P < 5\%$. Overall, the two observations show consistent magnetic field orientations. However, the polarization degree measured by SOFIA/HAWC+ is significantly higher than that reported by JCMT/SCUPOL. This discrepancy may arise from differences in instrumental systematics as well as intrinsic astrophysical factors such as dust temperature, density, and composition, whether grains are spatially separated or mixed along the line of sight, across different wavelengths [100, 101]. Notably, SOFIA/HAWC+ at 214 μm traces warmer dust, which is associated with stronger radiation fields. According to RAT theory, grains exposed to more intense radiation are more efficiently aligned with the magnetic field, leading to higher polarization fractions compared to colder dust. While this explanation is qualitatively consistent with the observed difference, a full quantitative investigation is beyond the scope of the current studies.

MHD simulations predict that magnetic fields tend to align perpendicular to filament spines, particularly in denser regions [187]. In this section, we test this in the G11 filament.

[2] https://www.cadc-ccda.hia-iha.nrc-cnrc.gc.ca/en/community/scupollegacy/

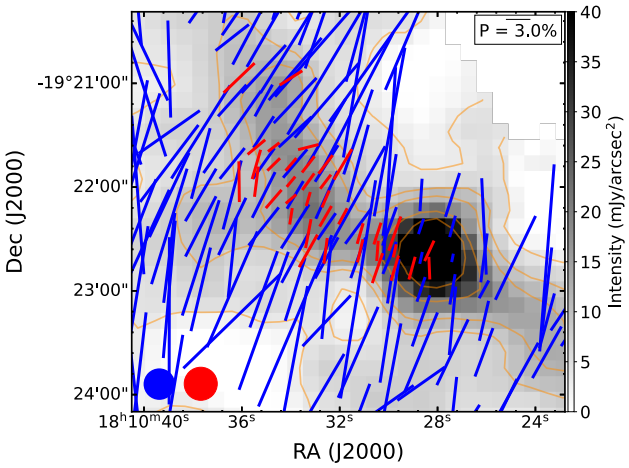

Figure 3.18: Comparison of magnetic field orientations observed by SOFIA/HAWC+ at 214 μm (blue segments) and JCMT/SCUPOL at 850 μm (red segments). Segment lengths are scaled according to polarization fraction, with a reference vector of 3% shown in the upper-right corner. The beam sizes are indicated in the lower-left: 18.″2 for SOFIA/HAWC+ (blue circle) and 20″ for JCMT/SCUPOL (red circle). The background contours are identical to those shown in Figure 3.14.

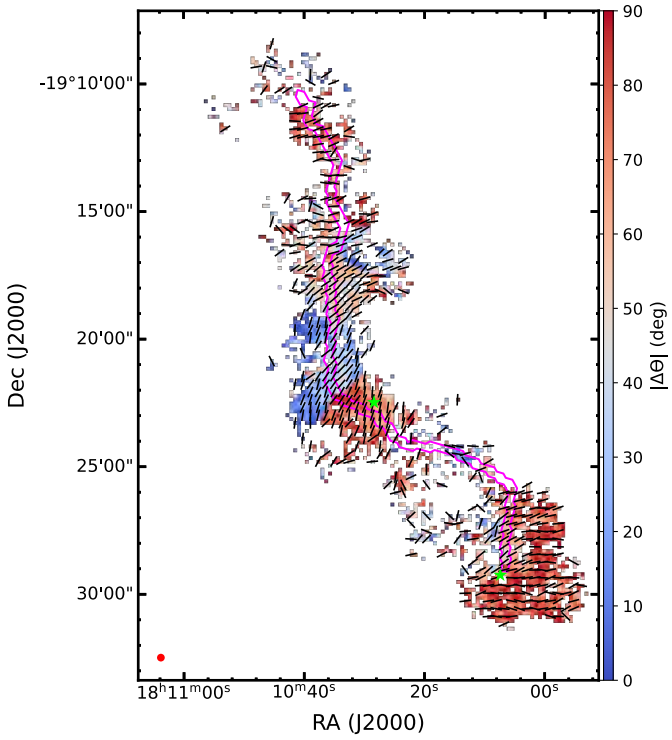

Figure 3.19: Map of the absolute angular difference between the magnetic field orientation and the direction of the filament spine (see text for details). The magenta contour represents the filament spine. Black segments indicate the magnetic field orientation, with segment lengths proportional to the polarization fraction at each pixel. The green stars mark the positions of the protostellar candidates P1 and P6.

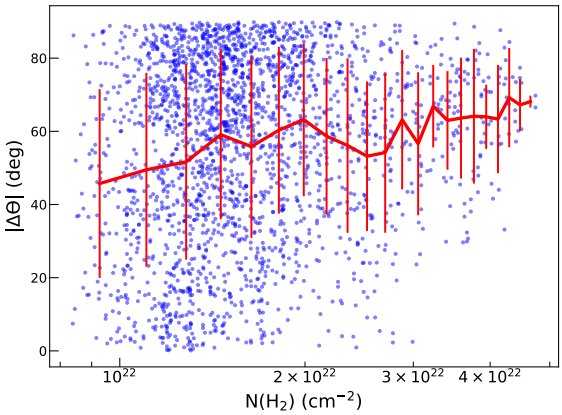

Figure 3.20: Dependence of the absolute angular difference, $|\Delta\Theta|$, between the magnetic field orientation and filament spine direction on column density. The thick red curve represents the running mean of $|\Delta\Theta|$, and the error bars indicate the root-mean-square (RMS) within each bin. A bin size of 1.77×10^{21} cm^{-2} is used.

I adopt the filament spine identified by the `RadFil` algorithm [185], shown as the magenta contour in Figure 3.19. A mask of the column density map is generated by applying a threshold approximately 2σ above the mean background. The spine is then determined through medial axis skeletonization, which identifies points equidistant to multiple boundary locations of the mask [188, 185]. To compare the magnetic field orientation with the filament's structure, I calculate the angular difference, $\Delta\Theta$, between the magnetic field orientation at each pixel and the tangent angle of the closest point along the spine. Figure 3.19 presents a map of the absolute angle differences, $|\Delta\Theta|$, showing that most magnetic field vectors are nearly perpendicular to the spine (red pixels in the map).

In addition, I examine how the relative orientation depends on column density. Figure 3.20 shows that $|\Delta\Theta|$ does not decrease with increasing column density, indicating a transition from parallel alignment in low-density regions to perpendicular alignment in high-density regions. This trend is consistent with previous observational studies using *Planck* and other facilities [39, 189]. Using polarimetric data from SOFIA/HAWC+, I derived the magnetic field orientation map of G11 and found that the magnetic fields are mostly perpendicular to the filament's spine, especially in the densest parts of the filament. Given that the SOFIA/HAWC+ data primarily trace regions with column densities above 10^{22} cm^{-2}, these findings align well with the observed column density threshold ($N_{\rm H} \gtrsim 3$–5×10^{21} cm^{-2}) above which magnetic fields become perpendicular to filaments, as reported in previous works [39, 190, 187].

3.5.2.2. Magnetic Field Strength in G11

We use Equation 3.1 to compute the magnetic field strength for each pixel where the polarization angle dispersion, σ_θ, is smaller than 25°, as recommended by [59]. Figure 3.21 presents the resulting map of magnetic field strengths toward the central region of G11. The strength values range from about 100 μG in the outer areas to around 600 μG along the filament spine, with a mean value of 235 μG. Pixel-by-pixel mapping of magnetic field strengths has been carried out in only a few previous studies, such as for Orion A [149, 159], Monoceros R2 [191], and 30 Doradus [192]. Earlier investigations typically reported only spatially averaged

field strengths rather than resolved maps. To validate the robustness of the derived magnetic field map for G11, I also apply the structure function method [158], to estimate the mean field strength over the central region.

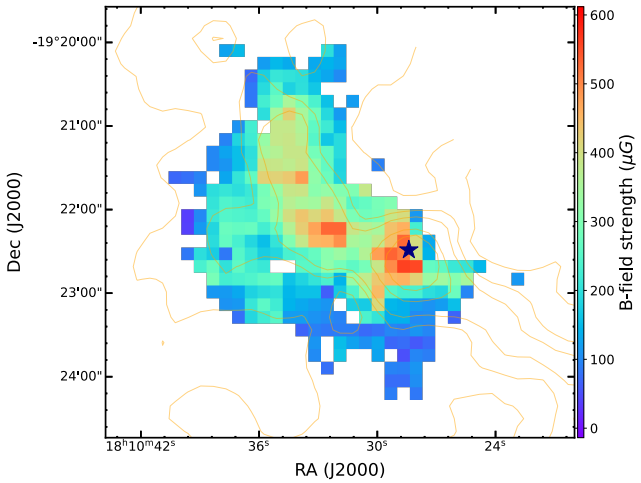

Figure 3.21: Map of plane-of-sky magnetic field strengths calculated on a pixel-by-pixel basis toward the central region of G11. The purple star marks the position of the massive protostellar candidate P1. Contours are the same as those shown in Figure 3.14.

The magnetic field strengths across G11 range from 100–600 μG, with stronger fields concentrated near the dense filament spine and weaker fields in the outer regions. These values are in good agreement with previous estimates. [133] derived a lower limit of ~200 μG toward the densest part of the central region using JCMT/SCUPOL. I obtain a polarization angle dispersion of $\sigma_\theta = 10.5° \pm 4.6°$. The average hydrogen number density and non-thermal velocity dispersion are $n(\mathrm{H_2}) = (8.0 \pm 1.4) \times 10^3$ cm^{-3} and $\Delta V = 2.4 \pm 0.4$ km s^{-1}, respectively. Substituting these values into Equation 3.1 yields a mean plane-of-sky magnetic field strength of $B_{\mathrm{POS}} = 242 \pm 50$ μG. This value is consistent with the pixel-based field strength distribution and supports the reliability of the mapping procedure.

The magnetic field strengths measured in G11 are comparable to those found in other massive filaments, including ~50 μG in G35.39 −0.33 [120], ~100–800 μG in NGC 6334 [124], ~60–470 μG in G34.43 +0.24 [122], ~20–100 μG in G47.06 +0.26 [125], and ~600–1000 μG in DR 21 [193]. These comparisons confirm that the magnetic field strength values derived for G11 are consistent with broader trends seen in massive filaments.

3.5.2.3. Mass-to-flux Ratios and Alfvén Mach Number

To further assess the influence of magnetic fields relative to gravity and turbulence, I computed the mass-to-flux ratio, λ, and the Alfvén Mach number, $\mathcal{M}_A$.

Figure 3.22 presents a map of the mass-to-flux ratio in the central region of G11. In this figure, blue pixels indicate sub-critical regions ($\lambda < 1$), where magnetic support dominates over gravity, while red pixels supercritical regions ($\lambda > 1$), where gravity can overcome magnetic support and trigger collapse. The map reveals that most of the central region is sub-critical, suggesting that gravitational collapse is largely suppressed and that the filament is likely in an early evolutionary phase. This supports a scenario in which material is still accreting from the surrounding lower-density medium along magnetic field lines onto the filament's spine. Notably, the southwestern portion of the region is supercritical and corresponds

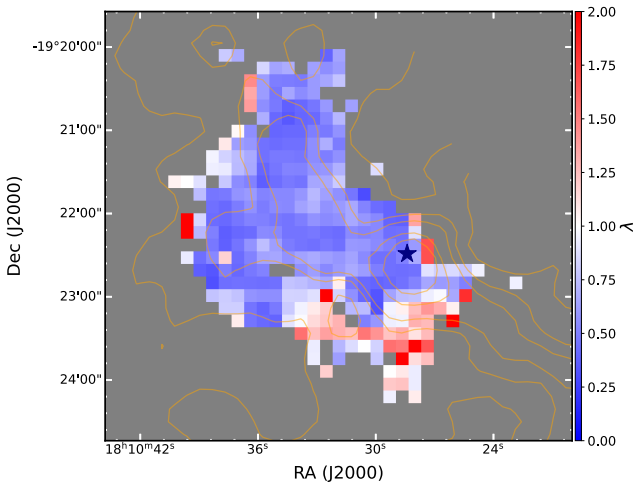

Figure 3.22: Map of the mass-to-flux ratio, λ, toward the central region of G11. The violet star marks the location of the massive protostellar candidate P1. The overlaid contours are the same as those shown in Figure 3.14.

closely to the location of the massive protostellar candidate P1, marked by the violet star in the figure. The $\mathcal{M}_A$ map (see Figure 3.23) reveals that the majority of the filament remains sub-Alfvénic, reaffirming that magnetic fields dominate over turbulence. These findings support the picture that the G11 filament is in an early evolutionary stage, where magnetic fields significantly influence its development and structure.

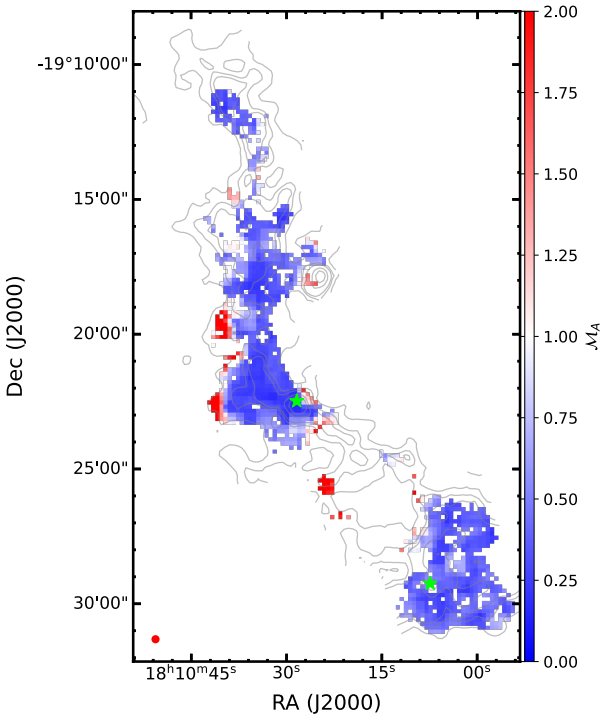

Figure 3.23: Map of the Alfvén Mach number, $\mathcal{M}_{\rm A}$, toward the central region of G11. Violet stars indicate the positions of the massive protostellar candidates P1 and P6. The contours are the same as in Figure 3.14.

3.6. Conclusions

Using thermal dust emissions toward Lkhα 101, M17, and G11.11 -0.12 observed by JCMT and SOFIA, the morphology and strength of magnetic fields in each region have been analyzed. The main results are summarized as follows:

LkHα 101: JCMT/POL-2 dust polarization observations at 850 μm were used.

1. The magnetic field morphology in the LkHα 101 region has been measured for the first time. While the magnetic field in the dust lane is largely aligned with its filamentary structure, the field becomes more complex in the central region. In lower-density clumps, particularly those that are elongated, the magnetic field tends to follow the local matter distribution.

2. The estimated plane-of-sky magnetic field strengths are ~91 μG in the central region and ~138 μG in the dust lane. These values are consistent across both the unsharp masking and structure function methods used to determine the polarization angle dispersion..

3. The mass-to-flux ratios, expressed in units of the critical value, are $\lambda = 0.27$ for the central region and $\lambda = 0.30$ for the dust lane. The regions are magnetically sub-critical, and magnetic fields are sufficiently strong to prevent gravitational collapse. The Alfvénic Mach numbers are found to be smaller than one, suggesting that magnetic fields dominate over turbulence. Notably, although LkHα 101 is the densest part of the Auriga-California cloud, its sub-critical supports the observed inefficiency of star formation in the region.

M17: SOFIA/HAWC+ dust polarization observations at 154 μm were used.

1. The plane-of-sky magnetic field strengths are estimated to be 980 ± 230 μG in the lower-density region (M17-N) and 1665 ± 885 μG in the higher-density region (M17-S).

2. In M17-N, the magnetic field structure takes the form of a gravitationally-collapsing core, with field lines running mostly north–south and curving at the edges. In M17-S, the field is more organized and follows the direction of gravitational collapse, forming an asymmetric hourglass shape centered around dense regions.

3. The measured Alfvénic Mach numbers are sub-Alfvénic, indicating that magnetic energy dominates over turbulent energy. Additionally, the mass-to-flux ratios are sub-critical, implying that the magnetic field is strong enough to resist gravitational collapse. These findings are consistent with the low efficiency of massive star formation reported in previous studies of this region.

G11.11 -0.12: SOFIA/HAWC+ dust polarization observations at 214 μm were used.

1. The magnetic field orientation has been derived. The field morphology reveals that the magnetic fields are predominantly perpendicular to the filament's spine.

2. The pixel-by-pixel map of magnetic field strength has been calculated for the central region using the DCF method. The field strengths range from approximately 100 to 600 μG, with the strongest fields located near the filament's dense spine and weaker fields toward its more diffuse outer regions.

3. Maps of the mass-to-flux ratio and Alfv'enic Mach number indicate that the central region is magnetically sub-critical and sub-Alfvénic, implying that magnetic fields play a dominant role over gravity and turbulence in shaping the filament's structure and dynamics. These results are consistent with the interpretation that G11 is in an early evolutionary stage, where magnetic fields shape its structure and dynamics and also guide the accretion of material from the surrounding low-density medium onto the filament's spine.

Chapter 4

Observational Studies of Grain Alignment and Evolution

Thermal dust polarization offers a powerful tool for tracing magnetic fields and constraining dust grain properties such as size, composition, and alignment efficiency. This chapter focuses on observational evidence of the Radiative Torque Alignment (RAT-A) and Radiative Torque Disruption (RAT-D) theories. I aim to understand how the polarization fraction varies under different environmental conditions, such as dust temperature, gas column density, and magnetic field structure.

Using high-resolution polarization data from JCMT/POL-2 and SOFIA/HAWC+, I examine the dust physics across a diverse set of environments: the Auriga-California molecular cloud, the massive star-forming region M17, and the filamentary infrared dark cloud G11.11–0.12. These sources were chosen for their contrasting radiation fields, gas densities, and magnetic field configurations, providing a robust framework to test theoretical predictions.

4.1. Introduction

Dust constitutes an essential component of the ISM, significantly influencing numerous astrophysical processes such as heating and cooling of interstellar gas, star and planet formation, and astrochemical processes on grain surfaces (see [194] for an overview). Additionally, polarized starlight [52, 51] and polarized thermal dust emission [195] induced by dust grains aligned with magnetic fields have become critical tools for observing magnetic fields. Furthermore, dust polarization provides valuable insights into dust physics, including grain size, shape, and composition (see e.g., [81]).

Currently, the most widely accepted grain alignment mechanism is RAT-A [89]. RAT-A theory predicts the alignment efficiency to vary with local environmental conditions, notably gas density and radiation field intensity. Specifically, the degree of alignment is expected to decrease in denser regions mainly due to gas randomization but increase in regions with stronger radiation fields or higher dust temperatures due to the more efficient alignment of grains [196, 197]. As a result, RAT-A theory predicts two critical observational signatures: (1) a decrease in polarization fraction, P, with increasing gas density, and (2) an increase in P with enhanced radiation intensity or higher dust temperatures (see [96]).

Past tests of RAT-A theory using starlight polarization observations generally support these predictions (see [155]). Observations consistently report a decline in polarization fraction with increasing gas column density, which is known as the polarization hole, across

optical-NIR (e.g., [198]) and far-IR/submillimeter wavelengths [199]. Numerical models by [198, 96] demonstrate that the polarization hole can result from the loss of grain alignment in dense regions with low radiation fields, consistent with RAT-A predictions. Comprehensive discussions of successful RAT-A tests using starlight polarization can be found in [155].

However, comprehensive testing of RAT-A using thermal dust polarization remains limited. Specifically, there is ongoing debate over the cause of polarization holes observed at FIR/submillimeter wavelengths in molecular clouds and star-forming regions. In diffuse and translucent clouds, observational data (e.g., [98]) and numerical simulations (e.g., [200]) suggest that fluctuations in magnetic fields rather than grain alignment loss explain the polarization hole. Moreover, the projection of magnetic fields onto the light of sight significantly impacts polarization fractions [201]. Observations further indicate that polarization fraction does not always correlate positively with dust temperature [67], challenging a central prediction of RAT-A theory.

To resolve this puzzle, Hoang et al. [97] introduced the RAT-D mechanism. RAT-D hypothesizes that strong radiation fields accelerate large dust grains to rapid rotation, causing centrifugal stress that disrupts these grains into smaller fragments. Numerical modeling of thermal dust polarization by [100] employing RAT-A and RAT-D (the RAT paradigm) successfully reproduced the observed decrease in polarization fraction at high dust temperatures seen by *Planck*. This occurs because grain disruption narrows the aligned grain size distribution, reducing polarization at far-IR/sub-mm wavelengths (see Figure 7 in [99] for a detail). Polarization fractions were shown to initially rise and then decrease with increasing dust temperatures in OMC-1 and ρ Ophiuchus A, highlighting the combined effects of RAT-A and RAT-D [101, 202].

Earlier investigations of dust grain alignment and grain properties mainly relied on starlight polarization [see 155]. However, thermal dust polarization has become increasingly important for probing alignment in denser molecular cloud environments. Moreover, testing the RAT paradigm, both RAT-A and RAT-D, requires observations of molecular clouds under a wide range of conditions, such as varying locations, masses, densities, and radiation fields. This thesis builds upon that shift in focus by utilizing FIR and submillimeter thermal emission in more complex, denser regions with various conditions. I concentrate on two key aspects of dust physics: grain alignment and grain evolution. Grain alignment refers to the alignment of dust grains to magnetic fields under the influence of local radiation and gas conditions. Grain evolution involves the size and structure of grains, including growth and rotational disruption by RATs. This chapter presents an observational perspective, while the following chapter will focus on numerical modeling of dust polarization. I provide a comprehensive analysis of dust polarization across three molecular clouds: Auriga (LkHα 101), M17, and G11.11 −0.12, which is presented in detail in this Chapter.

4.2. Grain Alignment in Auriga

In this section, I investigate the variations in polarization fraction in the Auriga-California region, around the B-star, LkHα 101, and explore grain alignment physics.

4.2.1. Polarization Hole

Figure 4.1 presents the map of inferred magnetic field segments, similar to Figure 3.1, the segment lengths are now scaled according to the polarization fraction. As evident from the figure, the polarization fraction is higher in the more diffuse regions, whereas it drops significantly in the dense central area associated with the high emission intensity (yellow contours).

To examine the variation of the polarization fraction with total intensity, Figure 4.2 dis-

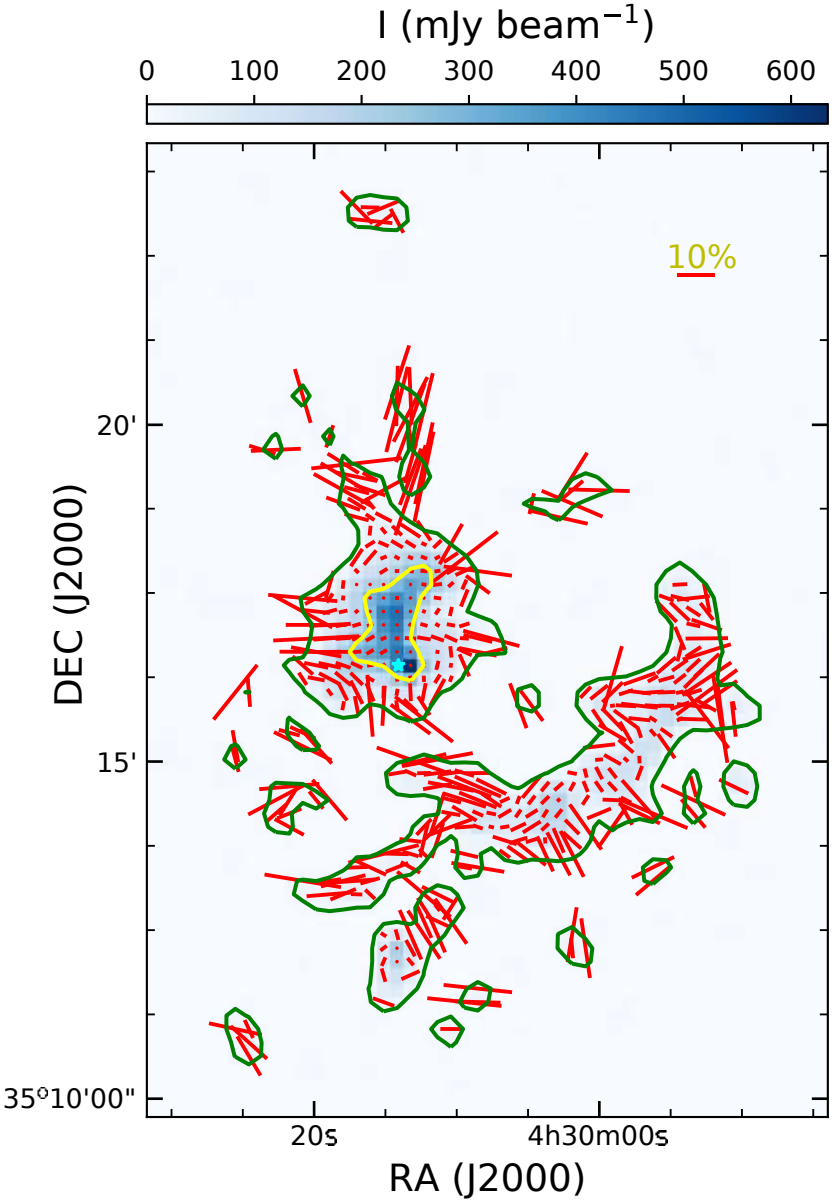

Figure 4.1: As in Figure 3.1, but here the line segment lengths scale with the polarization fraction, $P(\%)$. A reference segment of 10% is included for comparison.

plays P (%) as a function of I, after applying the δP–$\delta\theta$ cut to the data. The polarization fraction is observed to decrease with increasing intensity, a trend commonly referred to as the *polarization hole*. A power-law fit of the form $P \propto I^{-\alpha}$ yields a best-fit index of $\alpha = 0.82 \pm 0.03$. This uncertainty is derived from the fitting procedure and does not account for systematic errors. The obtained value of α for the LkHα 101 region lies within the typical range for molecular clouds, between 0.5 and 1. For comparison, previous BISTRO survey results observed by JCMT report $\alpha = 0.8$ for ρ Ophiuchus A [203], 0.9 for ρ Ophiuchus B [161], 1.0 for ρ Ophiuchus C [162], and 0.9 for Perseus B1 [168]. Using a different methodology that relied on non-debiased data, lower values were obtained—$\alpha = 0.34$ for Oph A and $\alpha = 0.6$–0.7 for Oph B and C [44]. The parameter α is widely used as a proxy for the

efficiency of dust grain alignment. A value of $\alpha = 0$ corresponds to constant alignment efficiency throughout the cloud, while $\alpha = 1$ implies that grain alignment is restricted to the outer layers, with complete loss of alignment in the interior [198]. Observational studies have reported $\alpha \sim 1$ in starless cores with high visual extinction ($A_V \sim 20$), consistent with the loss of grain alignment as predicted by RAT theory [204, 205, 206, 96]. Thus, the measured index $\alpha = 0.82$ in Auriga indicates that grain alignment occurs within the cloud, but with reduced efficiency, consistent with RAT alignment theory predictions [89, 85] in which stellar radiation from the LkHα101 star can align grains even in the dense region.

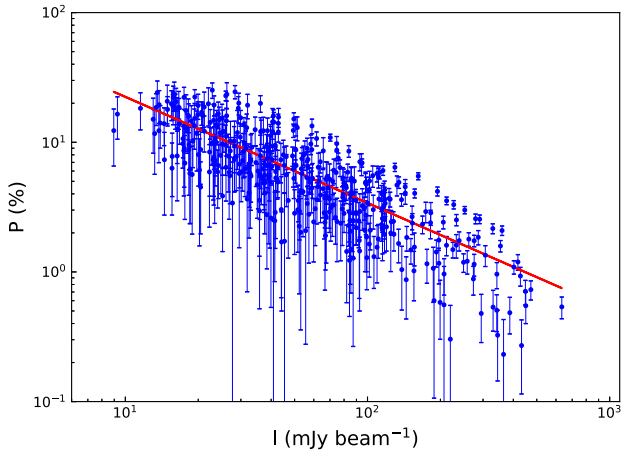

Figure 4.2: Dependence of polarization fraction on the total intensity. P tends to decrease with increasing I. The solid line is the best fit to a power law function.

4.2.2. Implications for Grain Alignment and Rotational Disruption by RATs around the LkHα 101 Star

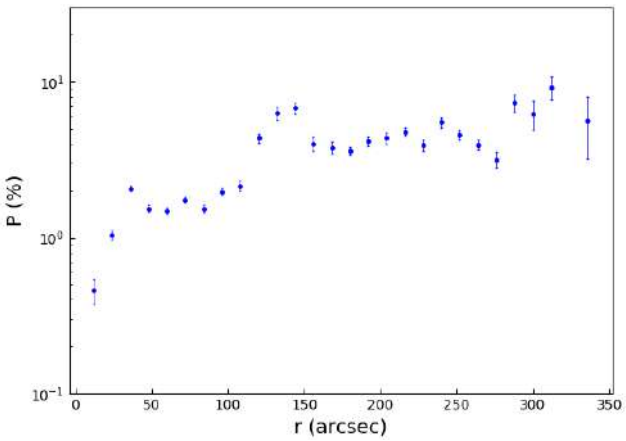

Figure 4.3: Dependence of P on the distance from LkHα 101. The polarization fraction decreases with r for $r < 150''$.

LkHα 101 is the only early B-type star present in this region. To examine its influence on dust polarization, Figure 4.3 shows how the polarization fraction varies radially, averaged in a 12″-wide rings centered on the star. I find a noticeable drop in polarization within ~150 arcsec of the star. LkHα 101 is about 15 times more massive than the Sun and has a luminosity of 8×10^3 L$_\odot$ [114]. The angular distance at which its radiation energy density equals the

typical interstellar radiation field (2.19×10^{-12} erg cm^{-3}; [2]) is roughly 3300 arcsec, far larger than the distance where the polarization fraction begins to decline.

To investigate this drop feature in P, particularly within $r < 150''$, I examine how the polarization fraction P, column density $N(H_2)$, and dust temperature T_d vary with distance from the star. The latter two quantities are derived from *Herschel* observations [111]. The upper left panel of Figure 4.4 shows a dust temperature map overlaid with contours of 850 μm emission. In the upper right panel, P is plotted as a function of distance r, along with power-law fits of the form $P = ar^b$. The data indicate two distinct regimes: for $r < 130''$, the fitted slope is $b = 0.86 \pm 0.04$, while for $r > 130''$, it is $b = 0.35 \pm 0.05$. This transition near $r \sim 130''$ aligns with a local minimum in column density (Figure 4.4, lower right), marking the boundary between the dense core and the more extended dust lane. Beyond $r = 130''$, the polarization degree declines slowly as the distance to the star decreases, suggesting a slow reduction in alignment efficiency. In contrast, within this radius, P drops off much more steeply. Concurrently, T_d increases with proximity to the star, as expected due to stellar heating (Figure 4.4, lower left), except for two points very close to the star ($r < 25''$) where T_d shows a slight dip. It is also notable that LkHα 101 lies near the peak of the column density distribution (Figure 4.4, lower right; see also Figure 3.5).

In theory, there are two main physical explanations for the sharp decline in P: (1) a drop in grain alignment efficiency, or (2) strong variation of the magnetic fields. According to RAT alignment theory ([89]), alignment becomes less efficient either due to reduced radiation and/or the increase of the gas density that enhances grain randomization. However, in this scenario, the radiation field strengthens closer to the star, and the gas density is not very high, $n(H_2) \sim 10^4$ cm^{-3}. Under such conditions, RAT theory predicts stronger grain alignment near the star, particularly since increasing the local radiation energy density described by T_d [96]. Thus, the rapid observed decline of P within $r < 130''$, despite dust temperatures exceeding 25 K, appears inconsistent with standard RAT-A predictions [100], and may point to additional physical processes at play.

Hoang et al. [97] proposed RAT-D, which disrupts dust grains into smaller fragments. RAT-D was modeled in detail for a dense cloud with an embedded radiation source in [96]. Because large grains dominate the emission responsible for dust polarization at FIR and sub-millimeter wavelengths, their destruction can reduce the overall polarization fraction as the local radiation energy density increases [100]. For a hydrogen number density of $n(H_2) \sim 10^4$ cm^{-3} (see Table 3.2), the polarization fraction initially increases with grain temperature by stronger radiation flux, but begins to decline once T_d exceeds approximately 25 K [100]. This prediction aligns well with the observed drop in P at smaller radii (or higher T_d) shown in Figure 4.4. Supporting evidence from previous observations by *Planck* [207] and SOFIA/HAWC+ [101] also revealed a decrease in P at high dust temperatures, consistent with the RAT-D mechanism. A detailed radiative transfer model to interpret P versus r is beyond the scope of this study.

Another explanation often given for the drop in polarization fraction with intensity or column density is magnetic field tangling along the line of sight [see review by 147]. However, no quantitative study to date has explicitly evaluated the role of magnetic field tangling in producing polarization holes on the spatial scales probed by JCMT or higher-resolution facilities such as CARMA[1], SMA[2], or ALMA[3]. Analyses of the *Planck* polarization data

[1] Combined Array for Research in Millimeter-wave Astronomy

[2] Submillimeter Array

[3] Atacama Large Millimeter/submillimeter Array

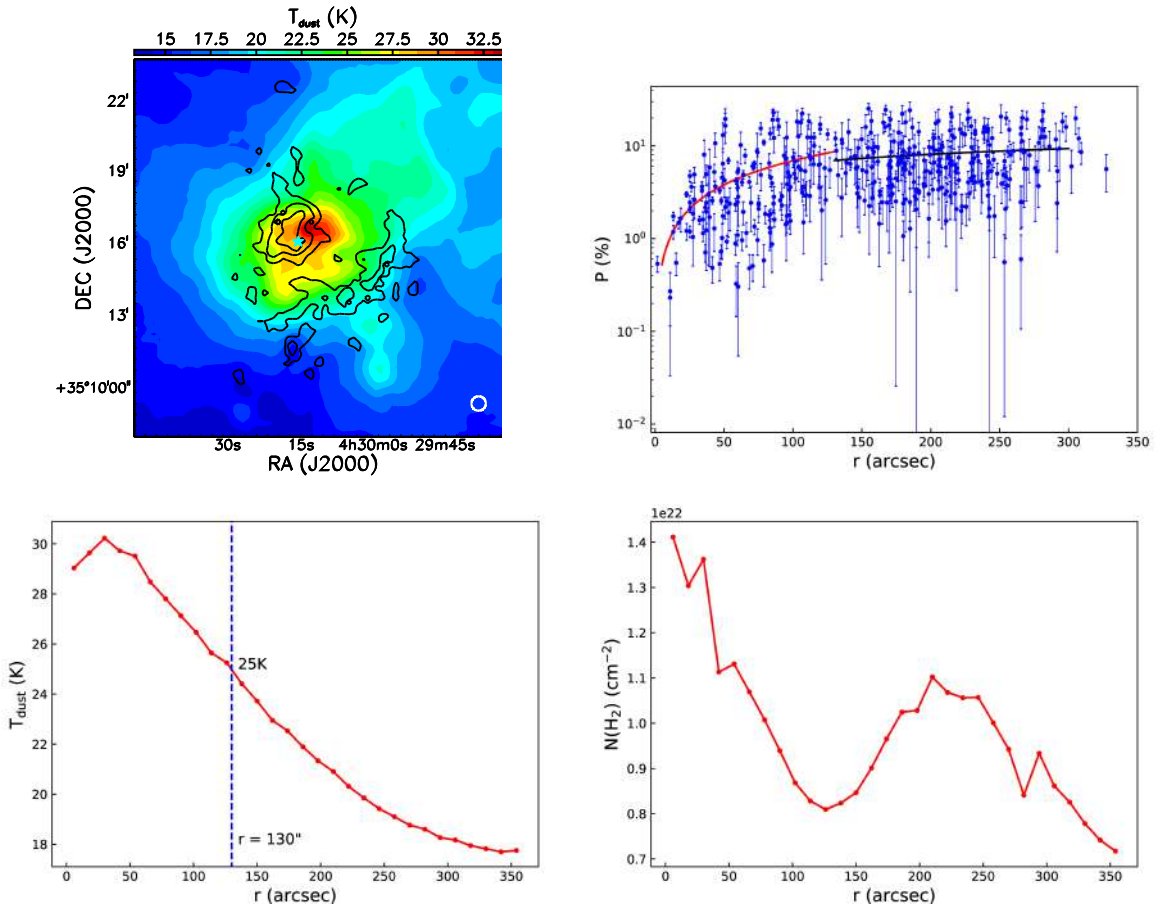

Figure 4.4: Upper left: Dust temperature map (color scale) overlaid with 850 μm continuum emission contours. The *Herschel* beam size (36.6″) is indicated in the bottom right corner. The location of the early B-type star LkHα 101 is marked by a cyan star. Upper right: Variation of polarization fraction P with distance r from LkHα 101. Power-law fits are applied separately for $r < 130''$ (red curve) and $r > 130''$ (black curve); see text for details. Lower left: Dust temperature $T_{\rm dust}$ as a function of distance r. The vertical dashed blue line denotes $r = 130''$, where the average dust temperature is approximately 25 K. Lower right: Column density $N(\mathrm{H_2})$ as a function of distance r.

[e.g., 77, 67] attributed the polarization hole effect entirely to turbulent tangling of magnetic fields along the line of sight, with dust grain–alignment efficiency remaining constant across a broad range of column densities. These spatial scales, however, are significantly larger than those probed by JCMT observations. Similar results were obtained from statistical analyses of ALMA data at spatial scales more comparable to JCMT [208].

In summary, in the absence of field tangling, polarization holes observed toward protostars cannot be consistent with RAT alignment theory alone, but can instead be explained by the combined effects of grain alignment and rotational disruption by RATs. Several possible mechanisms are currently under investigation to account for polarization holes, including RAT-D and magnetic field tangling. Comprehensive dust polarization modeling that incorporates grain alignment, disruption processes, and realistic magnetic field structures is necessary to clarify the origin of the polarization hole.

4.3. Grain Alignment and Disruption in M17

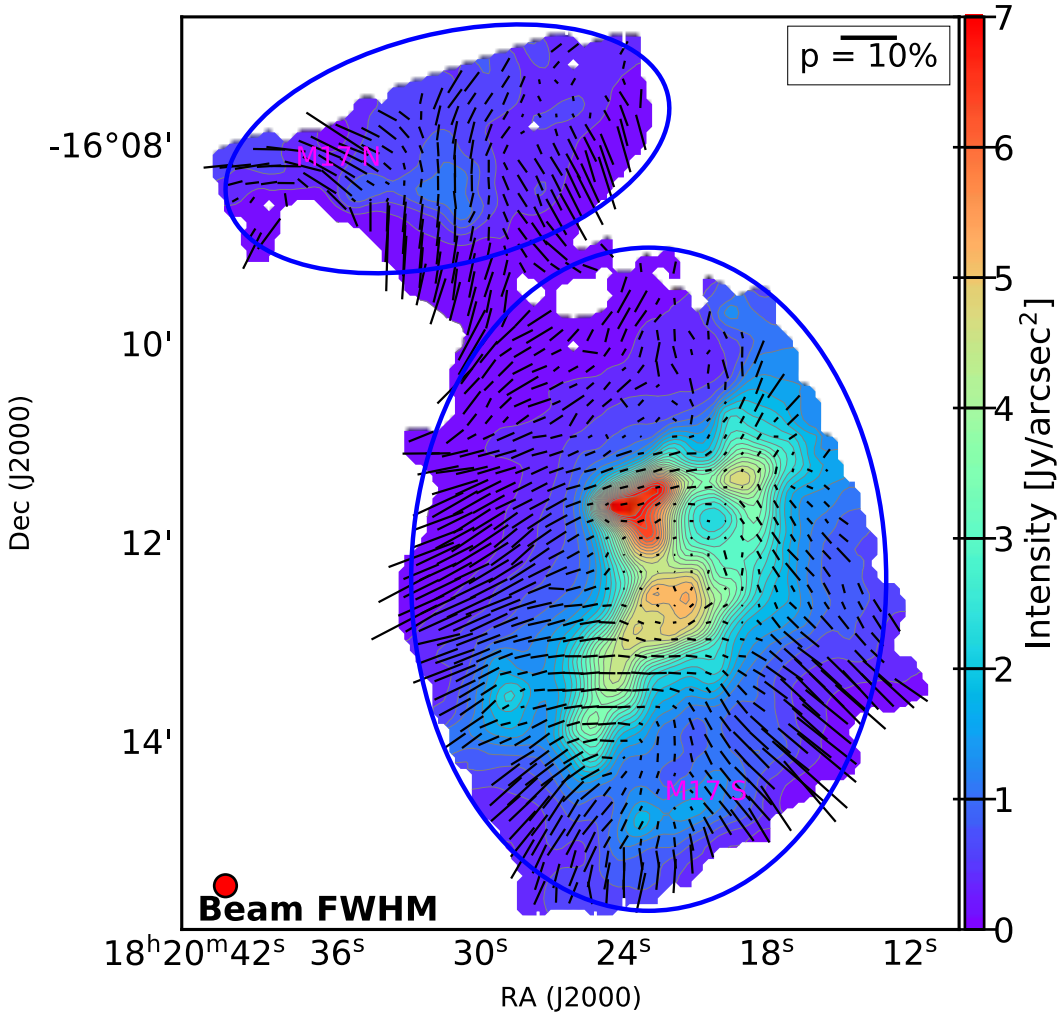

Figure 4.5: Map of the inferred magnetic field orientation in the M17 region observed with SOFIA/HAWC+. The half-vectors indicate the direction of magnetic fields (polarization angles rotated by 90°), with lengths proportional to the polarization fraction. The background color scale represents the total intensity. A reference segment indicating 10% polarization is provided in the upper right corner. The two blue ellipses highlight the M17-N and M17-S regions discussed in the text.

As with the magnetic field analysis of M17 in the previous chapter, I divide the region into two sub-regions, M17-N and M17-S, for a detailed examination of the dust physics. These sub-regions are marked by the ellipses in Figure 4.5.

4.3.1. Dust Temperature Map

As discussed in Section 3.4.1.3, the dust temperature map, $T_{\rm d}$, is obtained from graybody fitting to the *Herschel* data. This template map is subsequently regridded onto the SCUBA2 850; μm grid, resulting in a final pixel size of 4″.

The derived dust temperature map is presented in Figure 4.6. The average temperatures are 74 ± 11,K for M17-N and 43 ± 10,K for M17-S. Over the whole M17 region, the temperature generally decreases from east to west and from north to south, supporting the picture

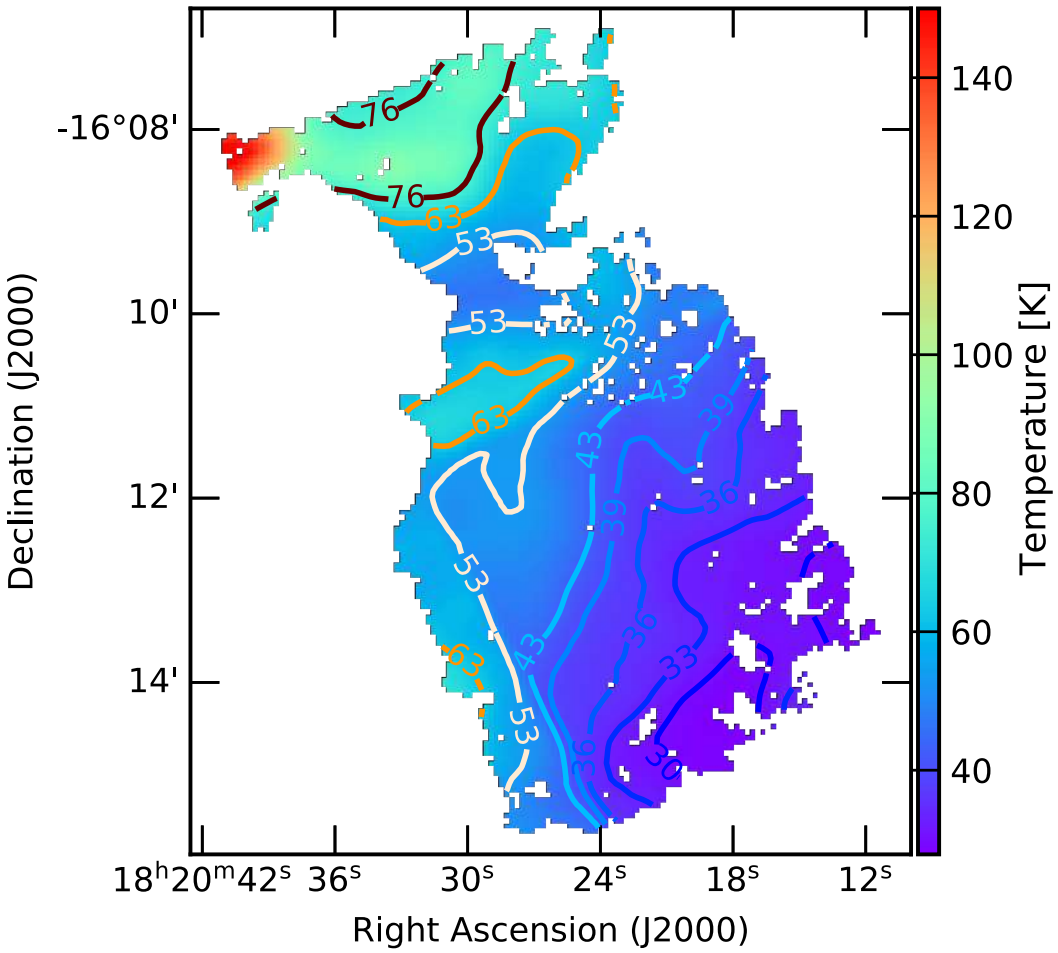

Figure 4.6: Dust temperature map of the M17 region, with selected contours indicating constant temperature values. In the M17-S region, the dust temperature generally decreases from east to west, in the direction moving away from the central star cluster.

that dust heating is mainly driven by the nearby massive star cluster. The higher temperatures observed in M17-N, as well as in the eastern and northeastern portions of M17-S, are likely due to their proximity to the star cluster and thus strongly heated by this intense radiation source and the adjacent H II region in the east. Within M17-S, the dust temperature clearly decreases with increasing distance from the star cluster. This cooling trend results from dust absorption within dense structures, whose densities are approximately an order of magnitude higher than those found in M17-N.

4.3.2. Polarization Fraction versus Emission Intensity, Column Density, and Dust Temperature

I now examine how the polarization fraction, P, varies with the total intensity, I, gas column density, $N(\mathrm{H_2})$, and dust temperature, T_d. These relationships provide fundamental insights into grain alignment and disruption processes occurring in M17.

Firstly, I investigate how P varies with I. Figure 4.5 clearly indicates that polarization fraction decreases with increasing intensity. Typically, this dependence can be characterized by a power-law of the form $P \propto I^{-\alpha}$, reflecting variations in grain alignment efficiency and magnetic field structure across the cloud. In Figure 4.7, a power-law fit applied to the entire M17 region yields $\alpha = 0.51 \pm 0.01$. Similar indices are derived when separately fitting data

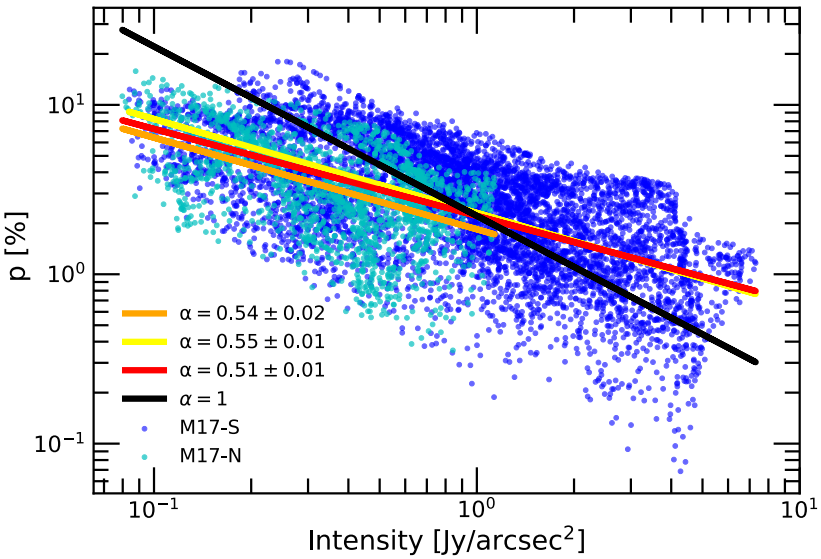

Figure 4.7: Variation of the polarization fraction with total intensity. The orange, yellow, and red lines represent best-fit power-law models for the M17-N region, the M17-S region, and the entire map, respectively. The black solid line indicates a reference power-law model with an index of $\alpha = 1$.

from M17-N ($\alpha = 0.54 \pm 0.02$) and M17-S ($\alpha = 0.55 \pm 0.01$). These indices suggest that grains retain partial alignment even towards regions of higher emission intensity [e.g. 44].

To further investigate variations in P, I analyze its dependence on $N(\mathrm{H_2})$ and T_d. The top-left panel of Figure 4.8 presents the relationship between P and $N(\mathrm{H_2})$. I determine the slopes by fitting piece-wise linear functions to the data. In M17-S, polarization fraction gently declines as gas column density increases, followed by a sharper decrease (slope -0.71) at $N(\mathrm{H_2}) > 3 \times 10^{22}$ cm^{-2}, corresponding to visual extinction $A_\mathrm{V} > 37$ mag. In contrast, M17-N shows a pronounced decrease with a slope of -0.67 at lower column densities ($N(\mathrm{H_2}) > 5 \times 10^{21}$ cm^{-2} or $A_\mathrm{V} > 6$ mag). This notable depolarization in M17-N occurs in regions of comparatively lower gas density but higher dust temperature relative to M17-S (see Figure 4.6). The top-right panel of Figure 4.8 represents the correlation between P and T_d. The polarization fraction initially decreases, subsequently rises, and eventually declines again as dust temperature increases. The initial decrease and subsequent increase originate primarily from M17-S, while the decline is observed in M17-N.

The bottom panel of Figure 4.8 illustrates how gas column density varies with dust temperature. In M17-S, column density rapidly decreases as dust temperature increases, whereas it changes more slowly in M17-N. The initial decrease of polarization degree observed at dust temperatures below 40 K corresponds to regions of high gas density ($A_\mathrm{V} \sim 100$ mag). This reduction in polarization is likely due to reduced grain alignment efficiency arising from weakened radiation fields and increased randomization through gas collisions. As dust temperature continues to rise, the density decreases, enhancing grain alignment efficiency closer to the luminous source, and consequently causing P to increase again. These trends align with predictions from the RAT-A theory. However, in the M17-N region, where dust temperatures reach up to approximately 150 K and gas densities are comparatively lower, the polarization fraction steadily decreases as temperature increases. This behavior significantly contradicts the expectations of the RAT-A theory, highlighting the need for further investigation into the grain alignment processes under such conditions.

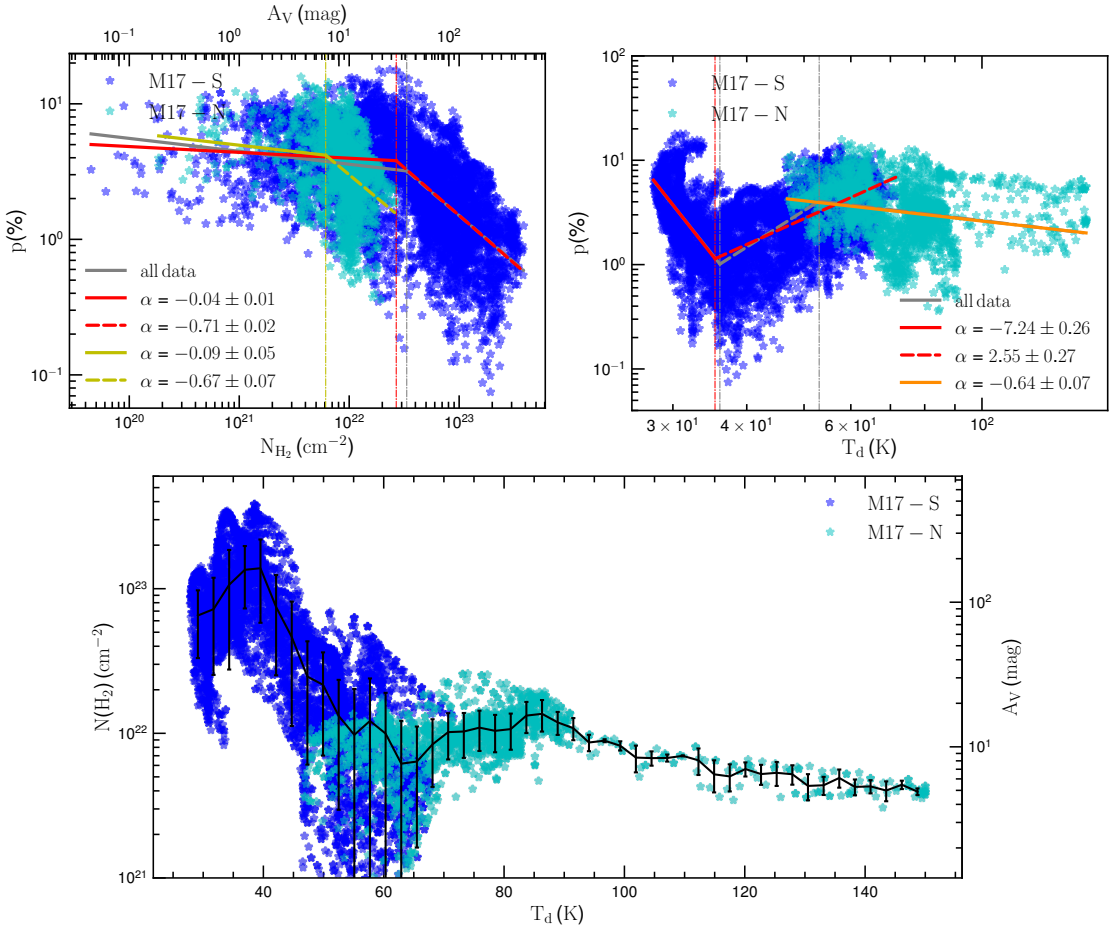

Figure 4.8: Top left: Relationship between polarization percentage and gas column density. Top right: Relationship between polarization percentage and dust temperature. In both panels, α denotes the index of the best-fit power-law model. The SOFIA/HAWC+ polarization data were smoothed to match the 14″ angular resolution of the SCUBA-2 850 μm map, which, together with *Herschel* data, was used to derive the $N(\mathrm{H_2})$ and T_d maps. Bottom: Variation of gas column density $N(\mathrm{H_2})$ as a function of dust temperature T_d.

4.3.3. Implications for Grain Alignment and Rotational Disruption by RATs

In this section, I discuss the implications of the observed polarization fraction in M17 for the physics of grain alignment and rotational disruption driven by radiative torques.

According to the RAT-A theory [55], the polarization percentage of thermal dust emission increases as the minimum aligned grain size, a_align, decreases. The alignment size a_align is determined by the competition between rotational acceleration by radiative torques and damping by gas collisions. This balance depends on the local gas density and dust temperature (which traces the radiation field), with the theoretical dependence given by $a_\mathrm{align} \propto n_\mathrm{H}^{2/7} T_\mathrm{d}^{-12/7}$ [202]. Therefore, in regions with higher gas density or lower dust temperature, a_align increases, leading to a lower polarization fraction due to fewer grains being efficiently aligned (see also [96] for details). This prediction from RAT-A theory explains the observed decrease in polarization percentage with increasing gas column density in the M17-S region (Figure 4.8, left panel). However, the same theory cannot account for the decline in P with increasing T_d in the M17-N region, where gas density remains relatively constant (Figure 4.8, right panel).

This discrepancy provides observational evidence for RAT-D.

The polarization fraction at far-IR and submillimeter wavelengths is highly sensitive to the maximum size of the dust grain size distribution, as larger grains dominate the emission at these wavelengths. According to the RAT-D mechanism [97], grains above a certain size can be rotationally disrupted when exposed to strong radiation fields. The disruption threshold, defined by the maximum grain size $a_{\rm disr}$, which depends on the local dust temperature (or equivalent with the radiation field), gas volume density, and the tensile strength of the grains, $S_{\rm max}$. This threshold follows the scaling relation $a_{\rm disr} \propto n_{\rm H}^{1/2} T_{\rm d}^{-3} S_{\rm max}^{1/4}$ [202]. Assuming a typical hydrogen volume density of $n_{\rm H_2} \simeq 3 \times 10^4$ cm^{-3} (see Table 3.3) and a dust temperature of $T_{\rm d} \simeq 53$ K, corresponding to the turning point in Figure 4.8, the estimated disruption sizes are $a_{\rm disr} = 0.16$, 0.28, and 0.49 μm for tensile strengths of $S_{\rm max} = 10^7$, 10^8, and 10^9 erg cm^{-3}, respectively (assuming a radiation field with a mean wavelength of 1 μm). As predicted by RAT-D, the disruption size decreases with increasing dust temperature, leading to a narrower population of aligned large grains and thus a decline in polarization fraction. This mechanism successfully reproduces the decreasing trend of P with $T_{\rm d}$ observed in M17-N.

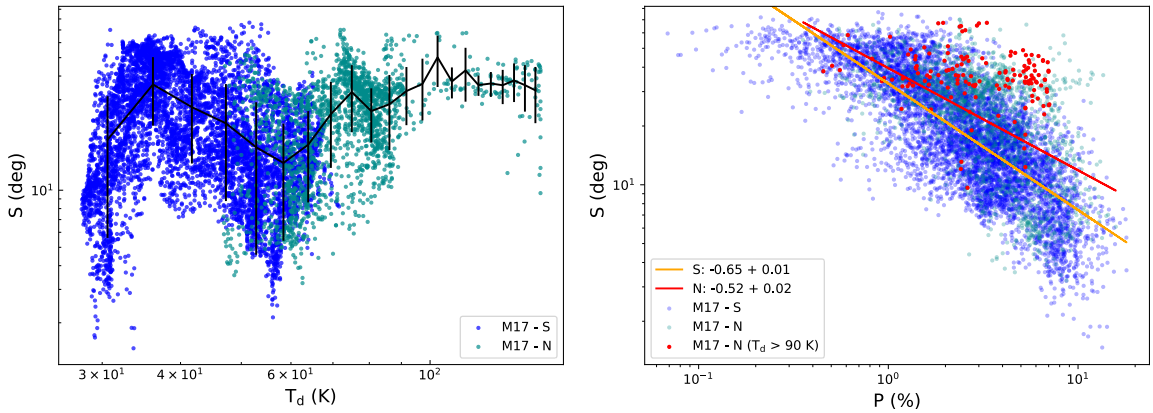

Figure 4.9: Left: Relationship between the polarization angle dispersion function, $\mathcal{S}$, and dust temperature, $T_{\rm d}$. The black curve represents the binned mean and standard deviation. Right: Relationship between $\mathcal{S}$ and polarization fraction, P. Red points indicate pixels with $T_{\rm d} > 90$ K. The orange and red lines show power-law fits for the M17-N and M17-S regions, respectively.

To investigate the role of small-scale magnetic field tangling in depolarization, I use the polarization angle dispersion function, S (see Section 2.3.5). Here, $\mathcal{S}$ is computed with $\delta = 27.2''$, which is approximately two beam sizes. As shown in the left panel of Figure 4.9, $\mathcal{S}$ is strongly correlated with $T_{\rm d}$ over most of the data, except for the hottest pixels in M17-N with $T_{\rm d} > 90$ K. This implies that the decrease in P at $T_{\rm d} > 90$ K (upper right panel of Figure 4.8) cannot be mainly explained by field tangling, and is more consistent with the RAT-D effect. The right panel of Figure 4.9 further shows an overall anti-correlation between $\mathcal{S}$ and P, again with the exception of the hottest pixels (red dots). In M17-S, pixels with $T_{\rm d} < 35$ K (dark blue dots in Figures 4.8 and 4.9) show a rapid decline in P, which can be attributed to stronger magnetic field tangling in the dense region (see the bottom panel of Figure 4.8). At intermediate temperatures of 35–65 K, both M17-N and M17-S show lower $N(\rm H_2)$ and $\mathcal{S}$, while P increases. This supports the idea that magnetic field tangling makes an important contribution to depolarization in the low-temperature regime.

4.4. Grain Alignment and Evolution in G11.11-0.12

In this section, I analyze the polarization fraction to investigate grain alignment physics and dust grain properties in G11.

4.4.1. Maps of Gas Density and Dust Temperature

Gas densities and dust temperatures are the key parameters governing grain alignment under RATs. For this analysis, I adopt the hydrogen column density and dust temperature produced by [17] based on modified blackbody fitting to *Herschel* observations in the 160, 250, 350, and 500 μm bands. Figure 3.17 presents the resulting maps: the left panel shows the gas column density, while the right panel displays the dust temperature distribution. The dust temperature decreases from $T_{\rm d} > 20$ K in the diffuse region to $T_{\rm d} \lesssim 15$ K close to the filament's spine. This temperature gradient indicates that dust heating is primarily due to the interstellar radiation field. The influence of local radiation from the two protostellar candidates, P1 and P6, appears to be minimal in comparison.

4.4.2. Polarization Fraction Map

Figure 4.10 shows the magnetic field orientation map, similar to Figure 3.14, but with segment lengths scaled by the polarization fraction P. For further analysis, I divide the filament into three sub-regions, North, Center, and South, outlined by the red rectangles in Figure 4.10. It is worth noting that the newly defined Center region differs slightly from the circular center region shown in Figure 3.14, which overlaps with the area observed by JCMT/SCUPOL. The map reveals that the polarization fraction is higher in the diffuse regions and drops significantly near the spine, where the thermal emission intensity is strongest.

Figure 4.11 presents histograms of the polarization fraction for the three sub-regions. While the mean polarization fraction in all regions is approximately 10%, a significant number of pixels exhibit high polarization values exceeding 20%. Among the three, the Center region shows a slightly higher polarization fraction on average compared to the North and South regions.

4.4.3. Polarization Fraction versus Total Intensity

Figure 4.12 shows the relationship between polarization fraction P and total intensity I. In the outer regions of the filament, where $I < 8$ mJy arcsec^{-2}, the polarization fraction is relatively high, ranging from approximately 10% to 30%. However, P decreases systematically with increasing intensity toward the filament's spine. This trend is well described by a power-law of the form $P \propto I^{-\alpha}$, with best-fit indices of $\alpha = 0.93 \pm 0.02$, 0.81 ± 0.02, and 0.80 ± 0.02 for the North, Center, and South regions, respectively. The uncertainties represent statistical errors from the fitting process.

In this study, I find that the Center and South regions exhibit slightly shallower slopes ($\alpha \sim 0.8$) compared to the North ($\alpha \sim 0.93$), suggesting that grain alignment is more efficient in the Center and South. Notably, the presence of two massive star candidates, P1 and P6, in these regions may contribute additional radiation that enhances grain alignment, thereby producing the observed shallower slopes [96]. Since $\alpha < 1$ in all three sub-regions, this suggests that grain alignment is not entirely lost even in the filament's dense interior. The implications of these slopes, along with supporting evidence for grain growth in the filament, are discussed further in Section 4.4.8.3.

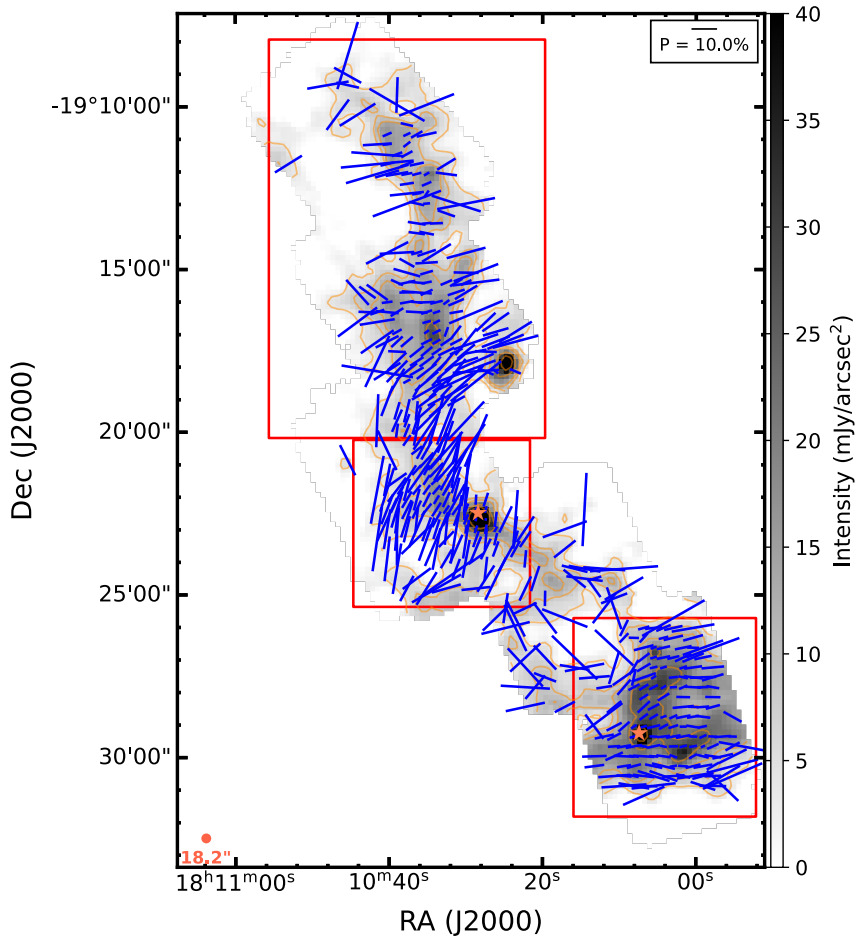

Figure 4.10: As in Figure 3.14, but with polarization vector lengths scaled to the polarization fraction. The North, Center, and South regions discussed in the text are indicated by the three red rectangles.

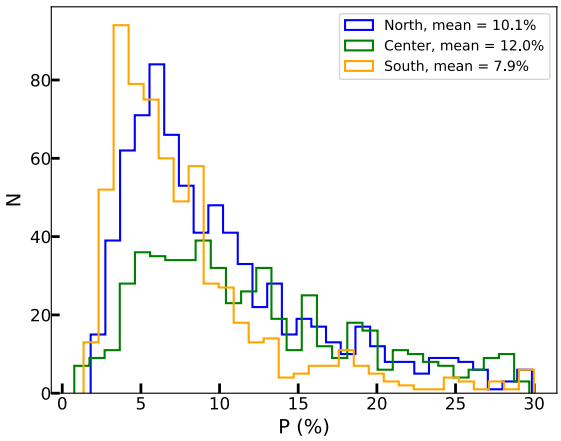

Figure 4.11: Distributions of the polarization fraction for the three sub-regions of the G11 filament: North (blue), Center (green), and South (orange)

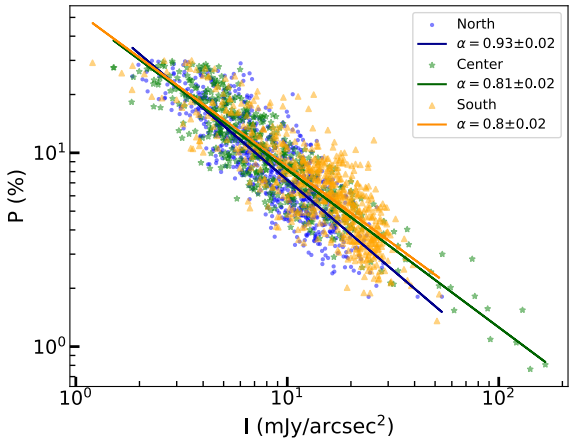

Figure 4.12: Dependence of polarization fraction, $P(\%)$, on total intensity, I observed by SOFIA/HAWC+ for the North (blue), Center (green), and South (orange) regions. Solid lines represent power-law fits to the data. The slope for the North region is steeper than those for the Center and South, indicating a stronger decrease in polarization fraction with increasing intensity.

4.4.4. Polarization Fraction versus Column Density and Dust Temperature

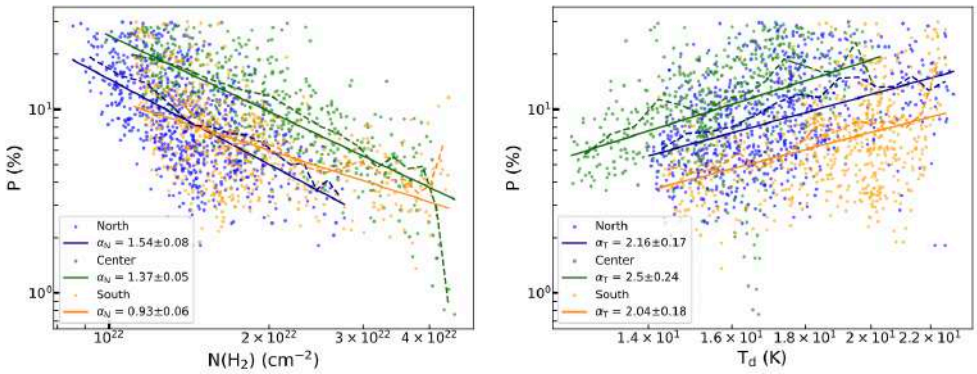

Figure 4.13: Dependence of polarization fraction, $P(\%)$, on column densities, $N(\mathrm{H_2})$ (left) and dust temperatures, T_d (right). Solid lines show power-law fits to the data (see text for details). Dashed lines indicate binned mean values, with bin sizes of 1.3×10^{21} cm^{-2} for $N(\mathrm{H_2})$ and 0.6 K for T_d.

According to the RAT theory [96], the efficiency of grain alignment is sensitive to local environmental conditions, particularly the strength of the radiation field and gas density. To investigate how these factors influence dust polarization in G11, I present in Figure 4.13 the dependence of polarization fraction P on column density (left panel) and dust temperature (right panel).

A clear anti-correlation is found in the $P - N(\mathrm{H_2})$ relation, and it is well represented by a power-law function, $P \propto N(\mathrm{H_2})^{-\alpha_\mathrm{N}}$. The derived values of the slope are $\alpha_\mathrm{N} = 1.54 \pm 0.08$ in the North, $\alpha_\mathrm{N} = 1.37 \pm 0.05$ in the Center, and $\alpha_\mathrm{N} = 0.93 \pm 0.06$ in the South. Similar to the P–I relation, the steeper slope in the North suggests a more significant decline in alignment

efficiency with increasing column density, whereas the shallower slopes in the Center and South regions point to more alignment of dust grains. This difference likely reflects the influence of two massive star candidates, P1 and P6, which may enhance local radiation and support grain alignment in the Center and South.

The P–$T_{\rm d}$ relation shows a positive correlation between polarization fraction and dust temperature, which serves as a proxy for the local radiation field strength. Fitting the relation with a power-law model, $P \propto T_{\rm d}^{\alpha_{\rm T}}$, yields slopes of $\alpha_{\rm T} = 2.16 \pm 0.17$ for North, 2.50 ± 0.24 for Center, and 2.04 ± 0.18 for South. These results suggest that stronger radiation fields, corresponding to higher dust temperatures, enhance grain alignment efficiency in all three regions. A more detailed discussion on the implications of these trends for grain alignment physics is provided in Section 4.4.6.

4.4.5. Magnetic Field Tangling

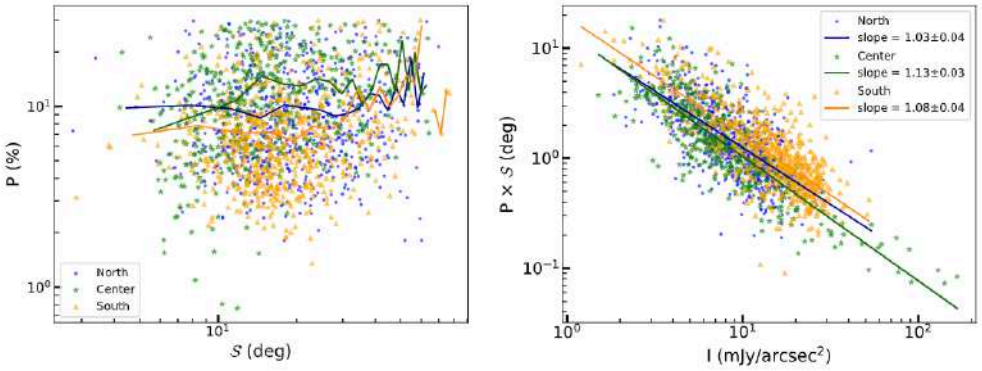

Figure 4.14: Left: Dependence of polarization fraction P (%) on the polarization angle dispersion function, $\mathcal{S}$. Solid curves represent the running mean. Right: Variation of $P \times \mathcal{S}$ as a function of total intensity I. Dashed curves show the running mean, while solid lines indicate power-law fits to the data (see text for details).

In addition to grain alignment and dust grain properties, the polarization fraction P is also influenced by the magnetic field geometry along the line of sight. To disentangle the relative contributions of magnetic field tangling and grain alignment to the observed dust polarization, I analyze the polarization angle dispersion function, $\mathcal{S}$, along with the product $P \times \mathcal{S}$. The quantity $P \times \mathcal{S}$ serves as a proxy for the average grain alignment efficiency along the line of sight [67]. This interpretation stems from the fact that, under constant alignment efficiency, variations in $\mathcal{S}$ reflect changes in magnetic field coherence: larger $\mathcal{S}$ values indicate stronger field tangling, leading to lower polarization fractions, and vice versa. Therefore, $P \times \mathcal{S}$ can be used to isolate the alignment contribution from the geometric depolarization effect and would provide us with information about the overall grain alignment.

I computed $\mathcal{S}$ following the method described in Section 3.3 of [67]. Figure 4.14 (left) displays the relationship between P and $\mathcal{S}$ across the three sub-regions. The solid lines represent running means. Although the individual data points show considerable scatter, no strong correlation is observed between P and $\mathcal{S}$. However, Figure 4.14 (right) shows the dependence of $P \times \mathcal{S}$ on total intensity I. A clear and steep decline is evident, indicating that the observed alignment efficiency decreases with increasing intensity. This trend suggests that magnetic field tangling is not the primary driver of depolarization in G11. Instead, the dominant effect appears to be a reduction in grain alignment efficiency toward regions of higher intensity.

4.4.6. Grain Alignment Mechanisms

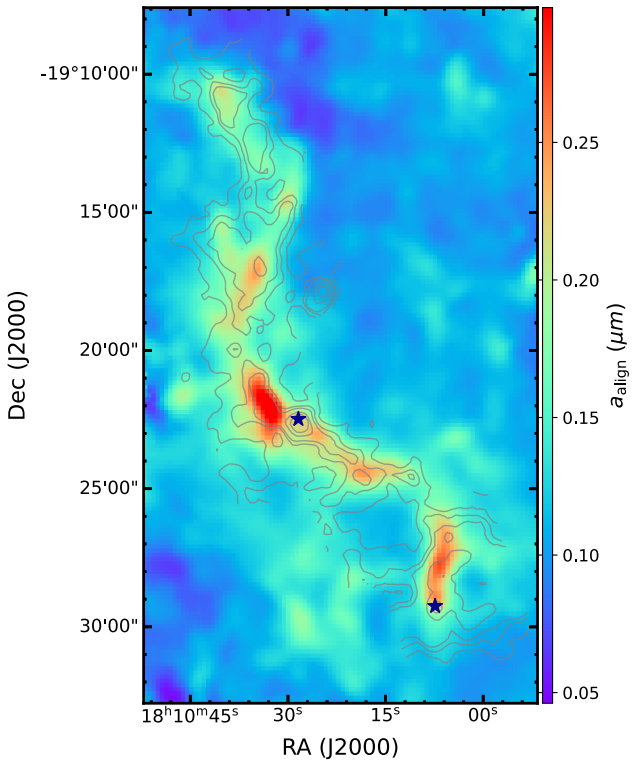

Figure 4.15: Map of the alignment size, $a_{\rm align}$, calculated within the framework of RATs, $a_{\rm align}$. The alignment size increases from the outer, more diffuse regions toward the denser inner spine of the filament

To interpret the observed polarization fraction and the results discussed in the previous section, I adopt the modern framework of grain alignment theory.

According to the RAT mechanism, efficient grain alignment occurs when dust grains achieve suprathermal rotation, i.e., their angular velocity significantly exceeds the thermal value [56, 85]. The minimum size of grain capable of alignment, hereafter referred to as the alignment size, can be estimated using the analytical expression derived in [96]:

$$a_{\rm align} \simeq 0.055\hat{\rho}^{-1/7}\left(\frac{\gamma\mathcal{U}}{0.1}\right)^{-2/7}\left(\frac{n_{\rm H}}{10^3\,{\rm cm}^{-3}}\right)^{2/7} \times\left(\frac{T_{\rm gas}}{10\,{\rm K}}\right)^{2/7}\left(\frac{\bar{\lambda}}{1.2\,\mu{\rm m}}\right)^{4/7}(1+F_{\rm IR})^{2/7}, \tag{4.1}$$

where $\hat{\rho} = \rho_{\rm d}/(3\,{\rm g\,cm}^{-3})$ with $\rho_{\rm d}$ is the dust mass density, γ is the anisotropy degree of the radiation field, $\mathcal{U}$ is the strength of the radiation field, and $\bar{\lambda}$ is the mean wavelength. $n_{\rm H}$ is the number density of hydrogen atoms, $T_{\rm gas}$ is the gas temperature, and $F_{\rm IR}$ quantifies the relative contribution of infrared damping compared to gas collisions. As shown in Equation 4.1, the alignment size increases in denser regions but decreases in environments with stronger radiation fields or high dust temperatures.

In the framework of the RAT theory, the observed dust polarization fraction depends on the population of aligned grains, which ranges in size from the minimum alignment threshold,

$a_{\rm align}$, to the upper limit of the grain size distribution, $a_{\rm max}$ [196, 100]. The value of $a_{\rm max}$ is determined by processes such as grain growth and fragmentation. For a fixed $a_{\rm max}$, an increase in $a_{\rm align}$ narrows the range of aligned grain sizes, leading to a reduced polarization fraction, P. Conversely, a smaller $a_{\rm align}$ allows a broader distribution of aligned grains, which results in a higher P [see 99].

To estimate the alignment size across G11, I adopt a local radiation anisotropy of $\gamma = 0.1$, a mean wavelength $\bar{\lambda} = 1.2\,\mu$m, and assume thermal equilibrium between gas and dust ($T_{\rm gas} = T_{\rm d}$), which is appropriate for cold, dense environments. The choice of $\gamma = 0.1$ is consistent with typical values for the diffuse interstellar radiation field [95, 209], and is justified by the lack of any nearby bright stars, implying that dust heating in G11 is dominated by the ambient ISRF. For this calculation, I use the maps of $T_{\rm d}$ and $n_{\rm H} = 2n(\rm H_2)$ shown in Figure 3.17. The radiation field strength, U, is derived from the dust temperature using the heating–cooling balance for silicate grains in the 0.01–1 μm size range, under the approximation $U \approx (T_{\rm d}/16.4\,{\rm K})^6$ for $U < 10^4$ (corresponding to $T_{\rm d} \lesssim 75\,{\rm K}$) [2].

The resulting alignment size map is presented in Figure 4.15. As expected, $a_{\rm align}$ increases from the more diffuse outskirts toward the dense spine of the filament, reflecting both the rise in gas density and the decline in dust temperature (see Figure 3.17). When compared to the polarization fraction map (Figure 4.10), an overall anti-correlation between $a_{\rm align}$ and P becomes apparent, consistent with theoretical predictions.

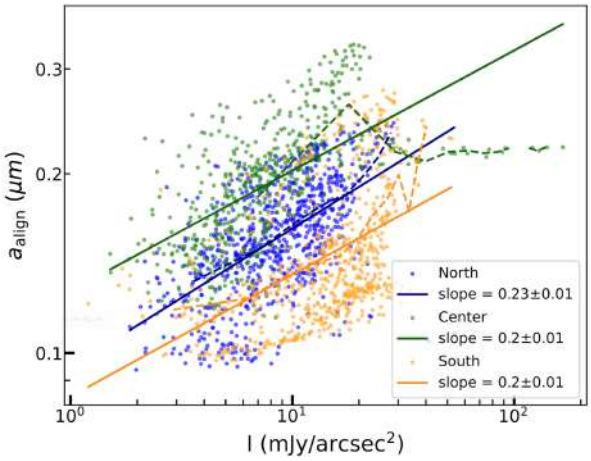

Figure 4.16: Variation of the alignment size, $a_{\rm align}$, with intensity, I. The dashed lines indicate the running mean values, while the solid curves represent power-law fits for the three regions.

To further examine the relationship between the polarization fraction and the alignment size, I plot the variation of $a_{\rm align}$ as a function of intensity, I, in Figure 4.16. The results show that $a_{\rm align}$ increases with increasing intensity, with the Center and South regions exhibiting slightly shallower slopes compared to the North.

Figure 4.17 presents the variation of the polarization fraction P (left panel) and the product $P \times \mathcal{S}$ (right panel) as a function of the alignment size $a_{\rm align}$. Both panels clearly show that polarization and alignment efficiency decrease as $a_{\rm align}$ increases. This trend is consistent with predictions from numerical modeling, which show that a larger $a_{\rm align}$ reduces the fraction of grains that are aligned, thereby lowering the observed polarization fraction [100, 96]. Thus, the depolarization in G11 is likely driven by a decrease in RAT alignment efficiency in regions characterized by high column density and low dust temperature.

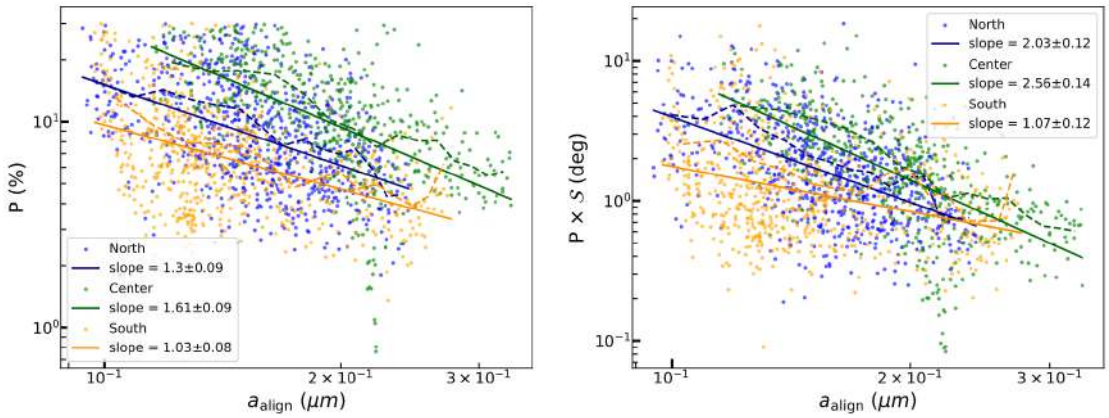

Figure 4.17: Variation of the polarization fraction (left) and the alignment efficiency, $P \times S$ (right), as a function of the alignment size, $a_{\rm align}$. The dashed lines represent running mean values, while the solid lines show power-law fits to the data (see text for details).

4.4.7. Magnetic Relaxation

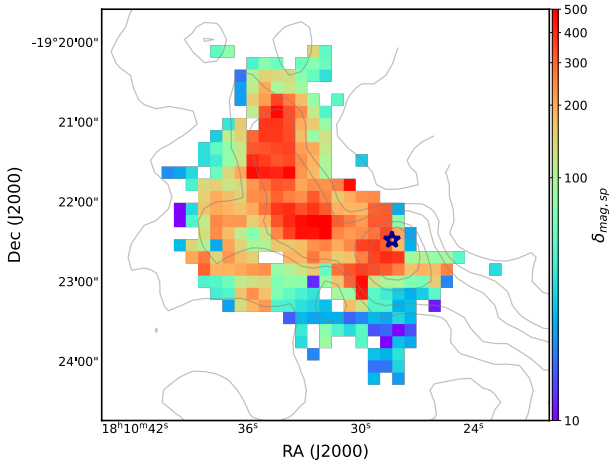

Figure 4.18: Map of the magnetic relaxation parameter, $\delta_{\rm mag,sp}$, for the central region of G11. The value of $\delta_{\rm mag,sp}$ increases from the outer layers toward the filament's spine and exceeds ~10 in the innermost areas. The star marker indicates the location of the protostellar source P1.

The magnetic properties of dust grains play a critical role in their interaction with ambient magnetic fields and their ability to align. To assess the role of magnetic relaxation in supporting grain alignment within this filament, I compute spatially resolved values of $\delta_{\rm mag,sp}$ (see Equation 1.38) using the available maps of hydrogen number density $n_{\rm H}$, magnetic field strength $B_{\rm tot}$, and dust temperature $T_{\rm d}$, based on Equation (1.38). For this calculation, I adopt representative parameters of $N_{\rm cl} = 100$ and $\phi_{\rm sp} = 0.01$, which corresponds to approximately 3% of the total iron abundance existing in the form of magnetic inclusions [85]. The resulting map is shown in Figure 4.18. Even with these modest assumptions for magnetic inclusions, $\delta_{\rm mag,sp}$ reaches values $\gtrsim$ 10 across the entire filament. This suggests that magnetic relaxation is highly efficient throughout the region and supports the possibility of perfect grain alignment via the MRAT mechanism [90].

It is worth noting that although $\delta_{\rm mag,sp}$ increases toward the filament's spine (see Figure 4.18), this does not necessarily lead to an increase in the observed polarization fraction. An increase in the polarization degree is not necessarily expected, as a result of the saturation of MRAT alignment efficiency and the growth of the minimum alignment size, $a_{\rm align}$ (see the previous subsection).

4.4.8. Discussions

4.4.8.1. Polarization Hole and RAT Alignment

G11, lacking bright internal sources, serves as an excellent laboratory for testing RAT alignment because the dominant source of radiation for grain heating and alignment is the diffuse interstellar radiation field [96]. In this study, I find that the polarization fraction follows a power-law relation with intensity, $P \propto I^{-\alpha}$, with $\alpha \sim 0.8$–0.9. This slope is notably steeper than those reported in other filaments, such as DR21 observed with JCMT/POL-2 ($\alpha \sim 0.3$; [193]) and Serpens South observed with SOFIA/HAWC+ ($\alpha \sim 0.5$; [46]). The steep slope in G11 indicates that grain alignment is only efficient in the outer region and becomes significantly less effective in the inner region.

As shown in Section 4.4.5, the contribution of magnetic field tangling to the observed depolarization in this dense filament is minor; the effect must instead be attributed primarily to variations in grain alignment efficiency. To investigate the role of grain alignment in producing the polarization-hole effect, I computed the minimum grain size required for alignment via RATs, $a_{\rm align}$, based on local gas density and radiation field (inferred from dust temperature), following the RAT framework outlined by [96]. This analysis revealed a strong correlation between $a_{\rm align}$ and total intensity (Figure 4.16), as well as a clear anti-correlation between $a_{\rm align}$ and both the polarization degree, P, and the alignment efficiency proxy, $P \times \mathcal{S}$ (Figure 4.17). These results suggest that the reduced population of aligned grains in the filament's spine, reflected in the larger $a_{\rm align}$, is the main driver of the polarization-hole feature, in agreement with RAT predictions [96].

4.4.8.2. Role of Magnetic Relaxation on RAT Alignment

Observations reveal that the polarization fraction in the outer layers of the G11 filament reaches high values, ranging from 20% to 30% (see Figures 4.11 and 4.12). These values exceed the typical interstellar polarization level of $P \sim 15\%$ reported by [67], and are consistent with those observed in other massive filaments such as DR21 [193] and G34.43 [122]. Modeling efforts based on *Planck* data suggest that such high polarization fractions require a high degree of grain alignment [207, 210]. This implies that, in the outer regions of dense filaments, near-perfect alignment of dust grains is necessary to reproduce the observed polarization levels. However, achieving perfect alignment through RATs alone is unlikely due to their sensitivity to several factors, including the angle between the magnetic field and radiation direction, grain composition [85, 211]. Enhanced magnetic relaxation, particularly from grains containing iron inclusions, has been proposed as a mechanism that can boost alignment efficiency beyond what RATs alone can provide [85, 90]. For the first time, I observationally assess the significance of magnetic relaxation and the MRAT mechanism in a filamentary cloud using magnetic field strength estimates derived from the DCF method. In G11, where the magnetic fields are relatively strong, I find that even modest iron inclusion levels ($N_{\rm cl} = 100$, $\phi_{\rm sp} = 0.01$) can result in magnetic relaxation timescales shorter than those for gas damping, yielding $\delta_{\rm mag,sp} > 10$ across the filament (see Figure 4.18). In

denser environments near the filament spine, grain-grain collisions may further enhance iron incorporation, increasing $\delta_{\rm mag,sp}$ and making perfect alignment more feasible. The much stronger magnetic relaxation, acting together with RATs, can lead to nearly perfect alignment of grains containing iron inclusions, which may explain the high polarization fractions observed in G11. A similar contribution from MRAT alignment has also been proposed for the Galactic Center by [212].

4.4.8.3. Implications for Grain Growth

Observational constraints on interstellar dust indicate that the typical upper limit of the grain size distribution in the diffuse ISM is approximately 0.25 μm, as described by the Mathis–Rumpl–Norsieck distribution [60] (see Equation 1.3.1.1). However, within dense molecular clouds, dust grains are expected to grow through coagulation and accretion processes. Dust polarization offers a valuable diagnostic for identifying such grain growth. For example, grain growth in dense regions has been evidenced by combining starlight polarization data with RAT numerical modeling [132].

In this work, I use the alignment size map (Figure 4.15) along with the polarization fraction map (Figure 4.10) to constrain lower limits on the maximum grain size, $a_{\rm max}$, necessary to account for the observed polarization slopes. In the outer parts of the filament, where the polarization fraction reaches high values (Figure 4.10), the minimum alignment size $a_{\rm align}$ ranges between 0.05 and 0.15 μm (Figure 4.15). To maintain such high levels of polarization, $a_{\rm max}$ must significantly exceed $a_{\rm align}$, which can be satisfied by the typical ISM value of $a_{\rm max} \sim 0.25\,\mu$m. In the inner filament, where densities peak, I find polarization fraction slopes of α ~0.8–0.9 (Figure 4.12), which are shallower than the $\alpha = 1$ case corresponding to a complete loss of alignment. This indicates that even in the densest parts of the filament, some grains remain aligned and contribute to polarized emission. For this to occur, $a_{\rm max}$ must be larger than the local $a_{\rm align}$, which reaches up to ~0.30 μm in the filament spine (Figure 4.15). Therefore, the condition $a_{\rm max} > a_{\rm align} \sim 0.30\,\mu$m must be satisfied, implying that grain growth is indeed occurring in G11. This finding suggests that dust grains in G11 have undergone growth in a moderately dense environment with hydrogen number densities around 10^4 cm^{-3} (see Figure 3.17, left panel), consistent with theoretical expectations for grain evolution in molecular clouds.

4.5. Conclusions

In this chapter, I examined thermal dust emission and polarization in LkHα 101, M17, and G11.11 −0.12 using polarization data from JCMT and SOFIA. The goal was to investigate how grain alignment and evolution respond to different physical conditions. The main findings are summarized below:

LkHα 101: JCMT/POL-2 dust polarization observations at 850 μm were analyzed.

1. The polarization fraction follows a power-law dependence on intensity with an index of $\alpha = 0.82 \pm 0.03$, which is within the typical range observed in molecular clouds. This result indicates that grain alignment occurs within the cloud, but with reduced efficiency. It aligns with the predictions of RAT alignment theory, suggesting that radiation from the B-type star LkHα 101 is sufficient to align grains even in relatively dense regions.

2. A significant drop in polarization fraction occurs near the B star, LkHα 101, which also corresponds to the region of highest density. This drop cannot be fully accounted for

by RAT alignment alone. However, it is consistent with the combined effects of grain alignment and rotational disruption. Additional mechanisms, such as magnetic field geometry influenced by turbulence, may also contribute to the observed polarization hole. Further investigation is needed to fully understand the origin of this feature.

M17: SOFIA/HAWC+ dust polarization observations at 154 μm were used.

1. The relationships between polarization fraction (P) and key physical parameters, total intensity (I), column density ($N(\mathrm{H_2})$), and dust temperature (T_d), were studied. The power-law index of the P–I relation is $\alpha = 0.51$, suggesting that grain alignment remains under the local radiation field. The observed decrease in polarization fraction with increasing column density in the M17-S region can be interpreted as the result of reduced alignment efficiency predicted by RAT-A theory, possibly coupled with magnetic field tangling effects.

2. The polarization angle dispersion function, $\mathcal{S}$, as a function of T_d and $N(\mathrm{H_2})$, was used to probe the role of magnetic field geometry. In the M17-N region, I found that the polarization fraction declines with increasing T_d even as both $N(\mathrm{H_2})$ and $\mathcal{S}$ decrease. This trend is most consistent with the combined effects of RAT-A and RAT-D, supporting the broader RAT paradigm.

G11.11 -0.12: SOFIA/HAWC+ dust polarization observations at 214 μm were analyzed.

1. The detailed analysis of the polarization fraction across the entire G11 filament was conducted to investigate grain alignment physics and dust properties. I found that the observed decrease in polarization fraction with increasing gas column density and total intensity can be explained by the growth of the minimum grain alignment size, a_align, toward the filament's center. An evaluation of alignment efficiency, taking into account the polarization angle dispersion function, suggests that magnetic field tangling is minimal and does not account for the observed depolarization near the spine.

2. Grain growth was constrained by using the slopes of the polarization degrees versus intensities and RAT alignment theory. In the outer regions, the maximum grain sizes, a_max, must exceed a_align $\sim$0.1 μm to maintain significant alignment. In the filament's bone, to reproduce the observed slope of $\alpha \sim 0.8$–0.9, a_max must be larger than the alignment sizes a_align $\sim$0.30 μm, indicating ongoing grain growth in dense regions.

3. Using magnetic field strengths derived from the DCF method (see Chapter 3), the role of magnetic relaxation in supporting RAT alignment was examined. The results show that grains can be perfectly aligned due to the combined effect of enhanced magnetic relaxation and RATs—referred to as the MRAT mechanism. This explains the high polarization fraction ($P \gtrsim 20\%$) observed in the outer regions of G11.

Together, these findings support the RAT paradigm while highlighting the significant influence of local conditions, such as radiation, dust temperature, gas density, and magnetic field structure, on the alignment and evolution of dust grains. The contrasting behaviors observed in the three regions emphasize the importance of combining polarization data with environmental conditions to gain an understanding of dust alignment physics.

Chapter 5

Numerical Modeling of Thermal Dust Polarization

The previous chapter analyzed far-IR and submillimeter polarization data from star-forming regions, providing observational evidence supporting the Radiative Alignment Torque (RAT) paradigm. However, a detailed forward modeling of thermal dust polarization based on the RAT paradigm and its comparison to the observational data are required to validate this theory. In this chapter, I apply numerical modeling to reproduce thermal dust polarization and compare the modeled results with the observed polarization percentage. I aim to bridge the gap between theory and observations by applying these models to star-forming regions. These models allow us to quantitatively test the predictions of RAT alignment and disruption mechanisms in specific molecular clouds, OMC-1 and Musca.

5.1. Introduction

Understanding dust polarization requires not only observations but also theoretical modeling to interpret the underlying physical processes. In this chapter, I present numerical modeling of thermal dust polarization using our developed DustPOL-py code [100]. This code incorporates both RAT-A and RAT-D mechanisms to simulate the alignment and disruption of dust grains under various physical conditions. The $P - T_{\rm d}$ (polarization percentage versus dust temperature) trend was reproduced [101, 202] for the OMC-1 and ρ Ophiuchus A molecular clouds, demonstrating the initial success of the joint effects of RAT-A and RAT-D. However, the influence of magnetic field fluctuations on polarization holes and the variation in the $P - T_{\rm d}$ trend has not yet been accounted for in previous tests of the RAT paradigm using polarization data (see [99] for a review). Therefore, it is crucial to consider the effects of magnetic field fluctuations to achieve a more comprehensive test of the RAT paradigm.

Filaments appear almost everywhere in interstellar clouds and form complicated networks, as shown by *Herschel*. They are believed to be an early stage of star formation, where the gas density and dust temperature can change a lot from one place to another inside the filaments (e.g., [11]). Because of this, filaments are good objects for testing the RAT paradigm. In this study, I have two main goals: (1) to test the RAT paradigm, and (2) to examine how magnetic field fluctuations affect the total thermal dust polarization produced by aligned dust grains in filaments. To do this, I use dust polarization observations of Musca from *Planck* and OMC-1 from SOFIA/HAWC+, and I compare them with synthetic polarization models made using our `DustPOL-py` code. These two filaments were chosen because they have different local conditions, such as gas density and radiation field, and because they may or may

not contain embedded protostars. Musca is a simple filament without embedded protostars, while Orion is the nearest high-mass star-forming region. Musca has low dust temperature and only a small amount of magnetic field tangling, so it is a good target for testing RAT-A. On the other hand, OMC-1 has a higher dust temperature, making it a good target for testing RAT-D. I use `DustPOL-py` to model the polarization data pixel by pixel, based on the main local physical parameters obtained from observations.

I introduce the numerical setup, including gas properties, radiation fields, and dust models. Then, I apply the model to each region, Musca and OMC-1, and compare the modeled polarization maps and trends with observations. Finally, I discuss the implications of these results for grain alignment physics.

5.2. Numerical Modeling

This section presents the numerical methodology used to model polarized thermal dust emission from aligned grains based on RAT paradigm. The objective is to test the validity of the RAT paradigm in two contrasting environments: Musca and OMC-1. The modeling is carried out using the `DustPOL-py` code[1], originally developed by [100, 101] to generate an "ideal" model of dust polarization, where the magnetic field is assumed to lie entirely in the plane of the sky and no field tangling or inclination effects are included. This idealized scenario provides a reference for the maximum polarization signal that can be achieved given perfect alignment conditions. To make the model more realistic, I then incorporate the effects of magnetic field inclination relative to the line of sight and fluctuations in field orientation along the line of sight. These depolarization mechanisms are added to the ideal model to produce a realistic polarization model and confront it with observational data.

The following subsections provide the main features of `DustPOL-py`, highlighting its key features and the physical input parameters required, including gas and dust properties, the local radiation field, and RAT-based alignment physics. I then present the key modeling outcomes and evaluate their consistency with observed data. Other polarization modeling approaches exist, such as inverse modeling [213, 214, 215] and parametric modeling [207, 210]. However, these two methods do not rely on fundamental physics and require multi-wavelength data to determine model parameters. As a result, they are not suitable for pixel-by-pixel modeling with single-wavelength data, which is the focus of this study.

5.2.1. Gas Properties and Radiation Fields

The number density ($n_{\rm H} = 2n_{\rm H_2}$) and gas temperature ($T_{\rm gas}$) are two key physical parameters in RAT theory, since they directly affect both the randomization of grain rotation and the alignment efficiency (see, e.g., [96]). In this study, these quantities are derived from observations and then used as input parameters for `DustPOL-py`.

In addition to gas properties, the characteristics of the local radiation field also play a crucial role. Specifically, the radiation strength U, which is often approximated by the dust temperature $T_{\rm d}$, and the anisotropy parameter γ are key determinants of alignment efficiency within the RAT framework [96]. The anisotropy degree γ varies between 0 and 1, where $\gamma = 1$ corresponds to a fully directional radiation field, such as that from a nearby stellar source, and $\gamma \approx 0.1$ characterizes more isotropic conditions typical of the diffuse ISM [88]. The mean wavelength of the radiation field, $\bar{\lambda}$, depends on specific regions.

[1] https://github.com/lengoctram/DustPOL-py

5.2.2. Grain Size Distribution

When accounting for the effects of RAT-D, the maximum grain size, $a_{\rm max}$, becomes a variable quantity that depends on the local gas density, radiation intensity, and the tensile strength of the dust grains, as described by Equation 1.40. The tensile strength reflects the grain's internal structure and plays a key role in determining the critical temperature at which grains are disrupted by centrifugal stress. For composite dust grains, typical values of tensile strength are on the order of $S_{\rm max} \approx 10^7\,{\rm erg\,cm^{-3}}$ [216].

5.2.3. Grain Alignment Function by RATs

According to the RAT-A theory, dust grains are first spun up to suprathermal rotational speeds by radiative torques before aligning with the local magnetic field direction [89, 56]. In grains that contain iron inclusions, making them superparamagnetic, the combined effect of enhanced magnetic relaxation and radiative torques can result in nearly perfect alignment with the magnetic field. This process is known as MRAT [85]. The minimum size for grain alignment, $a_{\rm align}$ (also called as critical alignment size), is defined by the threshold at which the grain's spin-up rate from RATs equals three times its thermal angular velocity, i.e., $\omega_{\rm RAT}(a_{\rm align}) = 3\omega_{\rm T}$ [56]. Using this criterion and the expression for $\omega_{\rm RAT}$ (Equation 1.36), the critical size $a_{\rm align}$ can be estimated as:

$$\begin{aligned} a_{\rm align} \;\simeq\; & 0.024\hat{\rho}^{-5/32}\gamma^{-5/16}\mathcal{U}^{-5/16}\left(\frac{10^3\,{\rm cm^{-3}}}{n_{\rm H}}\right)^{-5/16} \\ & \times\left(\frac{\bar{\lambda}}{0.5\;\mu{\rm m}}\right)^{17/32}\left(\frac{20\;{\rm K}}{T_{\rm gas}}\right)^{-5/16}\left(\frac{1}{1+F_{\rm IR}}\right)^{-5/16}\;\mu{\rm m}, \end{aligned} \tag{5.1}$$

where U is the radiation strength of the local radiation field [96].

The degree of grain alignment as a function of the grain size can be expressed using the following relation:

$$f_{\rm align} = f_{\rm max}\left[1-\exp\left(-a/2a_{\rm align}\right)^{-3}\right], \tag{5.2}$$

with $a_{\rm align}$ is defined by Equation 5.1, $f_{\rm max}$ describes the maximum degree of grain alignment, and the negligible alignment of small grains of $a \ll a_{\rm align}$ is disregarded [85].

Following MRAT, the maximum alignment efficiency, $f_{\rm max}$, depends on the ratio between the magnetic relaxation rate and the gas damping rate. This ratio is influenced by several factors, including grain size, magnetic susceptibility, and the surrounding gas density [85]. Numerical simulations have shown that grains containing embedded iron clusters can reach perfect alignment, corresponding to $f_{\rm max} = 1$. Supporting this, recent inverse modeling of Planck polarization data suggests that near-perfect alignment of large grains is necessary to reproduce observed polarization levels [210]. Based on these findings, this study adopts $f_{\rm max} = 1$, consistent with expectations for composite grains with internal iron inclusions under the MRAT mechanism.

5.2.4. Ideal Model of Thermal Dust Polarization with DustPOL-py

Dust grains are heated by starlight and then re-emit radiation at infrared wavelengths. Assuming that the dust population includes both carbonaceous and silicate components, the total thermal emission intensity can be calculated using the following expression:

$$\frac{I_{\rm em}(\lambda)}{N_{\rm H}} = \sum_{j=sil,cal} \int_{a_{\rm min}}^{a_{\rm max}} Q_{\rm abs} \pi a^2 \times \int dT B_\lambda(T_{\rm d}) \frac{dP}{dT} \frac{1}{n_{\rm H}} \frac{dn_j}{da} da, \tag{5.3}$$

where dP/dT is the temperature distribution function, $Q_{\rm abs}$ is the absorption efficiency, and $B_\lambda(T_{\rm d})$ is the Planck function. In this study, I neglect the minor effect of grain alignment on total emission intensity (cf. [201]).

When carbonaceous and silicate grains are treated as two separate populations, only silicate grains are expected to align with magnetic fields due to their paramagnetic properties. In contrast, carbonaceous grains, such as pure graphite, are typically diamagnetic and thus not efficiently aligned [85]. However, hydrogenated carbon grains may exhibit paramagnetic behavior because the presence of unpaired electrons allows them to interact with magnetic fields [217]. In the case of composite grains, where silicate and carbonaceous materials are mixed within a single grain, the entire grain can become magnetically responsive and can be aligned with magnetic fields. Observational evidence increasingly supports such composite grain models. For example, the Astrodust model [81] and the THEMIS model [82] both favor mixed compositions to explain observed interstellar dust properties. Based on this, I adopt the composite grain assumption throughout this study. Under this assumption, carbonaceous and silicate components share the same temperature.

To begin, I consider first the idealized model in which magnetic fields lie in the plane of the sky and the impact of magnetic field fluctuations is neglected. The polarized thermal emission from aligned dust grains is given by:

$$\frac{I_{\rm pol}(\lambda)}{N_{\rm H}} = \sum_{j=sil,cal} \int_{a_{\rm min}}^{a_{\rm max}} f_{\rm align}(a) Q_{\rm pol} \pi a^2 \times \int dT B_\lambda(T_{\rm d}) \frac{dP}{dT} \frac{1}{n_{\rm H}} \frac{dn_j}{da} da, \tag{5.4}$$

where $Q_{\rm pol}$ is the polarization efficiency [100].

The polarization degree (or polarization percentage) of thermal dust emission can be expressed as:

$$P_{\rm mod}^{\rm ideal}(\%) = 100\% \times \frac{I_{\rm pol}}{I_{\rm em}}, \tag{5.5}$$

where the subscript "mod" denotes quantities derived from the model, while the superscript "ideal" refers to the maximum polarization degree expected under ideal conditions—specifically, when magnetic fields lie entirely in the plane of the sky and no depolarization from field tangling is present.

5.2.5. Realistic Polarization Model: Accounting for Magnetic Field Tangling

In `DustPOL-py`, the magnetic field is assumed to lie entirely in the plane of the sky (POS), so the thermal dust polarization fraction can reach its maximum value, as described by Equation 5.5. In reality, however, the magnetic field may be inclined with respect to the line of

sight (LOS). This inclination, characterized by the angle ψ, reduces the observed polarization fraction because of projection effects. Additionally, variations in magnetic field fluctuations along the line of sight introduce further depolarization. This effect is captured by a correction factor, $F_{\rm turb}$, which accounts for magnetic field fluctuations. The parameter $F_{\rm turb}$ depends on the angle between the local magnetic field direction and the mean field orientation along the LOS. It is known to be anti-correlated with the polarization angle dispersion function $\mathcal{S}$ [201], meaning that regions with higher angular dispersion exhibit greater depolarization. Taking both projection and fluctuation effects into account, the modeled polarization degree under more realistic conditions is given by:

$$P_{\rm mod} = P_{\rm mod}^{\rm ideal} \sin^2\psi F_{\rm turb}. \tag{5.6}$$

Numerical simulations presented in [201], which combined MHD simulations and polarized radiative transfer using `POLARIS`, demonstrated that the polarization model defined by Equation 5.6 closely reproduces synthetic polarization results. Their study also showed that the depolarization factor $F_{\rm turb}$ decreases with increasing polarization angle dispersion, following the relation $F_{\rm turb} \propto \mathcal{S}^{-\eta_1}$, where the exponent η_1 depends on the magnetic field's inclination angle. Similarly, results from [105] revealed a correlation between the average magnetic field inclination and the polarization angle dispersion function. This relationship can be expressed as $\langle\sin^2\psi\rangle \propto \mathcal{S}^{-\eta_2}$, indicating that higher angular dispersion is associated with more inclined magnetic fields [see also 218]. In addition to line-of-sight fluctuations, small-scale magnetic field variations within the beam (i.e., the plane-of-sky tangling) can further reduce the observed polarization. This additional depolarization effect is quantified by a correction factor $F_{\rm beam}$ [201].

Accounting for all these depolarization effects, the net polarization degree from thermal dust emission can be expressed as:

$$P_{\rm mod} = \Phi P_{\rm mod}^{\rm ideal} \left(\frac{\mathcal{S}}{1^\circ}\right)^{-\eta}, \tag{5.7}$$

where Φ represents a coefficient that describes the depolarization due to the magnetic field's inclination angle. The parameter $\eta > 0$ is the power-law index describing the depolarization effect arising from magnetic field fluctuations along both the line of sight and the plane of the sky. This index is expected to vary depending on local environmental conditions. In practice, η is determined from the slope of the observed P–$\mathcal{S}$ relation. The value Φ is obtained by fitting the modeled polarization percentage to the maximum polarization observed in each filament. The best-fit values of Φ used in this study are listed in Table 5.1.

Table 5.1 provides a summary of the model parameters adopted for Musca and OMC-1. These include the hydrogen number density ($n_{\rm H}$), gas temperature ($T_{\rm gas}$), minimum and maximum grain sizes ($a_{\rm min}$, $a_{\rm max}$), and grain shape, characterized by an aspect ratio of 1:3 (minor to major axis). Also listed are the size distribution power-law index (β), the grain tensile strength ($S_{\rm max}$), the radiation field strength ($\mathcal{U}$), the mean wavelength of the radiation field ($\bar{\lambda}$), and the anisotropy parameter (γ).

In the following subsections, I present both the observational data and the corresponding modeling results for the Musca and OMC-1 filaments

5.3. Application to Musca

This section begins with a presentation of the observational data for Musca, followed by the modeling results. I then compare the modeled results with the observed data to assess the

Table 5.1: Model parameters

	Parameter	Musca	OMC-1
Anisotropic degree	γ	0.3	1
Mean wavelength	$\bar{\lambda}$ [μm]	1.2	0.3
Gas temperature	$T_{\rm gas}$ [K]	$T_{\rm dust}$	$T_{\rm dust}$/5000K
Grain composition	-	Sil+Car	Sil+Car
Dust mass density	ρ [g cm^{-3}]	3	3
Minimum grain size	$a_{\rm min}$ [μm]	10^{-3}	10^{-3}
Maximum grain size	$a_{\rm max}$ [μm]	0.25 – 0.5	0.2 – 2
Power-index	β	-3.5	-3.5
Maximum tensile strength	$S_{\rm max}$ [erg cm^{-3}]	10^7	10^7 – 10^8
magnetic field's inclination effect	Φ	0.53	0.28

agreement between theoretical predictions and actual measurements.

5.3.1. Observations

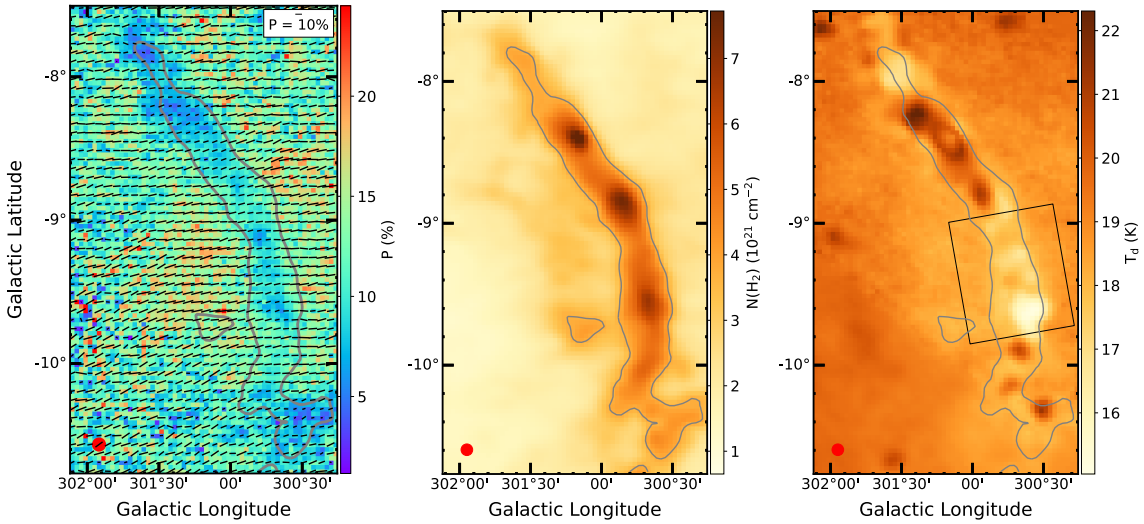

Figure 5.1: Musca observed by *Planck*. Left: Magnetic field orientation map, where the length of each line segment is proportional to the polarization percentage P. 10% reference scale is shown. Center: Column density map. Right: Dust temperature map. The red circle in the lower-left corner indicates the map resolution (FWHM) of 5′. Gray contours represent column densities of 3.7×10^{21} cm^{-2}. The black rectangle outlines the southern portion of the filament, which is the focus of the subsequent analysis.

To investigate the physical mechanisms behind dust grain alignment, polarization percentage is commonly analyzed in relation to total intensity. However, because total intensity depends on both column density and dust temperature, it can be difficult to isolate their individual effects on polarization. To address this, the present study examines the relationship between the polarization percentage P, gas column density $N(\mathrm{H}_2)$, and dust temperature $T_{\rm d}$.

In addition, I analyze the polarization angle dispersion function $\mathcal{S}$ to assess the influence of magnetic field tangling on the observed polarization.

First, I explore how P varies with physical parameters such as column density and dust temperature, in order to characterize the underlying grain alignment and potential disruption processes. Second, I examine the dependence of P on $\mathcal{S}$, which serves as a proxy for magnetic field disorder, to evaluate how magnetic field tangling contributes to depolarization.

Musca (Figure 5.1) is located at a distance of approximately 170 pc [134]. The filament is considered to be in an early stage of evolution and currently shows no signs of active star formation [135]. A candidate T Tauri star has been identified near the northern end of the filament in Galactic coordinates [136]. Musca is characterized as an isothermal filament in hydrostatic equilibrium that has already undergone fragmentation, suggesting that star formation may occur in the near future [137, 138].

Magnetic field orientations inferred from both starlight polarization [139] and thermal dust emission [140, 135] reveal that the local magnetic fields are predominantly perpendicular to the filament's spine. Analysis of *Herschel* data by [135] further showed that magnetic field lines tend to follow the low-column-density striations surrounding the filament, implying that Musca may be accreting interstellar material along these structures. More recently, SOFIA/HAWC+ observations at higher angular resolution have confirmed that the magnetic field orientation remains largely perpendicular to the spine, at least in the region covered by those observations [141].

In this study, I use the *Planck* polarization map of Musca at ~ 850 μm (353 GHz), which is the highest-frequency channel and the most sensitive one for measuring dust polarization [140]. The Stokes I, Q, and U maps have an angular resolution of $5'$, corresponding to a physical scale of about 0.24 pc. The pixel size is $112''$. Musca is one of the regions with high signal-to-noise ratio in the full-sky polarization data from *Planck* [140]. The left panel of Figure 5.1 presents the magnetic field orientation inferred from the *Planck* data, where the length of each line segment is proportional to the polarization fraction. This map was extracted from the public *Planck* archive and then reprojected into Galactic coordinates using the `reproject` package in the `astropy` Python library.

Figure 5.1 (center and right) presents the column density ($N(\mathrm{H_2})$) and dust temperature (T_d) maps derived from SED fitting performed by [77]. The column density map reveals a well-defined filamentary morphology with several substructures, where $N(\mathrm{H_2})$ increases from the outer regions toward the filament's spine. The dust temperature map shows a north–south gradient along the spine, with warmer temperatures ($\sim$21 K) in the north and cooler temperatures (below 17 K) in the south. However, I note that the dust temperatures inferred from *Planck* data can reach up to $\sim$22 K, is higher than that obtained by *Herschel* with a maximum T_d of $\sim$18 K. Moreover, [138] using *Herschel* data reported no evidence for a high-temperature core as suggested by the *Planck* temperature map (Figure 5.1, right panel). This discrepancy likely arises from the different wavelength coverage and spatial resolutions of the two instruments. *Planck* derives dust temperature from six broad-band channels spanning 20 to 3000 μm, with a representative resolution of $4'.9$ at 850 μm. In contrast, *Herschel* uses five channels from 70 to 500 μm, offering much finer spatial resolution, down to $36''$ at 500 μm. As a result, the two telescopes may probe different dust components, and *Planck*'s higher temperatures could partly reflect confusion between cold and warm components in the SED fitting (Lars Bonne, private communication). Since this study focuses on regions unaffected by embedded radiation sources, I restrict the analysis to the southern portion of the filament, outlined by the black rectangle in Figure 5.1 (right panel).

A detailed analysis of Musca using polarization data from *Planck* was carried out [140].

Their study revealed a clear depolarization effect along the filament, characterized by a significant drop in polarization fraction toward the filament's spine, as well as a general decline in polarization with increasing gas column density. To investigate the underlying causes of this depolarization, I analyze the filament's column density, dust temperature, and magnetic field tangling. Due to Musca's well-defined filamentary morphology, I examine the radial profiles of these physical quantities and assess how they relate to variations in polarization.

5.3.1.1. Gas Density Profile

To characterize the radial density structure of Musca, I fit its column density profile using a Plummer-like function with the `RadFil` Python package [185]. This method is applied to the column density map under the assumption that the filament lies in the POS. The Plummer-like profile is defined as follows [16, 135, 185]:

$$N(\mathrm{H_2})(r) = \frac{N(\mathrm{H_2})(0)}{[1 + (r/R_{\mathrm{flat}})^2]^{\frac{q-1}{2}}} \tag{5.8}$$

where $N(\mathrm{H_2})(0)$ is the peak column density, r is the radial distance from the filament's spine, q is the power-law density exponent, and R_{flat} is the radius of the inner, flat region of the density profile.

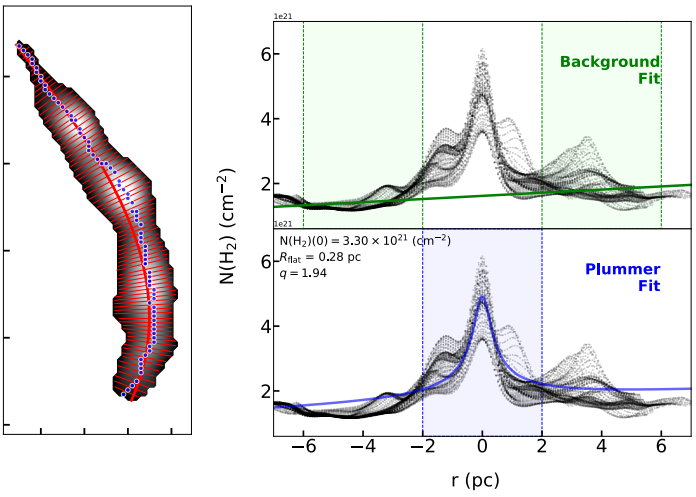

Figure 5.2: Musca. Left: Column density map used to construct the radial profile of the filament. Radial cuts (thin red lines) are sampled at intervals of 0.1 pc along the filament spine (thick red line), which is determined by `RadFil` using a B-spline smoothing algorithm and a user-defined mask [185]. Radial distance is defined as the projected distance from each pixel to the peak emission (marked by the blue dot) along its corresponding cut. Right: Radial profile fitting. The top panel shows the first-order polynomial background fit (green shaded region), while the bottom panel presents the Plummer-like profile fit (blue shaded region), both applied to the background-subtracted data.

The resulting spine from `RadFil` is shown as a thick red line overlaid on the grayscale column density map in Figure 5.2 (left). From this spine, `RadFil` generates a series of radial cuts (thin red lines) that are oriented perpendicular to the filament axis. These cuts yield individual radial profiles, which are displayed as black dotted lines in Figure 5.2 (right).

To estimate the background level, I fit and subtract a first-order polynomial from each radial profile. This background fitting is performed within a radial range of $2 < |r| < 6$ pc, indicated by the green-shaded region in the upper panel of Figure 5.2 (right). Finally, the background-subtracted radial profile is fitted with a Plummer-like function using `RadFil`. The resulting best-fit model is shown as a thick curve in the lower right panel of Figure 5.2.

From the best-fit model obtained using `RadFil`, I derive a power-law index of $q = 1.94$ and a flat inner radius of $R_{\rm flat} = 0.28$ pc. For comparison, a similar Plummer-like fit was applied to *Herschel* data, yielding $q = 2.2$ and $R_{\rm flat} = 0.08$ pc [135]. The larger value of $R_{\rm flat}$ found in this study is primarily due to the lower angular resolution of *Planck*, with a beam size of approximately $5'$ ($\sim$ 0.24 pc), compared to the much higher resolution of *Herschel* ($\sim 36''$, or $\sim$0.025 pc).

5.3.1.2. Filament Radial Profiles

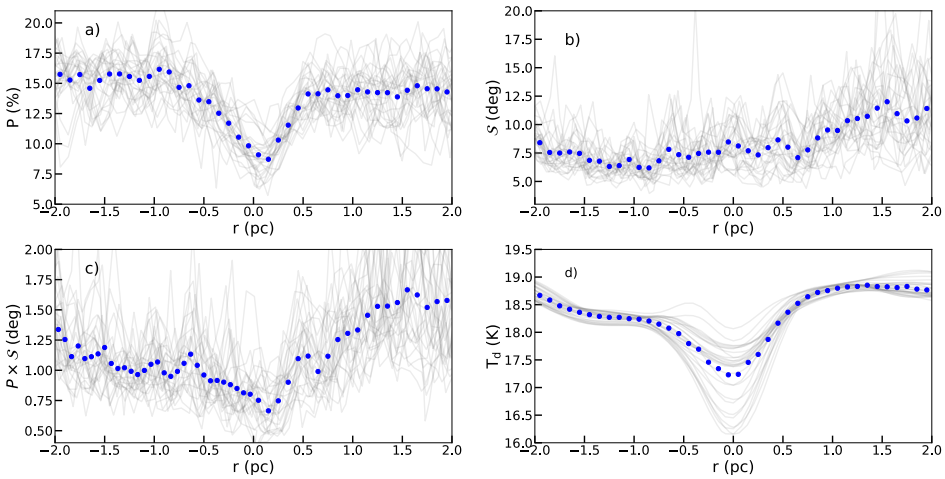

Figure 5.3: Musca. Variations of P, $\mathcal{S}$, $P \times \mathcal{S}$, and $T_{\rm d}$ as a function of the radial distance (r). These profiles were constructed using `RadFil` by sampling radial cuts at 0.01 pc intervals along the filament spine (see also Figure 5.2). Radial distance is defined as the projected offset from the spine, with negative and positive values corresponding to the left and right sides, respectively. Thin gray lines represent individual radial cuts, while filled dots denote mean values computed in bins of 0.1 pc.

Figure 5.3 presents the physical parameters across the Musca filament derived by `RadFil`, including polarization percentage (a), polarization angle dispersion function (b), grain alignment efficiency $P \times \mathcal{S}$ (c), and dust temperature (d).

Panel (a) shows that the polarization fraction reaches a minimum of approximately 8% at the filament's spine. Moving outward, P rises to around 15% at a distance of $\sim$0.7 pc before gradually decreasing to $\sim$10% further into the ISM. A similar trend was previously reported by [140] (see their Figure 10).

To investigate whether the observed depolarization near the spine is caused by magnetic field tangling, I examine the behavior of $\mathcal{S}$ and $P \times \mathcal{S}$ in panels (b) and (c), respectively. The values of $\mathcal{S}$ are generally low across the filament, with a mean below 10°. According to [140], such low values of $\mathcal{S}$ suggest that the depolarization is unlikely to be caused by magnetic field fluctuations, which would produce values closer to 52° in the case of random fields.

In addition to magnetic field tangling, the polarization percentage is influenced by environmental factors and alignment efficiency. By removing the effect of magnetic field disorder, $P \times \mathcal{S}$ provides the alignment efficiency of grains along the line of sight [67]. The radial profile of $P \times \mathcal{S}$ shows that alignment efficiency is lowest at the filament spine and increases toward the outer regions.

Panel (d) displays the dust temperature profile, which reveals an anti-correlation with column density (as shown in Figure 5.2). The central spine, characterized by the highest densities ($\sim 5 \times 10^{21}\,\mathrm{cm}^{-2}$), exhibits the lowest temperatures, typically below 18 K, with some regions reaching as low as 16 K. The dust temperature increases steadily from $\sim$ 17 K at the center to about 20 K in the outer areas.

From these filament profiles, we can see that the polarization fraction reaches its lowest value along the filament spine, where the dust temperature (or radiation field) is lowest, the density is highest, and the grain alignment efficiency is weakest. Toward the outer parts of the filament, the gas density decreases, while the dust temperature and alignment efficiency increase, leading to a corresponding rise in the polarization fraction.

5.3.2. Model Results

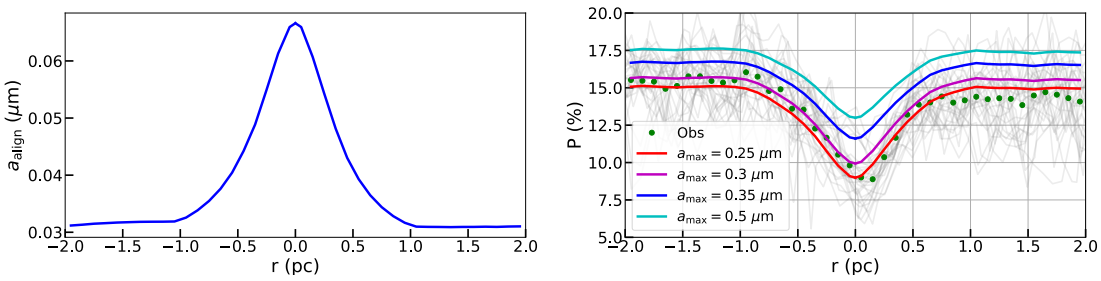

Figure 5.4: Musca. Upper panel: Minimum grain alignment size (a_{align}) computed from our RAT-based model for Musca. Lower panel: Comparison between model and observed polarization fractions. Gray curves represent P as a function of radial distance r for individual cuts across the filament, derived from observational data (see Section 5.3.1.2). Green dots indicate the mean observed polarization fraction in radial bins. Colored solid lines show the model predictions for different maximum grain sizes a_{max}. The sharp increase in alignment size toward the filament's center leads to a corresponding drop in the model polarization fraction, successfully reproducing the observed polarization hole.

In Musca, the filament exhibits a well-defined structure with relatively uniform physical conditions along its length. This allows for modeling the polarization fraction P as a function of radial distance r, i.e., the distance from the filament's spine toward its outer regions.

To simulate the variation in dust polarization with r, it is necessary to first characterize how the local gas volume density and dust temperature (which traces the radiation field) change with radial position. The dust temperature profile is adopted from the mean temperature map derived from *Planck* data (see Figure 5.3 d).

Within the filament, for regions with $|r| < 1$ pc, the gas number density is assumed to vary with radial distance r according to a Plummer-like profile (e.g., [16]),

$$n_{\mathrm{H_2}}(r) = \frac{n_{\mathrm{H_2}}(0)}{[1 + (r/R_{\mathrm{flat}})^2]^{p/2}}, \tag{5.9}$$

where $n_{\mathrm{H_2}}(0)$ represents the central number density of the filament at $r = 0$, given by

$$n_{\mathrm{H_2}}(0) = \frac{N(\mathrm{H_2})(0)}{A_{\mathrm{p}} R_{\mathrm{flat}}}, \tag{5.10}$$

where

$$A_{\mathrm{p}} = \frac{1}{\cos i} \int_{-\infty}^{\infty} \frac{du}{(1+u^2)^{p/2}}, \tag{5.11}$$

with i is the inclination angle of the filament relative to the POS, and I assumed $i = 0$. Following Plummer-like fitting as described in Section 5.3.1.2, I obtain $n_{\mathrm{H_2}}(0) \simeq 1300\,\mathrm{cm^{-3}}$.

For the outer regions of the filament ($|r| > 1$ pc), I adopt a constant gas number density of $n_{\mathrm{H_2}} = 100\ \mathrm{cm^{-3}}$ and a constant dust temperature of $T_{\mathrm{d}} = 18.3$ K, as inferred from the *Planck* temperature profile (Figure 5.3d).

The upper panel of Figure 5.4 illustrates the variation in the minimum grain alignment size, a_{align}, computed from the RAT alignment model for Musca. As the radial distance decreases toward the filament spine, a_{align} increases sharply. This behavior results from the combined effects of rising gas volume density and declining dust temperature (i.e., reduction of the local radiation field). For a given maximum grain size a_{max}, this increase in a_{align} leads to an increasing loss of grain alignment for grains smaller than a_{align} toward the filament's spine where is the dense and cold region.

The lower panel of Figure 5.4 presents a comparison between the modeled polarization profile, P_{mod} (computed using Equation 5.7), and observational data, for the case without RAT-D. Given that Musca exhibits relatively low dust temperatures (below 19 K) and moderate to high gas densities (10^2–$10^3\ \mathrm{cm^{-3}}$), conditions are not favorable for RAT-D. As such, models incorporating only the RAT-A mechanism are sufficient to reproduce the observed polarization trend. The effect of magnetic field tangling is also expected to be minimal in Musca. The polarization angle dispersion function, $\mathcal{S}$, remains low (typically $< 10°$) and shows little variation across the filament (Figure 5.3b). Furthermore, the weak correlation between P and $\mathcal{S}$, with a fitted power-law index of $\eta = 0.03$, suggests that magnetic field disorder does not significantly contribute to the observed depolarization.

The model predictions in Figure 5.4 explore a range of maximum grain sizes, from 0.25 to 0.5 μm. In this framework, dust grains are aligned within the size interval $a_{\mathrm{align}} < a < a_{\mathrm{max}}$; hence, increasing a_{max} leads to a greater number of aligned grains and a correspondingly higher polarization fraction. Furthermore, as a_{max} increases, the distribution of aligned grain sizes becomes broader, reducing the contrast in polarization fraction between the inner and outer regions of the filament. Our modeling shows that values of $a_{\mathrm{max}} = 0.25$–0.35 μm provide a good match to the observed sharp decline in polarization fraction toward the filament spine. This result supports the conclusion that the observed polarization hole in Musca is mainly caused by the loss of grain alignment due to increasing a_{align} in denser and colder regions, consistent with the predictions of the RAT alignment mechanism.

5.4. Application to OMC-1

This section begins with a presentation of the observational data for OMC-1, followed by the modeling results. I then compare the modeled polarization degree with the observed data.

5.4.1. Observations

Located at a distance of 388 ± 5 pc [142], the Orion Nebula is the closest known region of high-mass star formation [143]. The OMC-1, also referred to as Orion A, lies behind

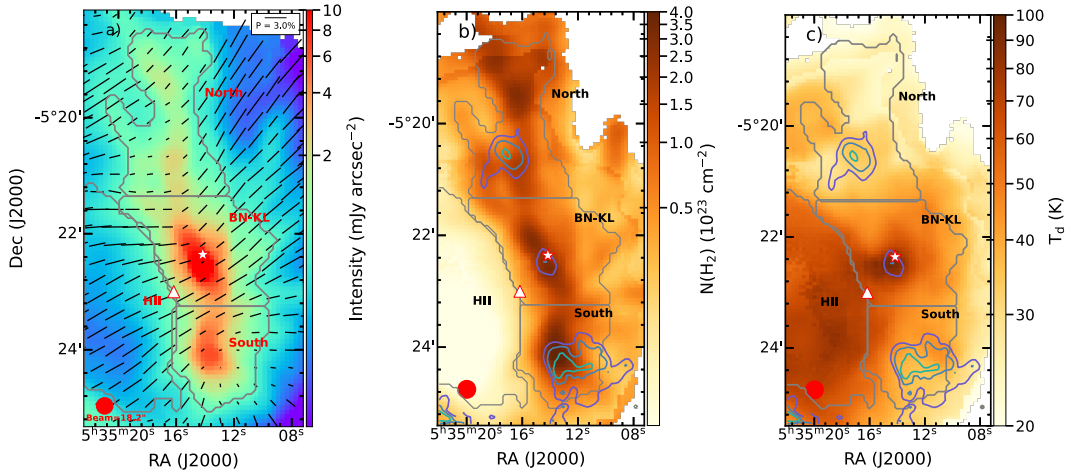

Figure 5.5: OMC-1. (a) Magnetic field orientation map observed at 214 μm with SOFIA/HAWC+. Black line segments represent the magnetic field orientation and are overlaid on the dust continuum intensity map. he vector spacing is equal to the beam size, shown by the solid red circle in the lower-left corner. The three subregions, North, BN–KL, and South, are marked. (b) Column density map. (c) Dust temperature map. The light green, dark blue, and violet contours correspond to polarization fractions of $P = 0.6\%$, 1.0%, and 1.4%, respectively. The star marks the BN/KL position, and the triangle indicates the location of the Trapezium cluster.

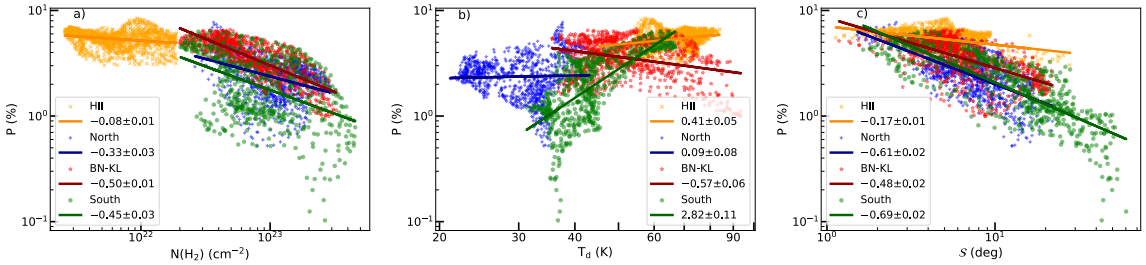

Figure 5.6: OMC-1. Variations of the polarization percentage P as a function of (a) column density $N(\mathrm{H_2})$, (b) dust temperature T_d, and (c) polarization angle dispersion function $\mathcal{S}$. Colored points represent different subregions: North (blue), BN–KL (red), South (green), and the H II region (orange). The solid lines show the best-fit power-law relations for each corresponding region.

an H II region that is ionized by the O- and B-type stars in the Trapezium cluster. OMC-1 consists of two prominent clumps: the Becklin-Neugebauer/Kleinmann-Low (BN/KL) region in the north [144, 145], and Orion South (Orion S) in the south [146]. The BN/KL region is notable for hosting a powerful explosive molecular outflow, characterized by a broad opening angle and multiple ejecta. Observations show that the magnetic fields in OMC-1 exhibit an hourglass morphology and strengths on the order of milligauss (e.g., [147, 148, 149]).

For this study, I use thermal dust polarization data toward Orion BN/KL obtained by SOFIA/HAWC+ at a wavelength of 214 μm, with an angular resolution of 18$''$.2. This dataset was first reported [148, 149], with a primary focus on analyzing the magnetic fields. A notable depolarization effect was also identified [148]. Evidence of RAT-D was later reported

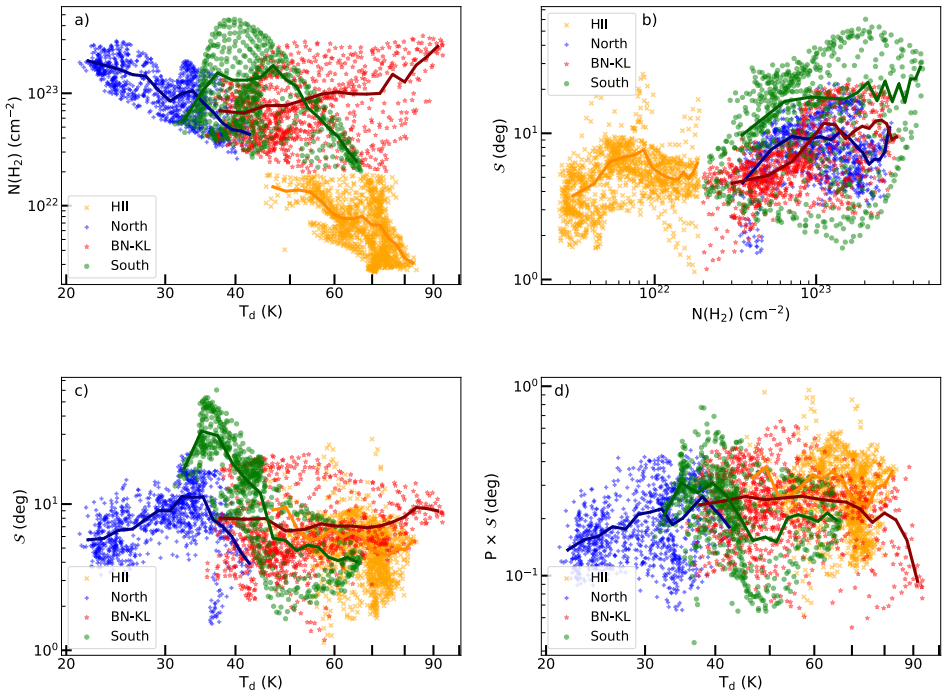

Figure 5.7: OMC-1. (a) Column density $N(\mathrm{H_2})$ as a function of dust temperature T_d; (b) polarization angle dispersion function $\mathcal{S}$ versus column density $N(\mathrm{H_2})$; (c) $\mathcal{S}$ versus dust temperature T_d; and (d) the product $P \times \mathcal{S}$ as a function of T_d. Colored points represent different subregions: North (blue), BN–KL (red), South (green), and the H II region (orange). Solid curves indicate the running mean values for each region.

in the BN/KL region [150] and in the Orion Bar [151]. In the present work, I use only the polarization measurements satisfying S/N(I) > 250 and S/N(P) > 3.

Figure 5.5 presents the magnetic field orientation map (a), column density map (b), and dust temperature map (c) for OMC-1. This analysis focuses on the OMC-1 filament and the H II region, both of which are encompassed by gray contours. The H II region is characterized by low column densities ($N(\mathrm{H_2}) < 2 \times 10^{22}$ cm^{-2}) and high dust temperatures ($T_\mathrm{d} > 45$ K). In contrast, the filament shows high column densities ($N(\mathrm{H_2}) > 2 \times 10^{22}$ cm^{-2}) and strong continuum emission ($I > 15$ mJy/arcsec^2). For detailed analysis, the filament is divided into three subregions: North, BN–KL, and South.

The column density map in Figure 5.5(b) shows that the largest $N(\mathrm{H_2})$ values are concentrated along the filament spine, where the material is organized into three main clumps: North, BN–KL, and South. Among them, BN–KL is the warmest, with dust temperatures reaching about 100 K (Figure 5.5(c)). The eastern side of OMC-1, including the H II region, is generally warmer than the western side, likely because of photoionization heating from the Trapezium cluster. In contrast, the H II region has the lowest gas column density among the subregions.

Figure 5.5(a) shows that the lengths of the polarization vectors reflect the polarization fraction, with relatively high values in the H II region and lower values in some parts of the filament. The colored contours in Figures 5.5(b) and 5.5(c) mark three polarization-hole regions, where the polarization degree falls below 1%, near the centers of the North, BN–KL, and South subregions. Although all three regions are associated with high column density,

the polarization holes in the North and South occur at lower dust temperatures than the one in BN–KL. This suggests that different depolarization mechanisms may be at work in cold and warm environments.

To explore the dependence of polarization percentage P on gas column density ($N(H_2)$), dust temperature (T_d), and magnetic field tangling ($\mathcal{S}$), I present the corresponding correlations in Figure 5.6. The P–$N(H_2)$ relation, see Figure 5.6 a, shows a clear anti-correlation, indicative of the polarization hole effect. Fitting a power-law model to each subregion yields the following indices: $\alpha = -0.33 \pm 0.03$ for the North, $\alpha = -0.50 \pm 0.01$ for BN–KL, $\alpha = -0.45 \pm 0.03$ for the South, and a significantly flatter slope of $\alpha = -0.08 \pm 0.01$ in the H II region. Within the OMC-1 filament, the P–T_d relation reveals more complex behavior. At low dust temperatures, the polarization fraction increases with increasing T_d, but it drops sharply at higher temperatures ($T_d > 70$ K). Specifically, in the South region, P increases steeply with T_d, following a power-law index of $\alpha = 2.82 \pm 0.11$. In the cooler North region ($T_d < 40$ K), a weaker positive trend is observed, with $\alpha = 0.09 \pm 0.08$. In contrast, BN–KL—dominated by massive protostars and high dust temperatures—exhibits a monotonic decrease in P with increasing T_d, with a power index of $\alpha = -0.57 \pm 0.06$. This non-monotonic behavior was also reported [150] using combined JCMT/POL-2 and SOFIA/HAWC+ data. Interestingly, although dust temperatures in the H II region can reach up to 80 K, the polarization fraction continues to increase with temperature, showing a moderate positive slope of $\alpha = 0.41 \pm 0.05$.

I also fit a power-law model to the P–$\mathcal{S}$ relation and find a clear anti-correlation between polarization fraction and angle dispersion function. The fitted slopes are $\alpha = -0.61 \pm 0.02$ for the North, -0.48 ± 0.02 for BN–KL, -0.69 ± 0.02 for the South, and -0.17 ± 0.01 for the H II region. The H II region seems to have relatively weak magnetic field fluctuations, as indicated by low values of $\mathcal{S} < 10°$. In contrast, the South region shows stronger magnetic field fluctuations, with $\mathcal{S} > 10°$.

Figure 5.7 (a) presents the $N(H_2)$–T_d relation. An anti-correlation is observed in the North, South, and H II regions, indicating that higher densities are associated with lower temperatures. However, in the BN–KL region with the presence of massive protostars, the two quantities are positively correlated due to local heating. To further investigate the role of magnetic field tangling in depolarization, I examine the relationships between $\mathcal{S}$ and $N(H_2)$ (Figure 5.7 (b)) and between $\mathcal{S}$ and T_d (Figure 5.7 (c)). The $\mathcal{S}$–$N(H_2)$ relation shows a general positive correlation, suggesting that magnetic field tangling increases with gas density, particularly in the denser filament regions. The $\mathcal{S}$–T_d relation displays contrasting trends across regions: $\mathcal{S}$ is anti-correlated with T_d in the South and H II regions.

Figure 5.7 (d) shows the relationship between $P \times \mathcal{S}$ and T_d, which serves as a proxy for average grain alignment efficiency. The trend suggests a weak increase in alignment efficiency for $T_d < 35$ K, a plateau in the range 35–70 K, and a decline at $T_d > 70$ K. This behavior reflects the interplay between thermal conditions and grain alignment efficiency across different environments in OMC-1.

5.4.2. Modeled Results

Given the complex structure and significantly varying physical conditions in OMC-1, such as differences between the eastern and western parts (e.g., presence or absence of an H II region) and the localized influence of embedded protostars within the filament, I perform pixel-by-pixel modeling across the entire region. This approach enables the generation of polarization fraction maps, which can be directly compared with the observational data.

In modeling the OMC-1 molecular cloud, I use a mean radiation wavelength given by

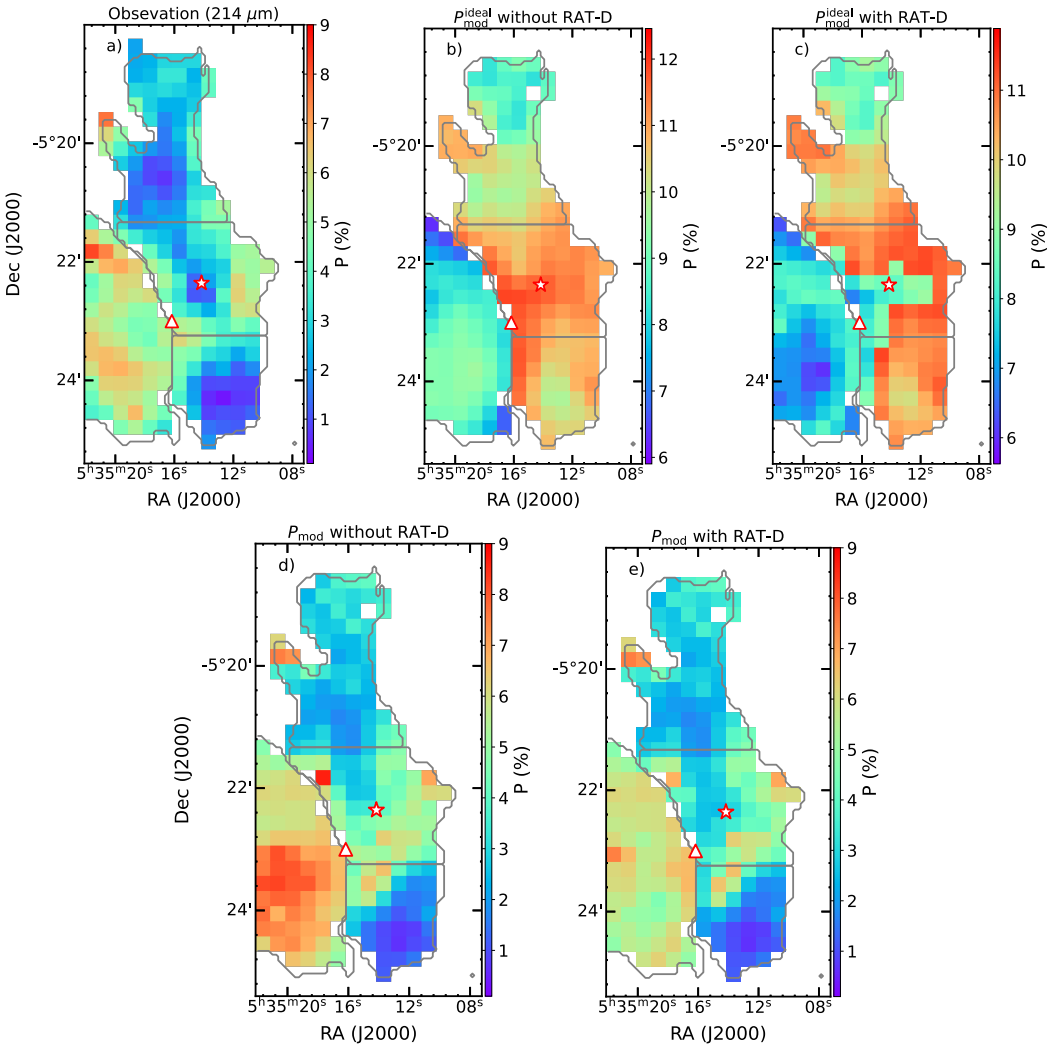

Figure 5.8: OMC-1. Maps of polarization percentage. (a) Observational polarization percentage map. (b–e) Modeled polarization percentage maps under different models: (b) $P_{\rm mod}^{\rm ideal}$ without RAT-D, (c) $P_{\rm mod}^{\rm ideal}$ with RAT-D, (d) $P_{\rm mod}$ without RAT-D, and (e) $P_{\rm mod}$ with RAT-D. Here, "ideal" refers to the case without considering magnetic field inclination and fluctuations. Gray contours outline the four subregions defined in Figure 5.5. The star marks the position of BN/KL, and the triangle indicates the Trapezium cluster.

$\bar{\lambda} \simeq 0.53\ \mathrm{cm, K}/T_\star$ [96]. With a nearby massive OB star cluster characterized by $T_\star > 2\times10^4$ K, this relation gives a typical value of $\bar{\lambda} = 0.3\ \mu$m. The grain alignment and resulting polarization degree are then computed using pixel-by-pixel maps of gas number density ($n_{\rm H_2}$) and dust temperature ($T_{\rm d}$) as model inputs. To derive the gas volume density, I assume a uniform line-of-sight depth for OMC-1 of $d_{\rm OMC} = 0.15$ pc, following the estimate from [148]. The number density is then calculated using $n_{\rm H_2} = N({\rm H_2})/d_{\rm OMC}$. To reduce measurement noise and optimize model computation time, I increase the effective pixel size by a factor of 4 to be 14″, which is almost equal to the spatial resolution of the input data maps.

Since grain growth is likely to be efficient in dense star-forming regions, I assume a maximum grain size of $a_{\rm max} = 2\ \mu$m in parts of OMC-1 where the column density exceeds $N({\rm H_2}) > 2\times10^{22}\ {\rm cm^{-2}}$. For less dense regions, including the outer filament and the nearby

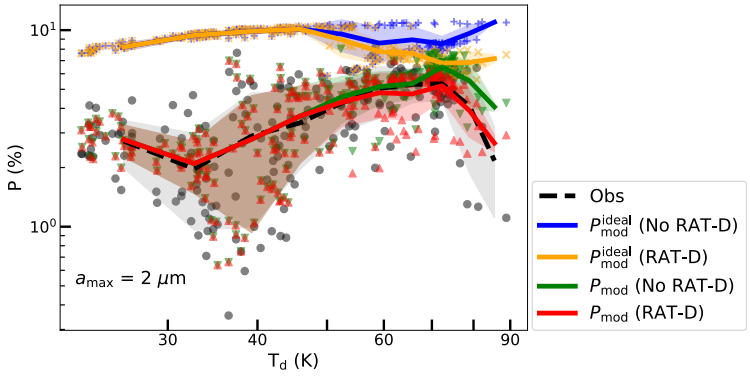

Figure 5.9: OMC-1. Comparison between modeled (color lines) and observed (black dashed line) polarization degree as a function of dust temperature. The shaded area represents the 1-σ deviation of each bin of data points which are shown by points (black for observation data and color for model data). The ideal polarization models (blue and orange lines), which neglect magnetic field inclination and fluctuations, tend to overestimate the polarization degree. In contrast, the realistic model (red line), which incorporates RAT-A, RAT-D, and magnetic field tangling ($P_{\rm mod}$), provides the best agreement with the observed P–$T_{\rm d}$ relation.

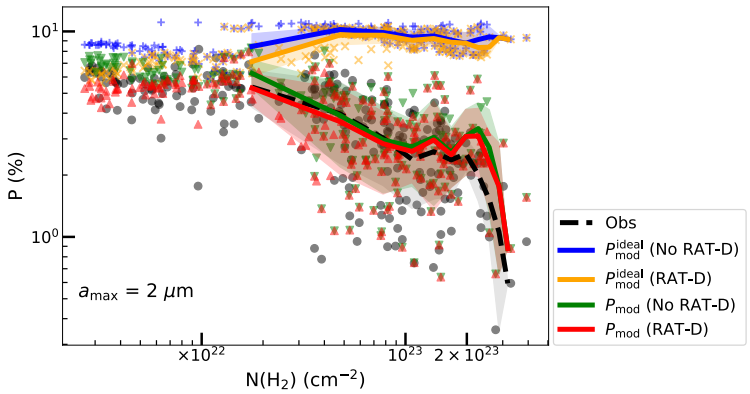

Figure 5.10: OMC-1. Same as Figure 5.9 but for $P - N(\mathrm{H_2})$ relation. The observational trend cannot be explained by the ideal polarization models (blue and orange lines). In contrast, the realistic model (red line), which accounts for RAT-A, RAT-D, and magnetic field tangling ($P_{\rm mod}$), reproduces the observed polarization hole most successfully.

H II region, I instead adopt $a_{\rm max} = 0.2\,\mu$m, consistent with values commonly used for the diffuse ISM. To account for RAT-D, which should be important in OMC-1 under its intense radiation environment, the tensile strength of dust grains also needs to be included. Because the tensile strength is linked to the internal grain structure, for example porosity, and this structure is expected to depend on grain size through coagulation [219], I use $S_{\rm max} = 10^7$ erg cm^{-3} for larger grains ($a_{\rm max} = 2\,\mu$m) and $S_{\rm max} = 10^8$ erg cm^{-3} for smaller grains ($a_{\rm max} = 0.2\,\mu$m).

As shown in Figure 5.6 (c), the polarization angle dispersion function $\mathcal{S}$ in OMC-1 can reach values as high as 50°. The slopes of the P–$\mathcal{S}$ relation, ranging from 0.47 to 0.69 within the filament, indicate that magnetic field tangling in OMC-1 is both stronger and more spatially variable than in Musca. Therefore, the ideal polarization outputs from `DustPOL-py` are insufficient to describe the observed depolarization behavior. Instead, I apply a polarization model that incorporates the effects of magnetic field fluctuations, as given by Equation 5.7, with varying η values for different subregions of OMC-1.

Table 5.2: Comparison between models and observations across different regions in OMC-1: North, BN-KL, South, H II, and all. The statistical evaluation is shown by $\chi^2 = \frac{1}{N}\sum_{i=1}^{N}\frac{(P^{i}_{\rm mod}-P^{i}_{\rm obs})^2}{P^{i}_{\rm obs}}$ with N the number of pixels within each region. As shown, the values of χ^2 are the highest for $P^{\rm ideal}_{\rm mod}$. $P_{\rm mod}$ with magnetic field tangling and RAT-D produces the smallest χ^2, which implies that both grain disruption and magnetic field tangling play an important role in the observed polarization. In addition, the model with the rotational disruption effect matches observations in BN-KL and HII regions much better.

Model	χ^2				
	North	BN-KL	South	H II	All
$P^{\rm ideal}_{\rm mod}$ without RAT-D	21.65	17.34	46.77	1.39	18.76
$P^{\rm ideal}_{\rm mod}$ with RAT-D	21.65	12.24	45.88	0.65	17.20
$P_{\rm mod}$ without RAT-D	0.32	0.83	0.30	0.32	0.43
$P_{\rm mod}$ with RAT-D	0.32	0.55	0.4	0.17	0.34

Figure 5.8 (b–e) displays the modeled polarization percentage maps obtained from our numerical models, while Figure 5.8 (a) presents the observational data for comparison. All maps are resampled to a pixel size of approximately 14″ to match the pixel size used in the modeling. In Figure 5.8 (b), the ideal polarization model without RAT-D ($P^{\rm ideal}_{\rm mod}$) reproduces portions of the polarization holes in the North and South regions but fails to capture the significant depolarization observed in BN–KL. When RAT-D is included (Figure 5.8 (c)), the modeled polarization decreases in the BN–KL region, although the predicted values are still significantly higher than the observed data. Figures 5.8 (d) and 5.8 (e) present models that incorporate magnetic field tangling effects, $P_{\rm mod}$ without and with RAT-D, respectively. The depolarization parameter η is assigned separately for each subregion, $\eta = 0.61$, 0.48, 0.69, and 0.17 for the North, BN–KL, South, and H II regions, based on the slopes of the P–$\mathcal{S}$ relation shown in Figure 5.6 (c). The model excluding RAT-D (Figure 5.8 (d)) improves agreement in the North and South but still does not reproduce the depolarization seen in BN–KL and the H II region. In contrast, the model that includes both magnetic field tangling and RAT-D (Figure 5.8 (e)) successfully reproduces the observed polarization pattern across all regions, including BN–KL and the H II regions.

To quantitatively assess model performance, I further examine two diagnostic relations: P–$T_{\rm d}$, which reflects the influence of grain alignment and disruption; and P–$N(\rm H_2)$, which probes the effect of gas damping on polarization degree. Figures 5.11 and 5.12 present detailed comparisons between our polarization models and the observed P–$T_{\rm d}$ and P–$N_{\rm H_2}$ relations, across different subregions of OMC-1: the North, South, and BN–KL regions. Among the models, the realistic polarization model that includes both RAT-D and magnetic field tangling provides the best agreement with the observational data, successfully reproducing the observed trends in both dust temperature and column density dependencies.

Figure 5.9 presents a comparison between the modeled and observed P–$T_{\rm d}$ relations for the whole OMC-1. There is a noticeable correlation between P and $T_{\rm d}$ at low temperatures, < 70 K, while an anti-correlation is observed at high temperatures, > 70 K. Models that do not account for magnetic field fluctuations fail to reproduce this dual behavior. In contrast, models that incorporate both RAT-D and magnetic field tangling provide the best agreement with the observed trends.

The Figure 5.11 shows corresponding P–$T_{\rm d}$ comparisons for individual subregions: North, South, BN–KL, and the H II region. In the cooler North and South regions, where dust temperatures remain below the RAT-D threshold, the results of models with only RAT-A and those including RAT-D are nearly identical, indicating that grain disruption does not occur. However, in the BN–KL and H II regions, which are subject to elevated radiation fields and higher temperatures ($T_{\rm d} > 50$ K), only models incorporating both RAT-D and magnetic field fluctuations successfully reproduce the observed decline in polarization degree.

Figure 5.10 compares the modeled and observed P–$N(\mathrm{H_2})$ relations. The idealized models ($P_{\rm mod}^{\rm ideal}$), which do not include magnetic field fluctuations, systematically overestimate the polarization degree and fail to reproduce the observed polarization holes. In contrast, the more realistic models ($P_{\rm mod}$), which incorporate magnetic field tangling, show significantly better agreement with the data. These results suggest that the primary driver of depolarization in the P–$N(\mathrm{H_2})$ relation is magnetic field tangling. Grain alignment remains efficient even at high column densities, likely due to the influence of embedded radiation sources. This behavior contrasts with that observed in Musca, where the polarization hole arises primarily from reduced grain alignment efficiency in dense regions with weak external radiation.

A quantitative comparison of the model performance, based on χ^2, is given in Table 5.2. The χ^2 values are higher for $P_{\rm mod}^{\rm ideal}$ and lower when RAT-D is included in $P_{\rm mod}^{\rm ideal}$. The improvement is especially clear in the BN-KL and H II regions, where the RAT-D effect is expected to occur. The model $P_{\rm mod}$ that includes magnetic field tangling gives even smaller χ^2 values, suggesting that both grain alignment and magnetic field tangling contribute to the observed polarization degree. Therefore, the best-fitting model is $P_{\rm mod}$ with both RAT-D and magnetic field tangling included.

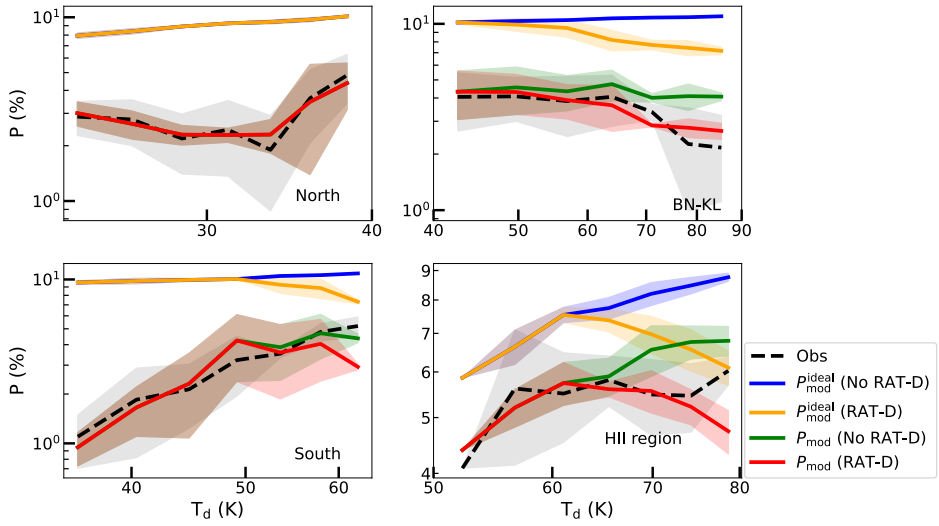

Figure 5.11: OMC-1. Comparison between the polarization percentage and dust temperature from the models and observations. The colored lines show the model results, while the dashed line represents the observational data. The shaded region indicates the 1-σ dispersion within each temperature bin.

5.5. Discussions

In this section, I examine the evidence for grain alignment and rotational disruption predicted by the RAT paradigm, through a comparison between our modeling results and the observa-

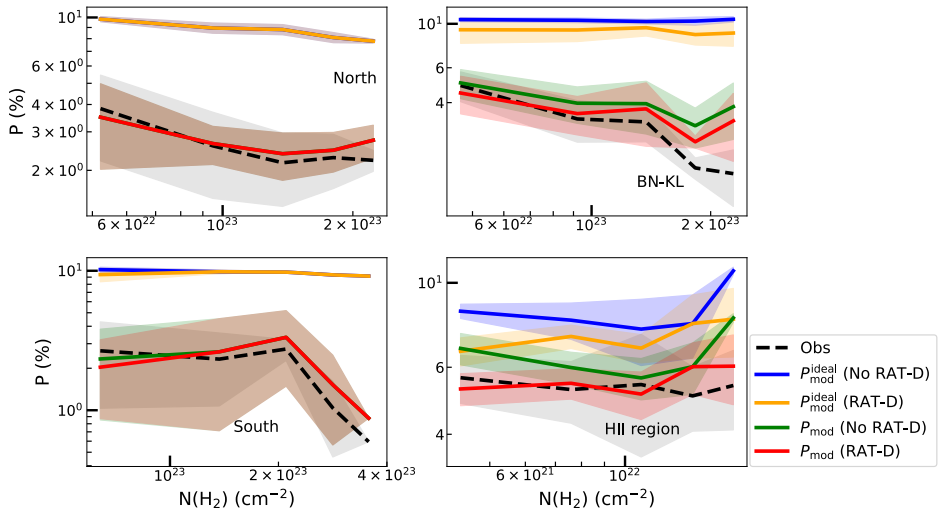

Figure 5.12: OMC-1. Comparison of polarization percentage versus column density between models and observations. The colored lines show the model results, while the dashed line represents the observational data. The shaded region indicates the 1-σ dispersion within each bin.

tional data for Musca and OMC-1.

5.5.1. Evidence of RAT-A Mechanism

A widely supported explanation is the reduction in grain alignment efficiency in denser regions, as predicted by the RAT mechanism [96]. Within the framework of RAT-A theory, only dust grains larger than a certain threshold—referred to as the minimum alignment size—can be effectively aligned with magnetic fields. This threshold, $a_{\rm align}$, scales with local physical conditions as $a_{\rm align} \propto n_{\rm H}^{2/7} T_{\rm d}^{-12/7}$ (see Equation 5.1). Therefore, higher densities and lower dust temperatures lead to a rise in $a_{\rm align}$, narrowing the population of grains that can align and thus reducing the overall polarization percentage [100]. $a_{\rm align} \propto n_{\rm H}^{2/7} T_{\rm d}^{-12/7}$ (see Equation 5.1).

To test this prediction quantitatively, I carried out polarization modeling toward Musca—a well-studied, relatively simple filamentary cloud that exhibits a distinct polarization hole. Using observationally constrained maps of gas density and dust temperature as inputs for the `DustPOL-py` code, I modeled the expected polarization signal across the filament. The results show that $a_{\rm align}$ increases significantly from the outer regions toward the spine, as density rises and radiation weakens (see Figure 5.4, upper panel). This leads to a clear drop in the modeled polarization fraction (P) toward the filament's center, successfully reproducing the observed polarization hole (Figure 5.4, lower panel).

A key prediction of the RAT-A mechanism is that the polarization degree should increase with dust temperature. This is because the minimum alignment size, $a_{\rm align}$, decreases with increasing $T_{\rm d}$ (see Equation 5.1), allowing a broader range of grain sizes to be aligned with the magnetic field [100].

For both Musca and OMC-1, the observational data confirm this trend at lower dust temperatures: the polarization degree (P) increases with $T_{\rm d}$. However, in the case of OMC-1—where strong radiation fields are present—the P–$T_{\rm d}$ relation exhibits a turnover at sufficiently high temperatures, with P decreasing as $T_{\rm d}$ increases. This reversal is indicative of rotational disruption, consistent with the predictions of the RAT-D mechanism. Our detailed

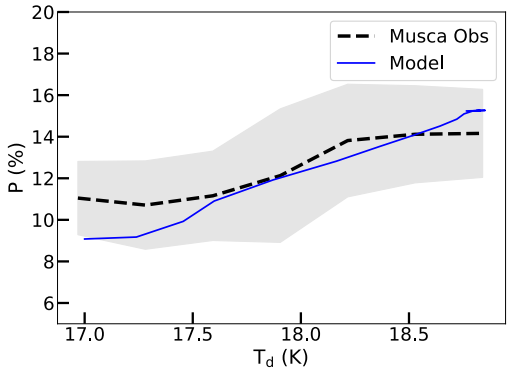

Figure 5.13: Musca: Comparison between the modeled and observed relation of polarization degree versus dust temperature. The blue line represents the results from our RAT-A–based polarization model, while the black line shows the observational data. The shaded regions indicate the 1σ dispersion within each temperature bin. The observed increase in polarization degree with dust temperature is reproduced by the model, supporting the prediction of the RAT-A alignment mechanism.

modeling for both Musca and OMC-1 successfully reproduces the observed rising trend of P with $T_{\rm d}$ at low temperatures (see Figures 5.13 and 5.14), supporting the theoretical framework of radiative torque alignment.

In addition to grain alignment efficiency and dust properties, the polarization fraction (P) is also affected by fluctuations in the magnetic field both along the line of sight and within the telescope beam [201]. Because the observed polarization angle in the plane of the sky represents an average over the polarization vectors aligned with local magnetic fields along the LOS, variations in field orientation can reduce the net polarization. The polarization angle dispersion function, $\mathcal{S}$, is commonly used as a proxy to characterize these magnetic field fluctuations.

In Musca, magnetic field fluctuations are relatively small across the filament (see Figure 5.3). In this case, our polarization model based on the RAT paradigm, without invoking additional depolarization effects, successfully reproduces the observed data (Figure 5.4). This indicates that the primary cause of the polarization hole in Musca is the loss of grain alignment in denser, colder regions, and that the impact of magnetic field tangling is minimal.

In contrast, OMC-1 exhibits strong and spatially variable magnetic field fluctuations (Figure 5.7). Modeling results demonstrate that the idealized model without field tangling ($P_{\rm mod}^{\rm ideal}$) systematically overestimates the polarization degree and fails to reproduce the observed trends. Only the more realistic models that incorporate the effects of magnetic field tangling ($P_{\rm mod}$) are able to match the observations (Figure 5.9). These findings highlight the role of magnetic field tangling in generating the polarization hole in OMC-1, particularly in regions with high column densities and strong radiation fields.

5.5.2. Evidence of RAT-D Mechanism in OMC-1

A distinct correlation between polarization fraction (P) and dust temperature ($T_{\rm d}$) is observed in the OMC-1 filament: P increases with $T_{\rm d}$ at low temperatures but decreases at higher $T_{\rm d}$. While the rising trend at low temperatures is consistent with predictions from the RAT-A mechanism, the declining trend at high temperatures deviates from it and instead points to the signature of grain disruption via RAT-D.

To investigate whether RAT-D can account for this behavior, I carried out detailed pixel-by-pixel modeling of thermal dust polarization using observationally derived maps of gas volume density and dust temperature. The modeling results successfully reproduce the observed P–$T_{\rm d}$ relation in OMC-1, as shown in Figure 5.9.

It is important to emphasize that magnetic field tangling alone, incorporated in the $P_{\rm mod}$ models, cannot explain the observed decline of P at high $T_{\rm d}$. As demonstrated in Figure 5.7, the polarization angle dispersion function ($\mathcal{S}$) remains low or nearly constant at high $T_{\rm d}$, indicating that field fluctuations are not the main cause of depolarization in this regime. Only when both magnetic field tangling and the RAT-D effect are included in the models (see Section 5.2) does the decreasing trend of P with $T_{\rm d}$, aligning with the observational data. Hence, This provides strong evidence that the RAT-D effect can explain the decreasing trend $P - T_{\rm d}$ in OMC-1 at high dust temperatures.

Additional evidence of RAT-D has been found in various star-forming environments, including Auriga and M17 (shown in Chapter 4), ρ Ophiuchi A [101], 30 Doradus [202], ang Orion Bar [151] further supporting the RAT-D mechanism.

5.5.3. Implication for Probing Grain Growth

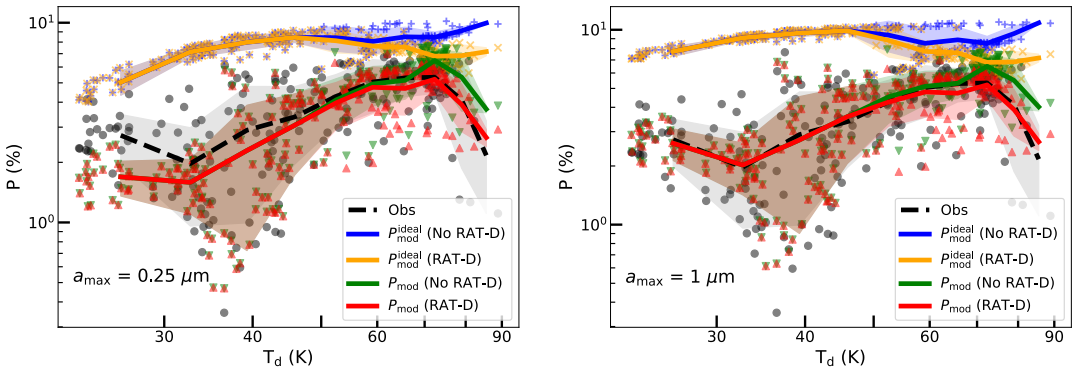

Figure 5.14: Comparison between the modeled and observed polarization fractions for different assumed initial maximum grain sizes: $a_{\rm max} = 0.25\,\mu$m (left panel) and $a_{\rm max} = 1\,\mu$m (right panel). The realistic models with larger grains (red line) provide a better fit to the data in regions of high density and low dust temperature ($T_{\rm d} < 50$ K), indicating significant grain growth in these dense environments.

Observational studies suggest that the upper limit of the interstellar grain size distribution in the diffuse ISM is approximately $0.25\,\mu$m [60]. However, within dense molecular clouds or filamentary structures, grain growth is expected due to processes such as gas accretion and grain coagulation. Evidence for grain growth in dense environments has been reported [132], who used starlight polarization observations combined with RAT-based modeling. Similarly, I found moderate grain growth in the G11 filament (see Chapter 4), with $a_{\rm max} > 0.3\,\mu$m when the gas volume density exceeds $10^4\,{\rm cm}^{-3}$.

In this study, our numerical modeling for Musca (Figure 5.13) indicates that the maximum grain size is approximately 0.3–0.35 μm. This suggests that while grain growth is occurring, it remains moderate, consistent with the relatively low volume density of Musca ($n_{\rm H} \sim 10^3\,{\rm cm}^{-3}$).

In contrast, OMC-1 exhibits significantly higher and spatially varying densities, reaching up to 10^4–$10^6\,{\rm cm}^{-3}$. To explore grain growth in this dense region, I varied $a_{\rm max}$ from 0.2

to $2\,\mu$m in the polarization modeling. The results show that models with $a_{\rm max} > 1\,\mu$m best reproduce the observed P–$T_{\rm d}$ relation, particularly in regions with low dust temperatures ($T_{\rm d} < 50$ K; see Figure 5.14, left panel). This provides strong evidence that grain growth is significant in the dense parts of OMC-1.

5.5.4. Limitations of Our Modeling and Future Works

In this study, I employed a hybrid approach to investigate thermal dust polarization and assess the predictions of the RAT paradigm. I first used the `DustPOL-py` code to compute the polarization degree under the idealized assumption that magnetic fields lie entirely in the POS. To incorporate more realistic conditions, I introduced a correction factor Φ to account for the inclination angle between the magnetic field and the line of sight, and a depolarization term $\mathcal{S}^{-\eta}$ to describe the effect of magnetic field fluctuations (see Equation 5.7). The resulting polarization model is based on the optically thin approximation, which has been validated through synthetic observations of MHD simulations using `POLARIS` [201].

While our model successfully reproduces the observed polarization patterns and provides support for the RAT paradigm, several limitations remain. First, I assumed perfect alignment of dust grains ($f_{\rm max} = 1$) through the MRAT mechanism, which is expected for grains containing embedded iron inclusions. Second, the inclination factor Φ, derived from fitting the model to the maximum observed polarization, is assumed to be constant across the filament. This assumption is likely appropriate for Musca, which has well-ordered magnetic fields and a small depolarization slope ($\eta \sim 0.03$). However, it may be an oversimplification for a complex and turbulent region like OMC-1, where magnetic field fluctuations are stronger and the η values vary significantly across sub-regions.

In future work, I plan to conduct fully synthetic dust polarization modeling using MHD simulations with the upgraded `POLARIS` code [91], which incorporates both the RAT mechanism and radiative transfer. A detailed comparison between these simulations and observational data will allow us to better disentangle the various contributors to the polarization hole—whether from loss of grain alignment, grain disruption, or magnetic field tangling.

5.6. Conclusions

In this study, dust polarization observations toward Musca and OMC-1 were analyzed to investigate grain alignment and rotational disruption mechanisms driven by radiative torques (i.e., the RAT paradigm). By examining the relationships between the polarization fraction (P) and key physical parameters, namely gas column density ($N(\mathrm{H_2})$), dust temperature ($T_{\rm d}$), and the polarization angle dispersion function ($\mathcal{S}$), and comparing them with theoretical predictions from the RAT paradigm, I aim to constrain the physical processes responsible for dust grain alignment. The main conclusions are summarized as follows:

1. Observational data reveal the presence of polarization holes, characterized by a decrease in polarization fraction with increasing column density, in both Musca and OMC-1. Analysis of the polarization angle dispersion function indicates weak magnetic field fluctuations in Musca, but strong and spatially varying fluctuations in OMC-1.

2. In Musca, where magnetic field tangling is small, detailed modeling using the RAT alignment theory reproduces the observed polarization hole. This supports the interpretation that the decrease in P arises from the loss of grain alignment in denser and colder regions. The modeling also suggests that while grain growth is present, it is not substantial in this quiescent filament.

3. In OMC-1, a high-mass star-forming region, an anti-correlation between P and $\mathcal{S}$ is found, while $\mathcal{S}$ increases with $N(\mathrm{H_2})$, especially at low temperatures. This behavior indicates that magnetic field fluctuations play a dominant role in depolarization in dense regions.

4. The observed relationship between P and T_d exhibits a dual behavior: at low temperatures (e.g., in the North and South), P increases with T_d; however, in the high-temperature BN/KL region, P decreases with T_d.

5. Through pixel-by-pixel modeling using the `DustPOL-py` code and local physical parameters derived from observations (gas density and dust temperature), I show that the observed P–T_d and P–$N(\mathrm{H_2})$ trends can be successfully reproduced when both RAT-A and RAT-D mechanisms, as well as magnetic field fluctuations, are taken into account. The decreasing P–T_d trend in BN–KL is particularly well matched by models including RAT-D.

6. The successful application of pixel-by-pixel polarization modeling in both a quiescent filament, Musca, and an active star-forming region, OMC-1, provides strong empirical support for the RAT paradigm. This approach offers a promising framework for constraining grain alignment physics and dust properties in other astrophysical environments.

Chapter 6

Summary and Future Work

6.1. Summary

This thesis presents an investigation into the role of magnetic fields and dust grain physics in star formation, using thermal dust polarization observations and numerical modeling. The study encompasses various star-forming environments, ranging from quiescent to active regions and differing in density, radiation field intensity, and evolutionary stage. Two overarching scientific goals guide the work:

(1) Understanding the role of magnetic fields in star formation

(2) Probing the physics of grain alignment and disruption mechanisms

The following targets were analyzed in detail to address these goals:

LkHα 101: A nearby and low star formation rate region in the Auriga-California molecular cloud at a distance of ~450 pc, observed at 850 μm by JCMT.

M17: A photodissociation region located ~2 kpc away, observed at 157 μm by SOFIA/HAWC+.

G11.11 -0.12: A massive filamentary molecular cloud at ~3.6 kpc, with a low star formation rate, observed by SOFIA/HAWC+ at 214 μm.

Musca: A low star formation rate filament at 150 pc, one of the simplest filaments without embedded protostars, observed by *Planck* at 850 μm.

OMC-1: The closest high-mass star-forming region at 366 pc, observed by SOFIA/HAWC+ at 214 μm.

The main results are summarized in Section 6.1.1 for magnetic fields and Section 6.1.2 for dust physics.

6.1.1. Magnetic Fields

The Davis-Chandrasekhar-Fermi (DCF) method is applied to quantify the magnetic field strength in different environments, using inputs such as column density, polarization angle, and velocity dispersion.

- **LkHα 101 (Auriga–California Cloud)**: For the first time, the morphology and strength of the magnetic field in LkHα 101 are reported. The magnetic fields are generally parallel to the matter structure of the dust lane and become quite complex in the central region with the presence of a B star. The measured strength is ~115 μG. The low mass-to-flux ratio and sub-Alfvénic turbulence support a scenario where magnetic fields dominate over gravity and turbulence, implying that magnetic support plays a significant role in suppressing collapse.

- **M17**: The magnetic field strength, estimated using the DCF method, is 980 μG in the northern part (M17-N) and 1665 μG in the southern part (M17-S). The magnetic field morphology represents an asymmetric large-scale hourglass structure that may reflect a collapsing core. The field is strong enough to dominate over turbulence ($\mathcal{M}_A < 1$) and resist gravitational collapse ($\lambda < 1$), implying that the magnetic fields in the regions are strong enough to resist gravitational collapse. These results are consistent with the deficiency in forming massive stars in the region found by previous studies.

- **G11.11–0.12 (The Snake Filament)**: The full magnetic-field map of the G11.11-0.12 filament is presented for the first time. The magnetic fields are predominantly perpendicular to the filament's spine. Field strengths range from 100 to 600 μG, with the highest strengths located near the filament's high-density spine and lower strengths in the outer regions. The region is found to be sub-critical (mass-to-flux ratio $\lambda < 1$). From the maps of the mass-to-flux ratio and Alfvénic Mach number, G11 exhibits strong magnetic fields, which dominate gravity and turbulence.

6.1.2. Dust Physics

The comprehensive analysis techniques for analyzing polarization vectors (including polarization degree and polarization angle) were developed to constrain dust physics, resulting in a significant understanding of dust grain alignment in the studied regions. This work provided the most comprehensive observational evidence so far supporting the RAT paradigm, including both the grain alignment and disruption mechanisms. The analysis techniques have been applied to study magnetic fields and dust physics in other regions by our collaborators in the framework of the BALLAD-POL project.

The key findings on dust physics from this thesis include:

- **RAT Alignment (RAT-A)**: Observed polarization holes in G11 and Musca can be explained by reduced grain alignment efficiency in high-density and low-radiation environments–consistent with the predictions of RAT-A theory.

- **RAT Disruption (RAT-D)**: In hot regions (e.g., M17, OMC-1, and LkHα 101), the polarization fraction decreases with increasing dust temperature, contrary to pure RAT-A predictions. This trend aligns with the predictions of RAT-D, where large grains are destroyed by intense radiation, thereby reducing the range of grain sizes in which grains can be aligned by RATs.

- **Grain Growth**: Evidence for dust-grain growth in dense filaments such as G11.11-0.12 and OMC-1 is reported. Using polarization fraction slopes and alignment size analysis in G11, maximum grain sizes must exceed 0.3 μm in the filament's spine. Using our numerical model, the maximum grain size is identified as being larger than 1 μm in OMC-1 to match the observations.

- **Magnetic Relaxation**: High polarization fractions in the outer layers of G11 (>20%) can be explained by magnetically enhanced RAT (MRAT) alignment. The calculations show that magnetic relaxation is important when the efficiency parameter $\delta_{\rm mag} > 10$, which takes place when grains having iron included in the form of clusters become superparamagnetic.

- **Numerical Modeling**: Using the `DustPOL-py` code [100, 101], the pixel-by-pixel modeling of polarization using the RAT paradigm has been first applied to Musca and OMC-1. This enables constraining dust physics and properties in star-forming regions: the quiescent Musca filament and the active star-forming region OMC-1. Strong evidence in support of the RAT paradigm in Musca and OMC-1 is found. This confirms the applicability of the RAT paradigm and provides constraints on dust properties in diverse astrophysical conditions.

6.2. Future Work

This study demonstrates that our techniques can be applied to investigate both magnetic fields and dust physics in star-forming regions. Several future directions are:

(1) Broader Sample of Star-Forming Regions

While this thesis studied five diverse regions, the current sample remains statistically limited. I will expand the application of the polarization analysis and modeling methods to additional environments with diverse physical conditions.

Our proposed techniques to analyze the polarization fraction to constrain dust physics and magnetic fields in this thesis are published and being conducted as the "B-fields and Dust in Interstellar Filaments Using Dust Polarization (BALLAD-POL)" project. The techniques have been applied by our international collaborators to other star-forming regions, including G34.43 [220], Serpens Main [221], and the Cocoon Nebula (IC 5146) [222] as part of the BALLAD-POL series.

Moreover, the current study is limited to the molecular cloud scale with observations from single-disk telescopes (JCMT and SOFIA); the addition of polarimeters to interferometers (like ALMA and NOEMA) can enable protostar or core-scale studies.

(2) Multi-Wavelength Polarization Observations

Single-wavelength polarization observations offer limited constraints on grain size and alignment properties. The next step is to combine polarimetry across a broad range of wavelengths, from far-infrared to submillimeter and millimeter regimes. Combining JCMT, SOFIA, ALMA, and NOEMA data will provide a more comprehensive understanding of how polarization depends on grain characteristics and environmental parameters. Different wavelengths probe different physical conditions: shorter wavelengths trace warmer regions, while longer wavelengths are more sensitive to cooler and denser regions.

Furthermore, the polarization spectrum can reveal information about dust composition and internal structure, for example, distinguishing between carbonaceous and silicate materials or composite and separate dust grain models. Our numerical tool, `DustPOL-py` [100, 101], can generate multi-wavelength polarization predictions that can be directly compared with observational data.

(3) 3D Magnetic Fields

Reconstructing the three-dimensional (3D) structure of magnetic fields is challenging. While this thesis has focused on analyzing the plane-of-sky magnetic field structures, recent advancements offer methodologies to infer the 3D magnetic field configurations. A new method was presented in [201] that combines thermal dust polarization observations with the radiative torque alignment theory to reveal the inclination angle of magnetic fields. They tested the method using synthetic observations from magnetohydrodynamic simulations of filamentary clouds and suggested using observational data to test the method. With rich polarization observations toward filaments, I plan to study the 3D magnetic fields of filaments.

Single-wavelength polarization observations offer limited constraints on grain size and alignment properties. The next step is to combine polarimetry across a broad range of wavelengths, from far-infrared to submillimeter and millimeter regimes. Combining JCMT, SOFIA, ALMA, and NOEMA data will provide a more comprehensive understanding of how polarization depends on grain characteristics and environmental parameters. Different wavelengths probe different physical conditions: shorter wavelengths trace warmer regions, while longer wavelengths are more sensitive to cooler and denser regions.

Furthermore, the polarization spectrum can reveal information about dust composition and internal structure, for example, distinguishing between carbonaceous and silicate materials or composite and separate dust grain models. Our numerical tool, `DustPOL-py` [100, 101], can generate multi-wavelength polarization predictions that can be directly compared with observational data.

(3) 3D Magnetic Fields

Reconstructing the three-dimensional (3D) structure of magnetic fields is challenging. While this thesis has focused on analyzing the plane-of-sky magnetic field structures, recent advancements offer methodologies to infer the 3D magnetic field configurations. A new method was presented in [201] that combines thermal dust polarization observations with the radiative torque alignment theory to reveal the inclination angle of magnetic fields. They tested the method using synthetic observations from magnetohydrodynamic simulations of filamentary clouds and suggested using observational data to test the method. With rich polarization observations toward filaments, I plan to study the 3D magnetic fields of filaments.